1-13-95

SANDIA REPORT

SAND92-0983 • UC-703
Unlimited Release
Printed December, 1994

Dynamic Properties of Indiana, Fort Knox and Utah Test Range Limestones and Danby Marble Over the Stress Range 1 to 20 GPa

M. D. Furnish

Prepared by
Sandia National Laboratories
Albuquerque New Mexico 87185 and Livermore, California, 94550
for the United States Department of Energy
under Contract DE-AC04-94AL85000

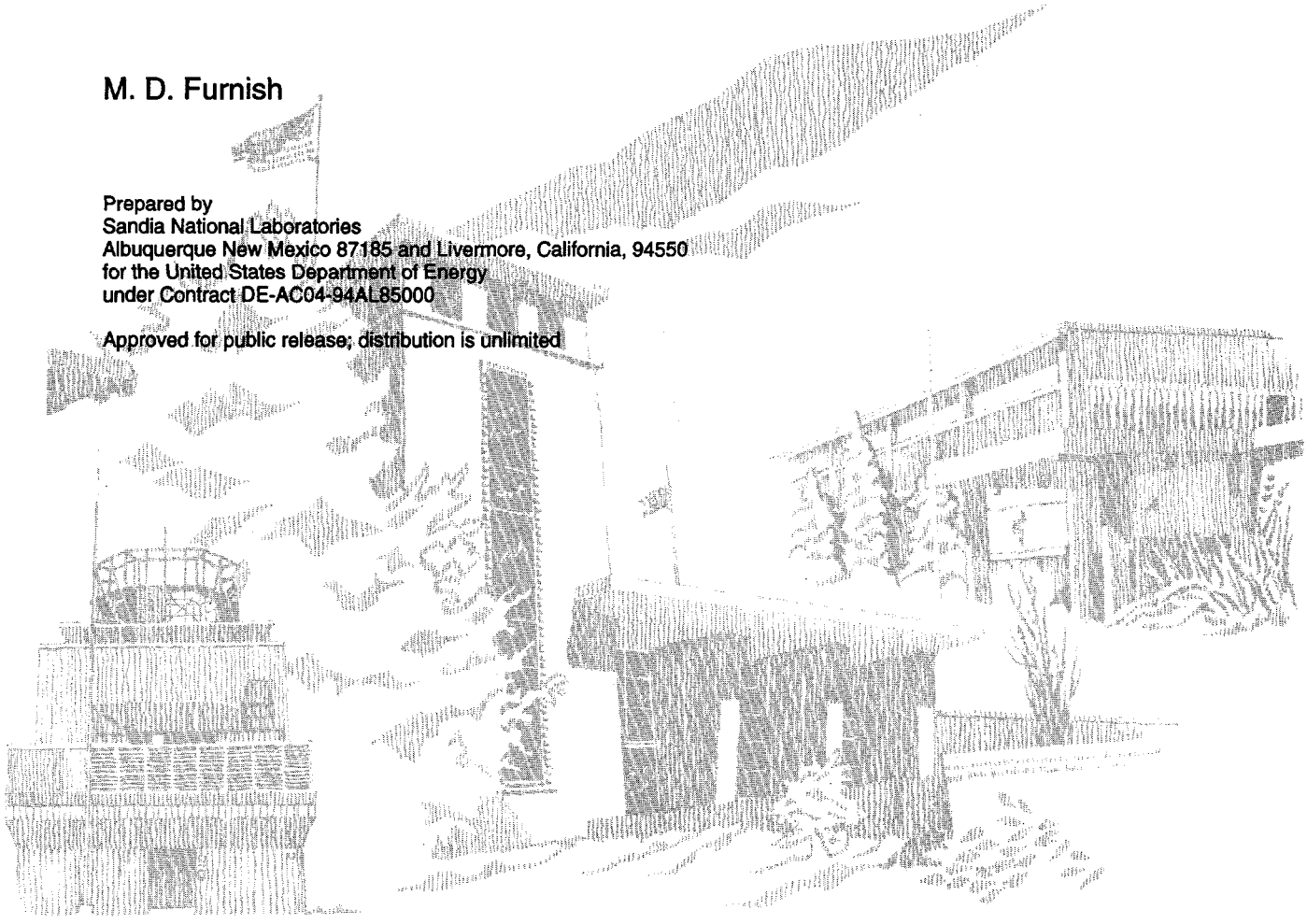

Issued by Sandia National Laboratories, operated for the United States Department of Energy by Sandia Corporation

Available to DOE and DOE contractors from
Office of Scientific and Technical Information
PO Box 62
Oak Ridge, TN 37831

Prices available from (615) 576-8401

Available to the public from
National Technical Information Service
US Department of Commerce
5285 Royal Port Rd
Springfield, VA 22161

NTIS price codes
Printed copy: A06
Microfiche copy: A01

DISCLAIMER

Portions of this document may be illegible in electronic image products. Images are produced from the best available original document.

SAND92-0983
Unlimited Release
Printed December, 1994

Distribution
Category UC-703

Dynamic Properties of Indiana, Fort Knox and Utah Test Range Limestones and Danby Marble Over the Stress Range 1 to 20 GPa

Michael D. Furnish
Experimental Impact Physics Department

Sandia National Laboratories

Albuquerque NM 87185

Abstract

The responses of the following carbonate materials to shock loading and release have been measured: Indiana limestone (18% porosity; saturated and dry), Jeffersonville/Louisville Limestones (Fort Knox limestone) (variable dolomitization, low porosity), Danby Marble (essentially pure calcite; low porosity), and a limestone from the Utah Test and Trainig Range (low porosity, with 22% silica). Various experimental configurations were used, some optimized to yield detailed waveform information, others to yield a clean combination of Hugoniot states and release paths. All made use of velocity interferometry as a primary diagnostic. The stress range of 0 - 20 GPa was probed (in most cases, emphasizing the stress range 0 - 10 GPa). The primary physical processes observed in this stress regime were material strength, porosity, and polymorphic phase transitions between the $CaCO_3$ phases I, II, III and VI. Hydration was also a significant reaction under certain conditions. The Indiana Limestone studies in particular represent a significant addition to the low-pressure database for porous limestone. Temperature dependence and the effect of freezing were assessed for the Fort Knox limestone. Experimental parameters and detailed results are provided for the 42 impact tests in this series.

Acknowledgments

There are many people to whom I am grateful for advice, guidance and patience through the course of this work. I am grateful to Eric Rinehart and Audrey Martinez (Defense Nuclear Agency/Experimental Shock Physics Office) for not only serving well as sponsors and monitors, but also for encouraging me to be a part of the community that needed the results. I hope that the other members of the community feel this participation made the resulting product more useful than "toss-it-over-the-wall" data. I am grateful to Ron McIntosh and Carl Konrad for handling the myriads of details associated with building up the shots and operating the guns and instruments. Jerry Kerley was always happy to give me feedback on how carbonates work, and reviewed this report (as did Dennis Grady, Eric Rinehart and Audrey Martinez). Jerry suggested the CTH modeling of Section 3.3.4, then badgered me to do it better (even doing runs himself) until it became of adequate quality to include in this writeup. My manager, Phil Stanton, has been very encouraging throughout. Finally, my wife Linn has been very supportive even under the weight of a four-year-old Sarah and a very busy toddler Rebecca (codename Girlzilla), who also deserve acknowlegement for extra time I spent working instead of playing.

This work was sponsored largely by the Defense Nuclear Agency and conducted under the auspices of the U. S. Department of Energy under Contracts DE-AC04-76DP00789 and DE-AC04-94AL85000. In addition, a portion of this work (that related to the Indiana Limestone) was sponsored by Los Alamos National Laboratory.

Table of Contents

Figures

Tables

Dynamic properties of Indiana, Fort Knox and Utah Test Range Limestones and Danby Marble Over the Stress Range 1 to 20 GPa

1.0 Introduction

1.1 Motivation

Significant fractions of the crust of the earth are composed of carbonate mineralogies, largely because of the action of living organisms through geologic time. Consequently the response of many parts of the crust to dynamic events is dominated by that of such minerals as calcite ($CaCO_3$), dolomite ($CaMg(CO_3)_2$), aragonite ($CaCO_3$) and magnesite ($MgCO_3$) (roughly in descending order of abundance).

The present study provides Hugoniot, loading, and (more significantly) release information for rocks composed of these mineralogies. Data are presented which are useful for modeling groundshock and related dynamic phenomena in carbonate rockmasses. Although most of the materials studied were composed dominantly of calcite, some information pertinent to dolomite mineralogies is presented as well.

1.2 What has gone before

Calcite and related mineralogies have been subjects of experimental studies and theoretical studies for more than 25 years. A few representative studies are mentioned here.

Kerley [1989a] has constructed a pseudo-equilibrium model for calcium carbonate including a treatment of solid-solid interactions and melting. The thermodynamic properties of each of the four solid polymorphs are calculated from the ion-ion interactions and lattice vibrational motion, while those of the fluid phase are calculated using fluid perturbation theory. Phase boundaries in pressure - temperature space are then evaluated by minimizing the Gibbs free energy. Agreement with experimentally determined boundaries is achieved by introducing energy shifts for the respective phases. The resulting phase diagram, shown in Fig. 1-1, illustrates the relations of the four calcite phases of primary concern in this paper, labelled as $CaCO_3$ I, II, III and VI.

$CaCO_3$ I, or calcite, is rhombohedral [e.g. Hurlbut and Klein, 1977], with an ambient density of 2.71 gm/cm^3. It is stable under ambient conditions. Aragonite, an orthorhombic phase which is stable under stresses of 0.1 - 0.3 GPa at room temperature [Bell and England, 1964], is also found under ambient conditions (pearls, for example, are aragonite). Its ambient density is 2.93 gm/cm^3. Kerley [1989a] equates $CaCO_3$ VI with arago-

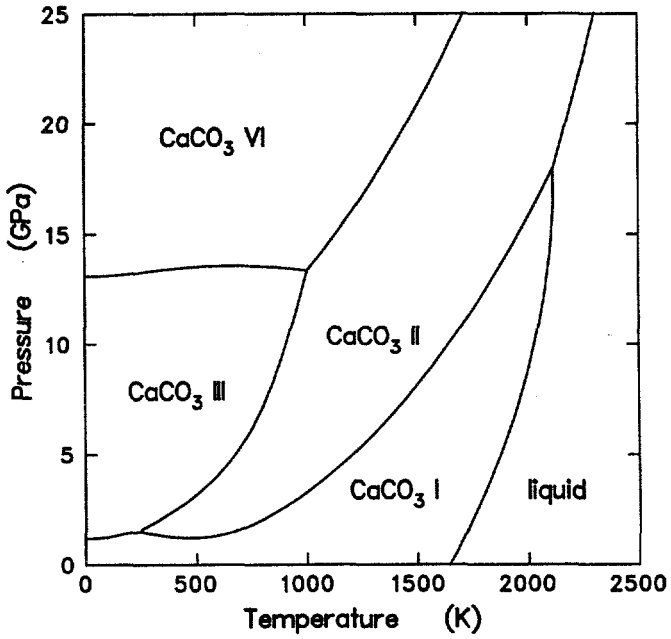

Fig. 1-1. Phase diagram of $CaCO_3$, adapted from Kerley [1989], representing a pseudo-equilibrium model

except for a fixed energy shift. $CaCO_3$ II and III are intermediate phases with monoclinic structures (P2 or $P2_1$ for $CaCO_3$ II and C2, Cc or C2/c for $CaCO_3$ III [Merrill and Bassett, 1972, 1975]. They have no field of stability under equilibrium conditions, but are observed under both static and dynamic conditions [Carlson, 1983].

Fully dense calcite exhibits signatures of transitions amongst the phases mentioned above. Two impact studies by Grady et al [1976a, 1978, 1983] used velocity interferometry diagnostics to measure the waveforms of shock/release cycles propagated through calcite, Blair dolomite, Oakhall limestone and Vermont marble. All of the samples were of very low porosity ($\phi > 0.5\%$). Over the stress range 0 - 4 GPa, both loading and rarefaction shocks were found in the calcite mineralogies. These appear to be related to transitions among the $CaCO_3$ I, II, and III set of structures.The dolomite samples did not show such marked rarefaction shocks, and the precursors were overrun at lower stress levels (consistent with smaller volume changes amongst the responsible transitions than for the analogous calcite transitions). The dolomite samples, however, showed a more marked rate dependence below their yield stress (about 2.5 GPa) than did the calcite samples [Grady et al, 1976b], a phenomenon attributed to rate dependent friction in previously closed cracks. A higher-stress (11 - 26 GPa) set of experiments performed by Grady et al. [1986] on Z-cut Iceland Spar calcite showed marked rarefaction shocks, consistent with the $CaCO_3$ VI$\rightarrow$ III transition.

Impact experiments over the range 0 - 40 GPa were conducted on C-cut aragonite ($CaCO_3$) by Vizgirda and Ahrens [1987]. These experiments used streak camera/tilt mirror diagnostics, providing precursor, Hugoniot and fully released states. They observed a phase transition on loading at between 5.5 and 7.6 GPa, with the Hugoniot approaching that of calcite at stresses over 10 GPa, suggesting that $CaCO_3$ VI might not be aragonite.

Static stress studies have been performed on the $CaCO_3$ system by several workers. Of

particular note for purposes of the present study, Singh and Kennedy [1974] used a piston-cylinder apparatus to measure calcite compressibility to 4 GPa, producing stress - volume curves for $CaCO_3$ I, II and III.

Porosity introduces additional phenomena to static and dynamic compression behavior. Heard et al [1974] compressed porous Indiana limestone (14% interconnected porosity) to 1.4 GPa (hydrostatic conditions) and 3.9 GPa (nearly hydrostatic conditions). Dry, 50% saturated and 100% saturated samples were tested. Although a transition beginning at 1.15 GPa was observed (probably $CaCO_3$ I $\rightarrow$ II), effects related to the porosity and water content were important. For example, a second transition near 2 GPa is likely to have been due to transitions in both $CaCO_3$ and water. Also, the irreversible 3% volume loss experienced for the saturated samples compressed to >2 GPa may be due to a combination of pore crushing (incompletely saturated occluded pores) and unrecovered phase transition.

The Hugoniot experiments of Kalashnikov [1973] surveyed the stress region 1 - 120 GPa for a variety of initial densities and compositions. Calcite, dolomite, magnesite and chalk were used as starting materials. The $CaCO_3$ portion of his results is summarized in Fig. 1-2. For stress levels above about 10 GPa, linear U_s/U_p relations provide a good description of these materials. At such stress levels, the effect of porosity is to introduce an offset to the pressure-particle velocity Hugoniots. Porosity-related thermal offsets in the pressure-density plane suggest that the Grüneisen γ is important.

Prior to the present study, releases from low pressure (less than 10 GPa) shock waves had only been measured for extremely low-porosity materials (porosity $\phi < 0.5\%$) and only over the range 0 - 4 GPa. Geotechnical applications require measurements of releases for material with porosity in the 10-20% range; only Murri et al. [1975] report release data for such material. Their experiments were limited to shock states in the range 11 - 31 GPa. One goal of the present study was to provide Hugoniot and release states for 18% porous

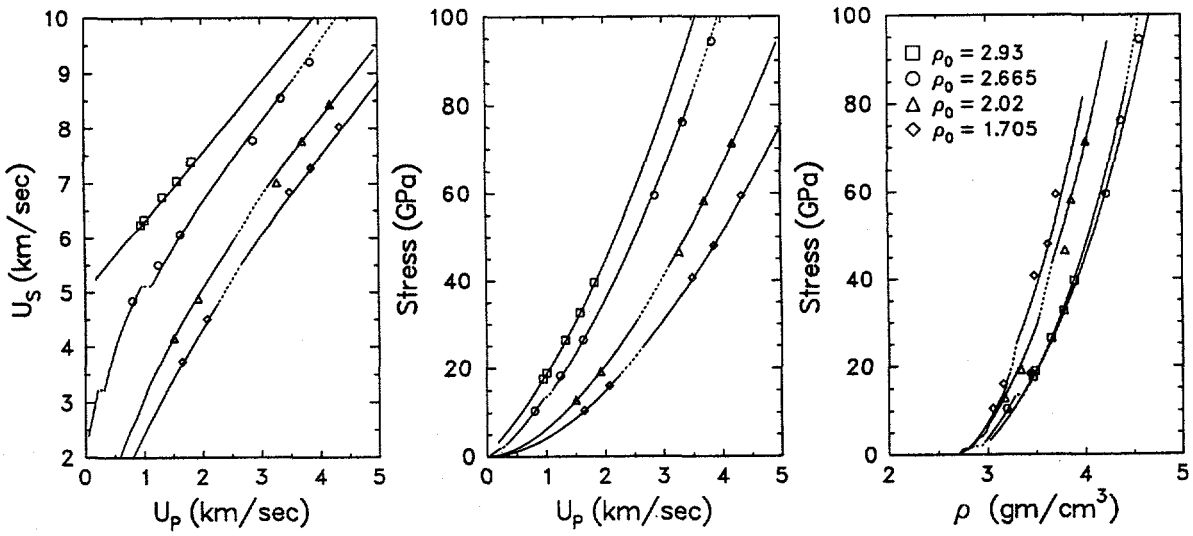

Fig. 1-2. $CaCO_3$ shock velocity - particle velocity results of Kalashnikov [1973], superposed on PANDA models of Kerley [1989].

limestone shocked to pressures in the 1 - 10 GPa range.

Water/calcite reactions may form $CaCO_3 \cdot 6H_2O$ (mineral name ikaite) from calcite, aragonite and water under stresses above 0.6 GPa at room temperature [VanValkenburg et al, 1971; Marland, 1975]. Ikaite is approximately 20% denser than the corresponding calcite and water combination in its stability field; its formation is expected to have a significant effect on the compression curves of water/calcite mixtures. The material is a named mineral because of natural occurrences in a Greenland fjord where temperatures are sufficiently low that the stability field of ikaite is reached. A significant question addressed in this study is whether such a reaction can occur rapidly enough to affect shock properties.

1.3 Scope of this study

This study focuses on several of the physical properties measurements required to constrain groundshock calculations. The properties assessed in parts of this work include:

- Hugoniot measurements and release paths of water-saturated and dry moderately porous limestone
- Hugoniot measurements and release paths of a low porosity marble
- Precursors and loading structure (dependence on dolomitization, porosity)
- Effect of temperature (frozen vs. ambient) on dynamic properties
- Whether hydration reactions occur on a microsecond timescale in water/calcite combinations

A variety of carbonate materials have been studied in the course of this work. They are assembled into a single report as dynamical properties measurements on carbonate materials using a common set of experimental methods. A summary of the tests conducted is presented in Table 1.1. Detailed descriptions of the samples will be presented in the respective sections.

Table 1.1. Dynamical Properties Test Series Conducted on Carbonate Rocks

Series (Shot designators)	Stress (GPa)	Experimental Suite[1]	Comments
Indiana Limestone (ILS; DLS)	1 - 12	17 RB, 4 FB	18% porosity. 9 dry, 15 wet. Very good data. Bedford quarry, Indiana
Limestone (JL)	4 - 20 GPa	9 FB; 1 RB	Saturated. Compare EOS of frozen and warm Ft. Knox limestones UTP Boring CB-7, 601.2-602.3 ft.; 642.3-642.9 ft. for Louisville Fm.; 523.2-523.45 ft. for Jeffersonville Fm

1. RB = reverse-ballistics; FB = forward-ballistics (see Section 2)

Table 1.1. Dynamical Properties Test Series Conducted on Carbonate Rocks (Cont'd)

Series (Shot designators)	Stress (GPa)	Experimental Suite	Comments
Marble (DM)	10 - 100	2 FB; 4 RB	Assess precursor and EOS. Dry Samples of Montclair Danby, Vermont Marble, Proctor, VT
UTTR Limestone (UT)	2 - 10	5 FB	Low porosity. CM02 drill hole (118' 4.2 - 7.3"). Density ~2.67 gm/cm^3.

2.0 Experimental Techniques

The present section contains a brief review of the experimental techniques used for dynamic materials properties measurements on carbonate materials. More detailed discussions of wave interactions, data reduction methods and uncertainties may be found in Furnish [1993a, b] and Grady and Furnish [1988]. Details of data reduction methods will be presented where appropriate in the remainder of this report.

The overall field of material properties measurements under high strain-rate loading and unloading has advanced greatly in recent years. Time-resolved interferometry techniques [Barker and Hollenbach, 1971; Chhabildas, 1987] have proved invaluable for measuring shock wave structures. In addition to Hugoniot data, it has become possible to obtain information about yield strengths, shock viscosity, release trajectories, multiwave structures, spall properties and the strength of materials in the shocked state [Davison and Graham, 1979]. Techniques have been developed to determine the dynamic material properties at strain rates of 10^5 to 10^{10} sec^{-1} at stresses ranging from less than 1 GPa to about 250 GPa. In particular, rate-dependent effects and release hystereses can be characterized [Furnish et al, 1992]. These sets of data are crucial in evaluating strain-rate-dependent viscoplastic or viscoelastic material models.

2.1 Considerations for impact studies of geological materials

The impact characterization of geological materials poses special challenges. Most importantly, samples are likely to contain heterogeneities (mm or larger scale). These affect experiments in several ways. Often a buffer must be used between the sample and the diagnostic to protect the diagnostic from the effects of an uneven shock, as well as to average a signal passed through the heterogeneous sample. Samples must be selected with an eye toward having results represent the bulk of the available material, but at the same time the samples must be uniform enough to allow a meaningful experiment (restrictions which may be difficult to simultaneously satisfy). Sample selection generally favors the most homogeneous and competent samples, and as such may bias the results of any dynamic study of these materials.

The effects of heterogeneities are more important at lower pressures. As interest shifts from groundshock behavior at high stress levels (σ > 100 kb) to groundshock behavior in the stress region only slightly above the elastic limit (σ ~ 1 kbar), both small-scale inhomogeneities such as selectively altered crystals and large-scale inhomogeneities such as joint systems become important.

Often water is an important component of the material of interest. When it is, the experiment may need to isolate the sample from vacuum, and possibly from gauges or reflective films as well. The sample may need to be machined without being allowed to dry. If the sample location is above the water table, the sample may be partially saturated. Such partial saturations are extremely difficult to maintain, and the only practical avenue may be to choose an end-member saturation for the tests.

Other important experimental considerations for natural samples may include a need to preserve volatiles content (especially water), friability of a specimen rendering difficult its fabrication into a usable gas-gun sample, and whether the sample can withstand the kilo-gravity to megagravity environment of a gun launch without damage.

2.2 Experimental configurations of interest

2.2.1 Forward ballistic (transmitted wave) configuration

In the most generally usable configuration for gas-gun testing, the sample is placed in the target (Fig. 2-1). This configuration is especially appropriate for measuring loading wave

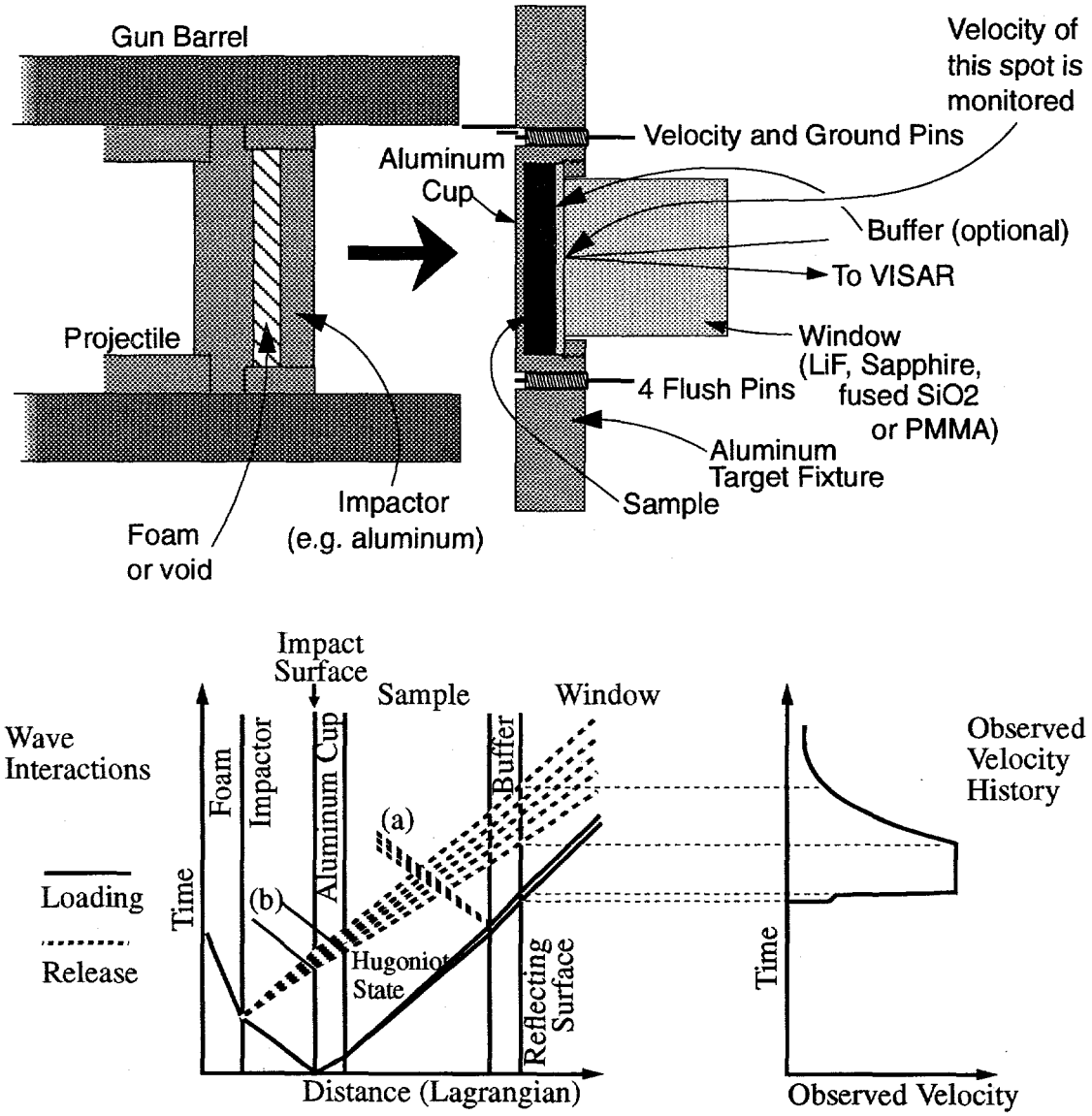

Figure 2-1. Forward Ballistic Configuration
(a) Release or reshock from sample/buffer interface
(b) Reshock(s) from sample/cup/impactor interfaces

profiles, Hugoniot states and strength properties (Hugoniot Elastic Limit for loading, the strength at the Hugoniot state, and the tensile or spall strength). If a window material can be chosen which is an approximate shock impedance match for the sample (such as Z-cut sapphire for iron, or lithium fluoride for slate or granite), a continuous release path may be measured; otherwise the pressure and particle velocity of a single point on the release (or reshock) of the sample may be determined. If a window material is chosen which has a much lower shock impedance than does the sample, spall properties of the sample may be measured as well as Hugoniot properties.

Analysis of the velocity profile from such a test consists of determining the precursor and Hugoniot states from the transit time across the sample (hence velocity of the observed waves), then extracting available release or spall information [Furnish, 1993a]. If the window is a fairly close impedance match to the sample and the waveforms entering and leaving the sample are known (easiest if no buffer is used), Lagrangian integration of the wave velocities yields a table relating stress, strain, time, shock velocity and wave velocity [Furnish, 1992]. For many materials, the strain rate during loading varies approximately as the fourth power of the Hugoniot stress [Swegle and Grady, 1985]. If buffers are used, wavecode modeling of the experiment to match the observed waveform may yield the pressure-volume path, although this procedure is somewhat more laborious. If the window is a poor impedance match for the sample, the average amplitude of the waveform "plateau" may be used with the Hugoniot of the window to calculate a single partial release or reshock state of the sample. Finally, if the sample has spalled, the amplitude of the pull-back signal may yield the spall strength of the sample [Chhabildas, et al, 1990].

2.2.2 Reverse ballistic configuration

For conditions where a window matching the shock impedance of the sample cannot be found, Hugoniot and continuous release paths may be measured using the geometry shown in Figure 2-2. Wave interactions and a typical velocity history are indicated. This configuration, called "reverse-ballistic," has been used extensively for measuring Hugoniot and release properties of rocks and grouts. It may be used with water-saturated samples (as may the forward-ballistic configuration). It does not give any information about loading characteristics, such as precursors and material strength, and in fact may give misleading results if incorrect assumptions about these quantities are made [Furnish, 1993a]. Under certain conditions, however, a family of such tests can be used to determine precursor conditions. It is normally most useful if the dynamic strength of the material is small compared to the Hugoniot stress.

The wave interactions for this type of test are presented in Figure 2-3 in a perspective format which may further clarify them for the interested reader. Interface motion as a function of time is shown by the dashed lines, although the scale is too coarse to indicate the details of a velocity vs. time profile. It is worthwhile bearing in mind that the aluminum/lithium fluoride interface is the location monitored by velocity interferometry. Note especially that the sample is subjected to a simple load/unload cycle (contrary to the suggestion from the velocity profile that two plateau states are reached).

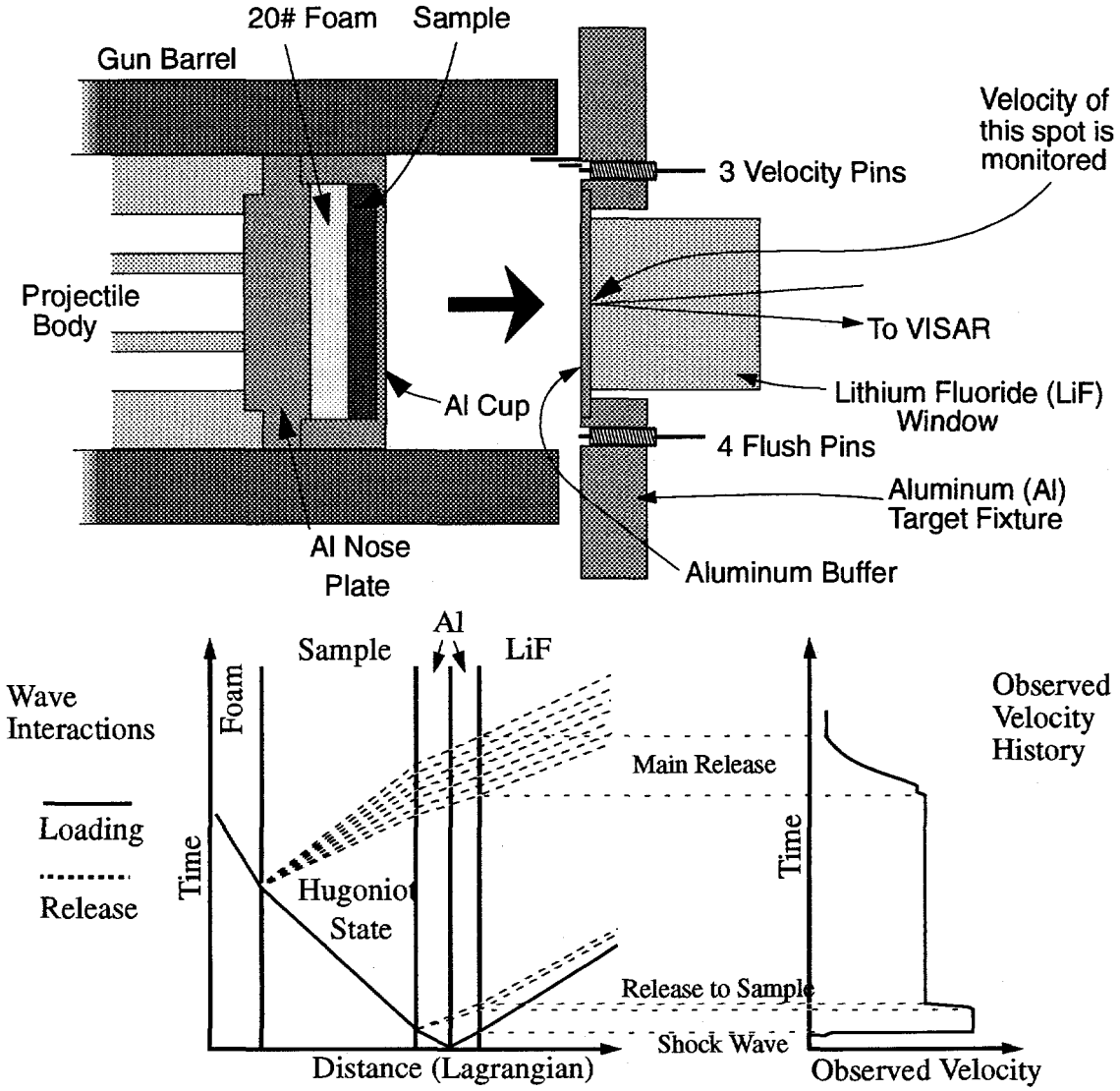

Figure 2-2. Reverse Ballistic Configuration

2.3 Strengths and limitations of gun impact tests for EOS measurements

Let us make several general comments about gas-gun tests (where the term "gas gun" here includes powder guns and 2-stage light gas guns as well as compressed-gas guns). Fundamentally these tests are uniaxial tests of hand-specimen-sized samples. As such, they cannot readily assess large-scale properties of heterogeneous bodies, nor can they directly assess the effects of wave divergence (such as the role of hoop stresses in reducing mean stress and causing pullback). Various studies have been performed to assess the roles of heterogeneities, generally aimed to model or observe a system with one or a few simple structures, although the behavior of families of these features under high strain rates remains unclear (but of considerable importance for stresses near the elastic limit of these materials).

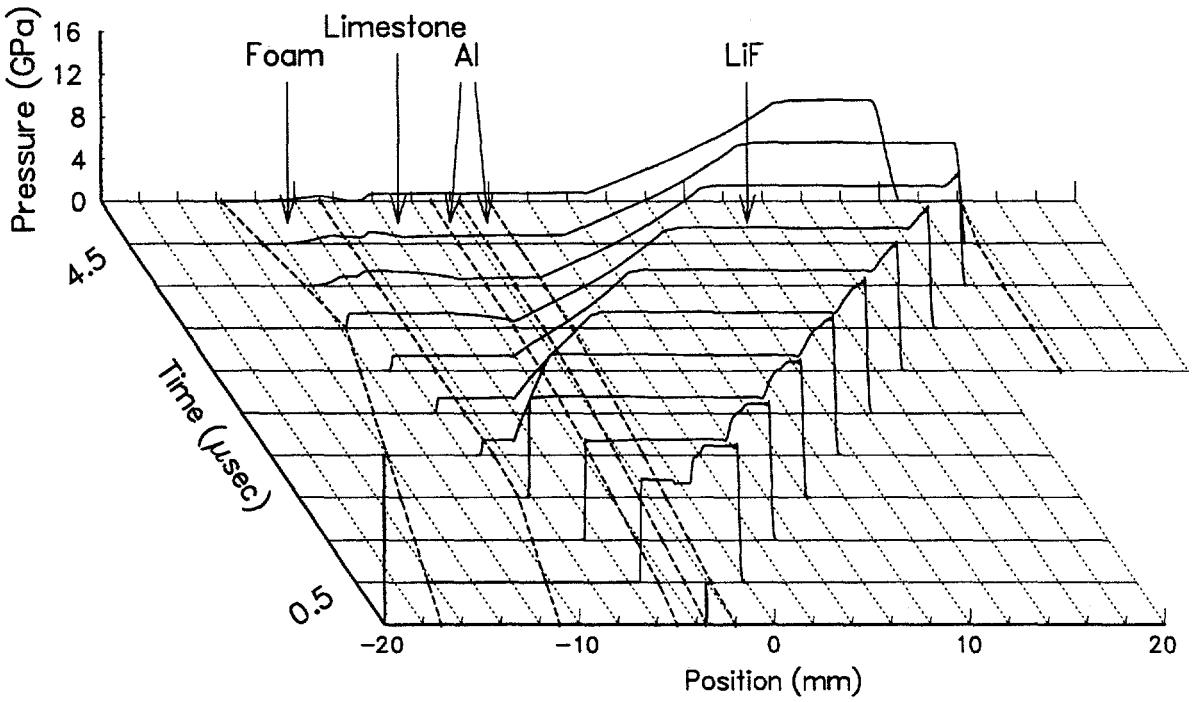

Figure 2-3. Wave interaction profile perspective for test ILS-3 (see Section 3). Stress as a function of time and position calculated by WONDY V Lagrangian finite-element wavecode (see Section 3).

Wave divergence effects may be assessed with actual divergent wave environments. While such environments can be produced from impact experiments (e.g. propagating a shock along a rod), the more traditional divergent wave experiments (exploding wire or point charge) may allow a more straightforward relation to physical systems of interest.

On the other hand, gas-gun tests conducted to separate shear and longitudinal properties may be useful experiments for benchmarking individual parameters in material models for calculating nonplanar wave behavior. These tests normally require generating a plane shear wave by a tilt-impact or anisotropic shock-processing material (e.g. Y-cut quartz), then coupling this wave into the sample and out at the other side. For geologic materials, this coupling is difficult and hard to ascertain. When such experiments can be made to work, they can constrain a large set of physical parameters describing the dynamic behavior of the material [Aidun and Gupta, 1989]. They are able, as well, to separate volume effects (such as phase transitions) from strength- and Poisson's ratio- effects such as the Hugoniot elastic limit and strength effects upon release. These effects generally cannot be separated in a simple longitudinal wave impact experiment.

Stresses are limited by the ability of window materials to remain transparent. The most common window materials in use, and their useful stress limits, are lithium fluoride (160 GPa +) [Wise and Chhabildas, 1985], Z-cut sapphire (elastic to 14 GPa; may recover transparency above 50 - 60 GPa) [Barker and Hollenbach, 1970], PMMA (20 GPa; has viscoelastic behavior) [Schuler and Nunziato, 1975], and fused silica (8 GPa; produces ramp wave below 3 GPa) [Barker and Hollenbach, 1970]. At low stress ranges (1 - 3 GPa), lithium fluoride is slightly affected by its elastic-plastic transition.

Within these constraints, gas gun tests are able to produce a wide range of materials properties data for materials undergoing high strain-rate deformation.

In summary, the waveform shown in Fig. 2-4 illustrates representative properties which can be obtained for metallic or stony geological materials (represented here for a forward-ballistic test).

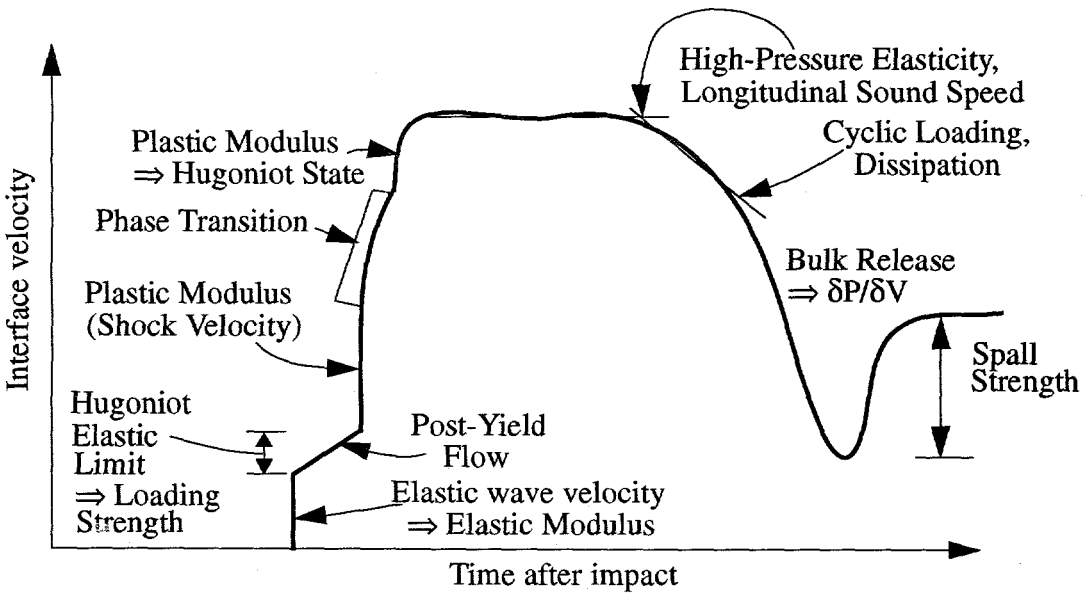

Figure 2-4. Correspondence Between Wave Features and Physical Properties

3.0 Indiana Limestone

3.1 Materials studied

3.1.1 Characterization

A large machined sample of limestone from the Bedford, Indiana quarries supplied the material for this study. It was obtained from Don Larson of Lawrence Livermore Laboratories, and is similar to the samples utilized in his [1988] studies of spherical shocks introduced by small charges. In general, this material is a high quality, fine-grained, uniform, nearly pure calcite limestone with about 18% porosity.

Helium pynchnometry and mercury porosimetry measurements were performed by Quantachrome Corp. to measure grain densities and pore size distributions, respectively. The helium pynchnometry experiments yielded grain densities of 2.70 gm/cm^3, close to that of pure calcite (2.71 gm/cm^3). Mercury porosimetry techniques were also applied. Intrusion pressures of 25 PSIA to 5980 PSIA were applied, with intruded volumes of mercury measured as a function of intrusion pressure. A wetting angle of 140^o was measured; these intrusion pressures were accordingly calculated to correspond to 4.27 μm (25 PSIA) to 17.8 nm (5980 PSIA). In the sample tested, approximately 50% of the pore volume occurred in pores of less than 330 nm diameter, and the total measured pore surface area was 0.72 m^2/gm (~1.6·10^4 cm^2/cm^3).

Ultrasonic mappings of longitudinal velocity and attenuation were performed to identify samples with significant heterogeneities. Samples with such heterogeneities were not selected for use in the gas gun tests. Among the samples used, longitudinal velocities ranged from 3.80 to 4.10 km/sec (variations within a single sample over 70 -80% of this range) and attenuations varied over 7 db (0.236" thick samples). Patterns in the variations corresponded to bedding patterns which appeared typical of those found in other competent limestones.

3.1.2 Saturation

Saturation was accomplished by evacuating the samples (submerged under 1 - 2 cm of water) in a bell jar, and then allowing pressure to return to room levels. This cycle was performed 2 - 4 times until no further bubble evolution was observed under evacuation. For this material, this method worked well, although for other materials such as zeolitized tuffs [Furnish, 1989] it has not worked nearly as well. The ease of saturation is an indication that dewatering/resaturation of the limestone is almost entirely a mechanical process; that chemically bound water does not play an important role.

Utilizing the grain density measurement described above, five samples were measured for porosity and saturation. Dry and saturated densities were measured for five disk-shaped samples (~65 gm wet weight each), resulting in the values shown in Table 3.1.

Table 3.1. Porosity and Saturation Values - Indiana Limestone Samples

Shot #	ρ_{Wet} gm/cm^3	ρ_{Dry} gm/cm^3	ϕ_{tot} %	ϕ_{H_2O} %	ϕ_{unsat} %
ILS1	2.375	2.195	18.70	18.00	0.70
ILS2	2.371	2.194	18.74	17.70	1.04
ILS3	2.380	2.200	18.52	18.00	0.52
ILS4	2.380	2.206	18.30	17.40	0.90
ILS5	2.381	2.208	18.22	17.30	0.92

ρ_{Wet} = Water-saturated density
ρ_{Dry} = Dry density
Values based on $\rho_{Grain} = 2.70$ gm/cm^3

ϕ_{tot} = total porosity
ϕ_{H_2O} = water-filled porosity
ϕ_{unsat} = unsaturated (occluded?) porosity.

3.2 Matrix of experiments conducted

A matrix of 23 tests was conducted to measure Indiana Limestone dynamic properties. Fifteen of these tests were conducted on water-saturated samples, with the remaining eight conducted on dry samples. Hugoniot stress levels ranged from 0.6 GPa to 12 GPa. 21 of these tests yielded limestone data. Detailed parameters are presented in Tables 3.2 and 3.3.

These experiments divide into the following categories:

(a) Reverse-ballistic release experiments, with aluminum cups and buffers and lithium fluoride windows (Figure 2-2) (ILS 1, 2, 3, 9, 10, 12 and 15).

(b) Reverse-ballistic release experiments, with fused silica cups, buffers and windows. These tests were confined to lower velocities because fused silica becomes opaque after passage of a shock of amplitude more than approx. 8.5 GPa (ILS 13, 14; DLS 1, 3, 4). At stresses below about 5 GPa, though, a ramp loading is delivered to the front of the sample (see Fig. 3-3).

(c) Reverse-ballistic tests with no cups. Only dry limestone could be tested in this configuration because exposure to vacuum desiccates the samples. Test DLS 6 used a LiF buffer and window; test DLS 8 used a fused silica buffer and window. The sample is subject to a sharp shock even if a fused silica buffer is used.

(d) Reverse-ballistic reshock experiments. All of these replaced the foam with 6061-T6 aluminum. Tests ILS 5 and 11 used aluminum cups and buffers and lithium fluoride windows; test DLS 5 used a fused silica cup, buffer and window; and test DLS 7 used a lithium fluoride buffer and window (no cup).

(e) Forward-ballistic (wave-transmission) experiments (Figure 2-1). The three tests conducted on water-saturated limestone (ILS 6, 7, 8) used aluminum impactors and cups, a void behind the impactor, and PMMA buff-

Table 3.2. Test Matrix for Impact Studies of Water-Saturated Indiana Limestone (18% Porosity)

Reverse Ballistic

Shot #	Gun Facility	Impact Velocity (km/sec)	Velocity Per Fringe (km/sec)[2]	Materials[1]			Densities (gm/cm^3)			Thicknesses (mm)					
				Cup	Buffer	Window	Foam	Sample Saturated	Sample Dry	Foam	Sample	Cup	Buffer	Window	Gap[3] Sam/Cup
ILS1	Powder	1.000	0.10889	Al	Al	LiF	0.287	2.375	2.195	6.020	6.011	1.489	1.523	25.460	0.143
ILS2	Powder	1.297	0.10889	Al	Al	LiF	0.287	2.371	2.194	6.08	5.996	1.487	1.514	25.173	0.092
ILS3	Powder	1.534	0.10889	Al	Al	LiF	0.285	2.380	2.200	6.05	6.008	1.490	1.513	25.405	none
ILS4	Powder	←	- - -	- - -	- - -	(No Fringes)	- -	2.380	- - -	- - -	- - -	- - -	- - -	- - -	→
ILS5	Powder	1.425	0.10889	Al	Al	LiF	(Al)	2.381	2.208	~6	6.002	1.478	1.510	25.399	none
ILS9	Gas	0.203	0.039539	Al	Al	LiF	0.291	2.382	2.206	6.025	6.001	1.505	1.533	25.309	none
ILS10	Gas	0.449	0.039539	Al	Al	LiF	0.295	2.382	2.206	6.125	6.001	1.515	1.520	25.428	none
ILS11	Gas	0.675	0.056502	Al	Al	LiF	(Al)	2.380	2.202	~6	6.000	1.434	1.518	24.879	0.173
ILS12	Gas	0.819	0.056502	Al	Al	LiF	0.282	2.379	2.201	6.030	5.998	1.514	1.514	25.341	0.041
ILS13	Gas	0.124	0.042173	(f)SiO_2	(f)SiO_2	(f)SiO_2	0.276	2.389	2.199	5.892	6.008	3.147	3.126	37.36	0.021
ILS14	Gas	0.840	0.069049	(f)SiO_2	(f)SiO_2	(f)SiO_2	0.276	2.385	2.195	5.877	6.010	3.205	3.173	38.148	none
ILS15	Gas	1.457	0.089823	Al	Al	LiF	0.276	2.378	2.194	5.931	6.012	1.554	1.592	25.374	none

Forward Ballistic[4]

Shot #	Gun Facility	Impact Velocity (km/sec)	Velocity per Fringe (km/sec)	Materials			Densities (gm/cm^3)			Thicknesses (mm)					
				Impactor	Cup	Buffer & Window		Sample Saturated	Sample Dry	Impactor	Sample	Cup	Buffer	Window	
ILS6	Gas	0.129	0.072322	Al	Al	PMMA		2.376	2.196	7.004	5.985	1.465	3.080	37.53	
ILS7	Gas	0.417	0.050880	Al	Al	PMMA		2.377	2.202	7.000	6.000	1.490	3.103	38.075	
ILS8	Gas	0.735	0.072353	Al	Al	PMMA		2.382	2.206	6.995	5.988	1.500	3.093	37.470	

Notes:

[1]Standard aluminum used is 6061-T6 throughout assembly; (f)SiO_2 is fused silica (GE Dynasil 2000).

[2]Velocity per fringe (VPF) corresponds to a setting of the VISAR.

[3]Unintentional; width inferred from wave profiles.

[4]In the forward-ballistic tests, the impactor is backed by a void.

Table 3.3. Test Matrix for Impact Studies of Dry Indiana Limestone (18% Porosity)

Reverse Ballistic

Shot #	Gun Facility	Impact Velocity (km/sec)	Velocity Per Fringe (km/sec)[2]	Materials[1]			Densities (gm/cm^3)			Thicknesses (mm)					
				Cup	Buffer	Window	Foam	Sample Saturated	Sample Dry	Foam	Sample	Cup	Buffer	Window	Gap[3] Sam/Cup
DLS1	Gas	0.338	0.064406	(f)SiO_2	(f)SiO_2	(f)SiO_2	0.275		2.202	5.920	6.017	3.068	3.141	38.185	0.055
DLS3	Gas	0.868	0.069049	(f)SiO_2	(f)SiO_2	(f)SiO_2	0.276		2.193	5.957	6.011	3.193	3.209	37.885	none
DLS4[4]	Powder	1.358	0.111085	(f)SiO_2	(f)SiO_2	(f)SiO_2	0.277		2.187	5.880	6.008	3.148	3.188	38.025	?
DLS5	Powder	1.116	0.111085	(f)SiO_2	(f)SiO_2	(f)SiO_2	(Al)		2.214	~6	6.012	3.101	3.136	38.153	none
DLS6	Powder	2.042	0.089823	None	LiF	LiF	0.276		2.202	5.958	6.015	---	3.094	25.365	n.a.
DLS7	Powder	1.586	0.089823	None	LiF	LiF	(Al)		2.212	~6	6.012	---	3.278	25.471	n.a.
DLS8	Powder	1.308	0.111085	None	(f)SiO_2	(f)SiO_2	0.277		2.213	5.953	6.015	---	3.269	38.175	n.a.

Forward Ballistic

Shot #	Gun Facility	Impact Velocity (km/sec)	Velocity per Fringe (km/sec)	Materials			Densities (gm/cm^3)			Thicknesses (mm)					
				Impactor	Cup	Buffer & Window		Sample Saturated	Sample Dry	Impactor	Sample	Cup	Buffer	Window	
DLS9[5]	Gas	0.424	0.071673	(f)SiO_2	(f)SiO_2	PMMA			2.198	6.404	6.006	3.086	1.624	37.03	

Notes:

[1]Standard aluminum used is 6061-T6 throughout assembly; (f)SiO_2 is fused silica (GE Dynasil 2000).

[2]Velocity per fringe (VPF) corresponds to a setting of the VISAR.

[3]Unintentional; width inferred from wave profiles.

[4]Light was lost on test DLS4 approx. 250 nsec after initial arrival; no data pertinent to sample EOS was acquired.

[5]In the forward-ballistic test, the impactor is backed by 6.127 mm of foam (density 0.1787 gm/cm^3)

ers and windows. The test conducted on dry limestone (DLS 9) used a fused silica impactor and cup and PMMA buffer and window. For DLS 9, the cup caused a slight degree of ramp loading of the sample, although the unloading of the sample could be described as a rarefaction shock, an especially clean form of release for modeling purposes.

3.3 Dynamic properties results

3.3.1 Observed velocity profiles

The first practical level of information provided by impact experiments using velocity interferometry as the primary diagnostic is the velocity profile. It cannot be interpreted without some detailed knowledge of the experimental configuration used; with such knowledge, however, it can provide a practical starting point for benchmarking numerical models.

For these tests, the velocity profiles are grouped according to the experiment types described in Section 3.2. The profiles are also shown separately in Section 3.3.2, juxtaposed on model curves.

Figure 3-1 shows the velocity profiles obtained from category (a); i.e. reverse-ballistic release experiments with aluminum cups and buffers and lithium fluoride windows. Four

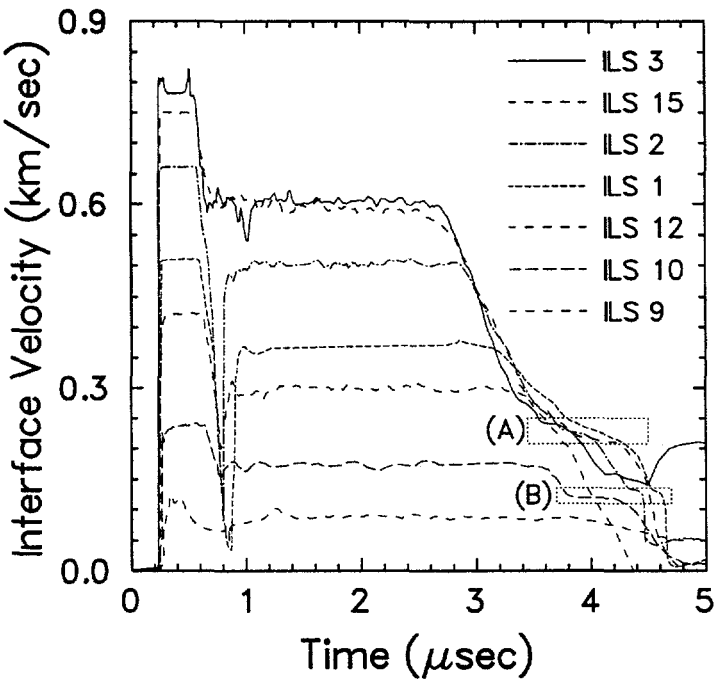

Figure 3-1. Velocity profiles for Category (a) experiments (standard reverse-ballistic). The samples are water-saturated Indiana Limestone for all tests here. Rectangles point out release structure; (A) is at stress of 4.0 - 4.9 GPa; (B) at 1.7 - 3.0 GPa. Captions are in same vertical order as velocity profiles.

of these tests show signatures of slight gaps formed between the sample and the cup; widths of these gaps calculated are shown in Table 3.2. These widths were calculated by estimating the release and reshock wave speeds in the cup and buffer, calculating the corresponding gap closure time, and assuming that closure occurs at the velocity of the projectile. Resulting values were refined in the course of simulation with the WONDY V wavecode (Section 3.3.2).

Timing these tests relative to impact was accomplished by choosing a translation in time which corresponds to wave speeds in the aluminum agreeing with an aluminum Hugoniot, $C_0 = 5.33$ km/sec, $S = 1.344$ and $\rho_0 = 2.703$ gm/cm^3.

Configuration (b) wave profiles are shown in Figure 3-2. These are reverse-ballistic release experiments, with fused silica cups, buffers and windows (ILS 13, 14; DLS 1, 3, 4).

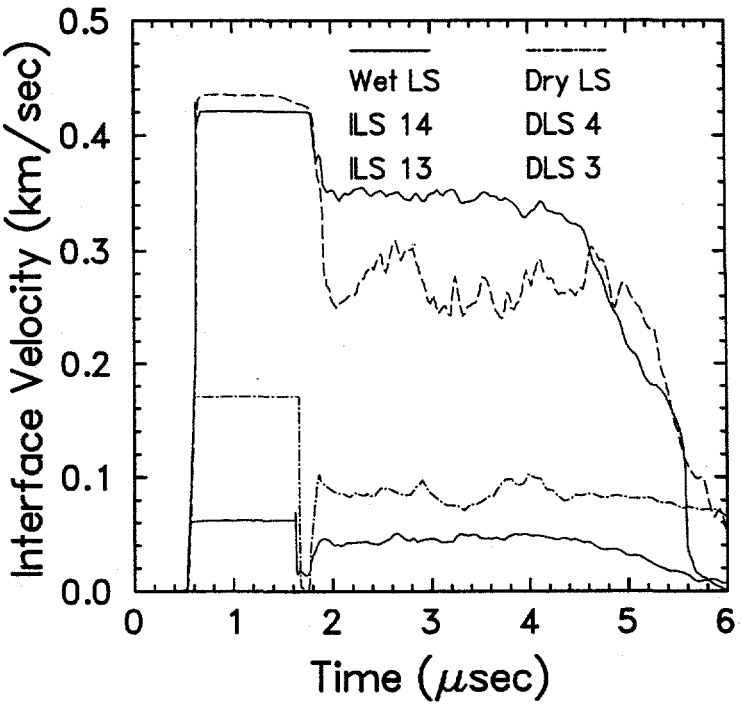

Figure 3-2. Wave profiles from reverse-ballistic release experiments using fused silica cups, buffers and windows. Captions are in same vertical order as velocity profiles for wet and dry tests (respectively).

At stresses below about 5 GPa, a ramp loading is delivered to the front of the sample. This is a consequence of the pressure/volume behavior of fused silica upon shock loading [Barker and Hollenbach, 1970):

$$\sigma = 77.60\varepsilon\cdot(1 - 5.5595\varepsilon + 39.098\varepsilon^2 - 89.252\varepsilon^3) \qquad (0 < \sigma < 9 \text{ GPa}) \qquad \text{(Eq. 3.1)}$$

Because the shock velocity is a decreasing function of stress for stresses to ~4 GPa, a ramp to this level is formed. At the highest stress levels (~9 GPa), the ramp is partly overdriven, with a transition to shock at ~2.5 GPa.

As an illustration of the ramp loading delivered to these samples, consider the loading profiles shown in Figure 3-3. These are enlargements of the profiles for the tests in the present series with fused silica buffers and windows. Since the cup and buffer thicknesses are comparable where fused silica cups are used, these profiles represent velocity histories delivered to the samples (with some vertical scaling for impedance mismatch). Juxtaposed on these is the predicted time-of-arrival for shock propagation through 3 mm of fused silica, using the stress-strain relation shown in Eq. 3.1. The present experiments agree quite closely with the Barker and Hollenbach predictions.

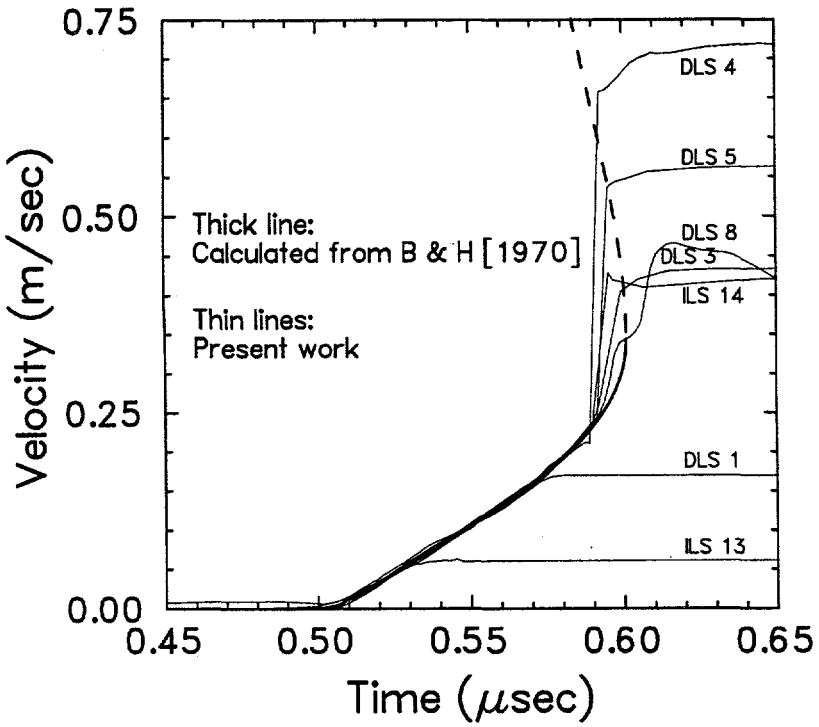

Figure 3-3. Velocity profile detail for initial arrival region of tests with fused silica buffers. Timing scaled for 3 mm thick buffer. Represents input to sample w/ fused silica cup. B & H [1970] refers to Barker and Hollenbach [1970]

Two experiments used configuration (c); i.e. reverse-ballistic tests with no cups. Wave profiles are shown in Figure 3-4. By contrast with configuration (b), which used a fused silica cup, the sample is subject to a sharp shock loading. Only dry limestone could be tested in this configuration because exposure to vacuum desiccates the samples. Test DLS 6 used a LiF buffer and window; test DLS 8 used a fused silica buffer and window.

The final group of reverse-ballistic test is that providing a reshock to the sample. Aluminum replaced the closed-cell foam behind the sample, providing the reshock. Four tests are included in this group. Tests ILS 5 and 11 used aluminum cups and buffers and lithium fluoride windows; test DLS 5 used a fused silica cup, buffer and window; and test DLS 7 used a lithium fluoride buffer and window (no cup). Velocity histories are shown in Figure 3-5.

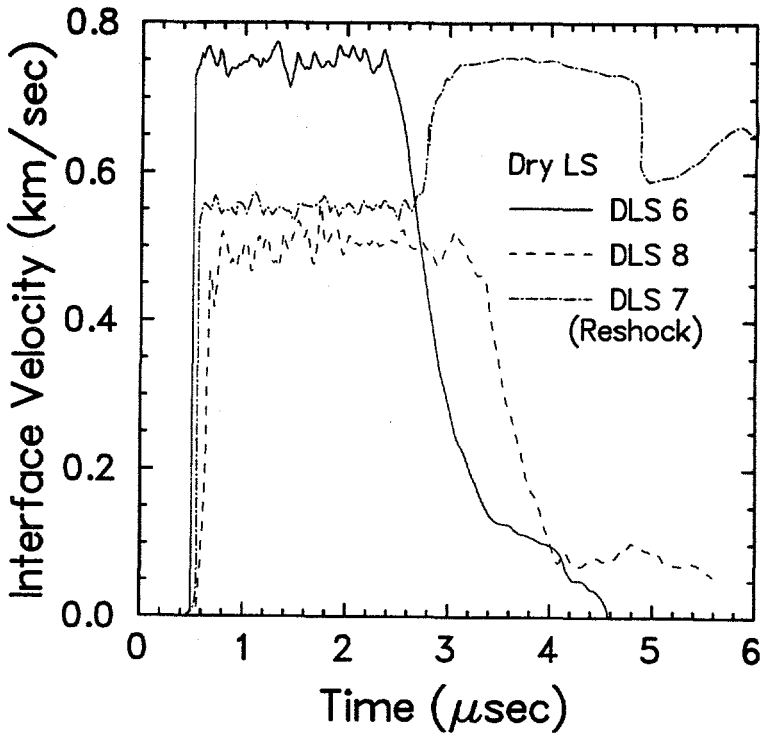

Figure 3-4. Wave profiles for reverse-ballistic tests with no cups. See Tables 3.2 and 3.3 for configuration details.

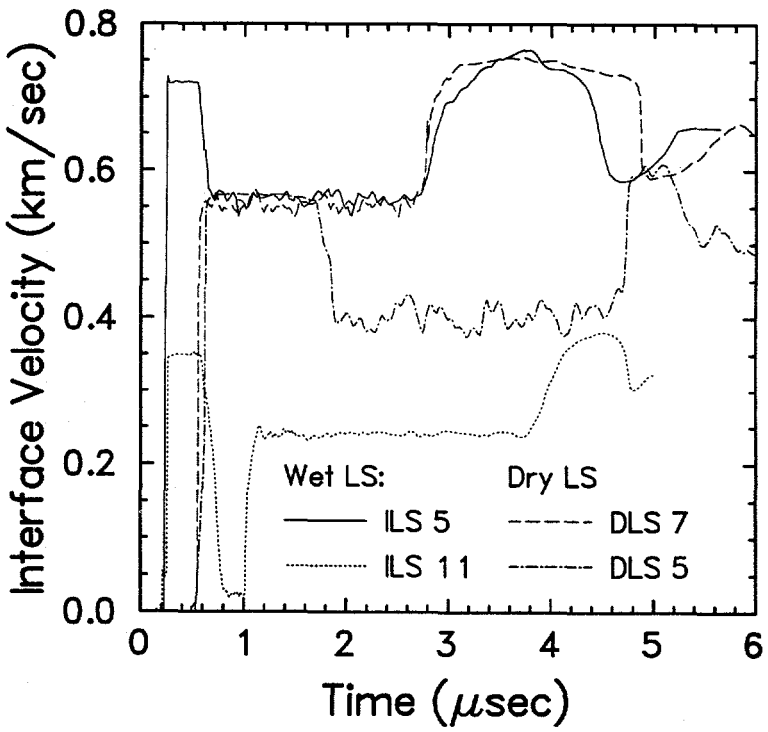

Figure 3-5. Wave profiles for reverse-ballistic reshock tests. See Tables 3.2 and 3.3 for configuration details. (Note duplication of DLS 7 from Fig. 3-4.)

Four tests were performed in a transmitted-wave mode (configuration (e); see Figure 2-1). All used PMMA buffers and windows. The test conducted in this configuration on dry limestone (DLS 9) used a fused silica buffer and cup to provide a rarefaction shock release input to the sample. This was done at the cost of providing a ramp loading (as discussed above). The three tests performed on water-saturated limestone (ILS 6, 7, 8) used aluminum impactors and cups. These three tests had voids behind the impactor; by contrast, DLS 9 had 20 lb./ft^3 foam behind the impactor. Resulting velocity profiles are shown in Figure 3-6.

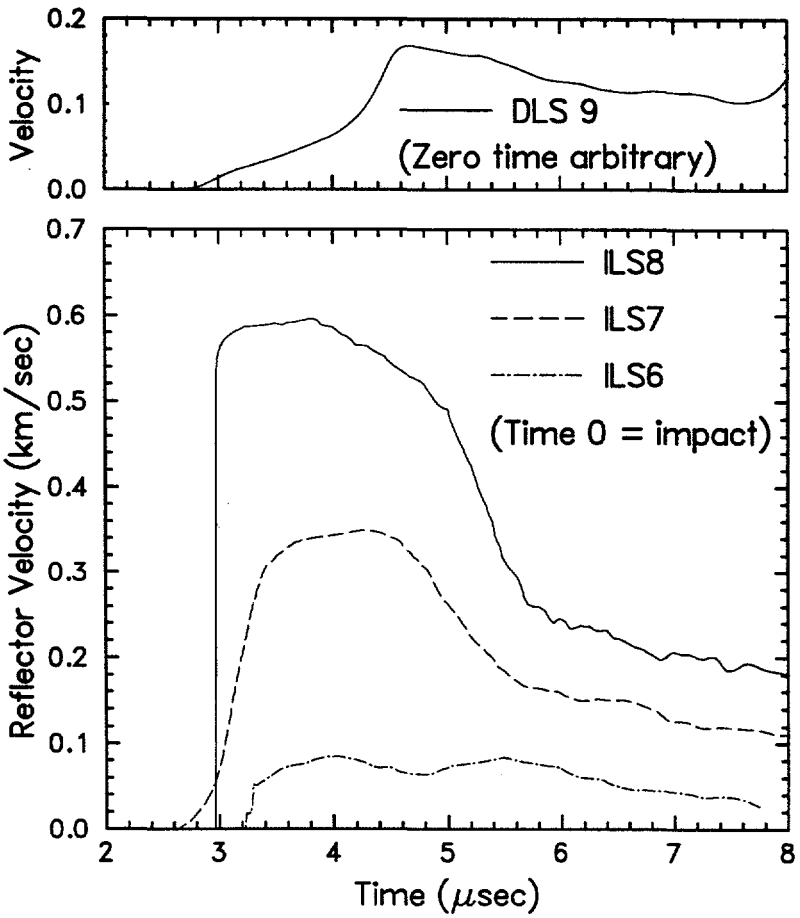

Figure 3-6. Wave profiles for forward-ballistic tests. Timing for DLS 9 is arbitrary; others are timed so that impact occured at zero (as with other traces in this report).

3.3.2 Loading, Hugoniot and release/reshock paths

Transmitted-wave tests: Precursor and Hugoniot conditions

Let us start with interpretation of the forward-ballistic tests. This is prudent because knowledge of the loading structure, provided by such experiments, is necessary for properly interpreting the reverse-ballistic experiments as well.

Details of the reduction method are presented in Furnish [1993a, b], and are briefly summarized here. Calculation of the Hugoniot and partial release/reshock states proceeds as

illustrated in Figure 3-7. For this configuration, the Hugoniot state in stress/particle velocity space is calculated from the shock arrival time at the window (hence the shock velocity in the material). Assuming there is no precursor, this state lies at the junction between the line $\sigma = (\rho_0 U_s)U_P$ and the aluminum release from the Al/Al impact state. If there is a precursor, both the shock velocity $U_{s(p)}$ and particle velocity $U_{P(p)}$ of the precursor state must be determined. $U_{P(p)}$ may be estimated from the observed interface velocity after passage of the precursor, using the fact that the precursor state must lie on the line $\sigma_{(p)} = (\rho_0 U_{s(p)})U_P$ and assuming that a release of the same slope magnitude connects this state to the observed precursor state transmitted into the PMMA. The Hugoniot state then lies on the intersection of the line $\sigma = [\rho_p(U_{sH}-U_{P(p)})](U_P-U_{P(p)})$ with the same aluminum release as before.

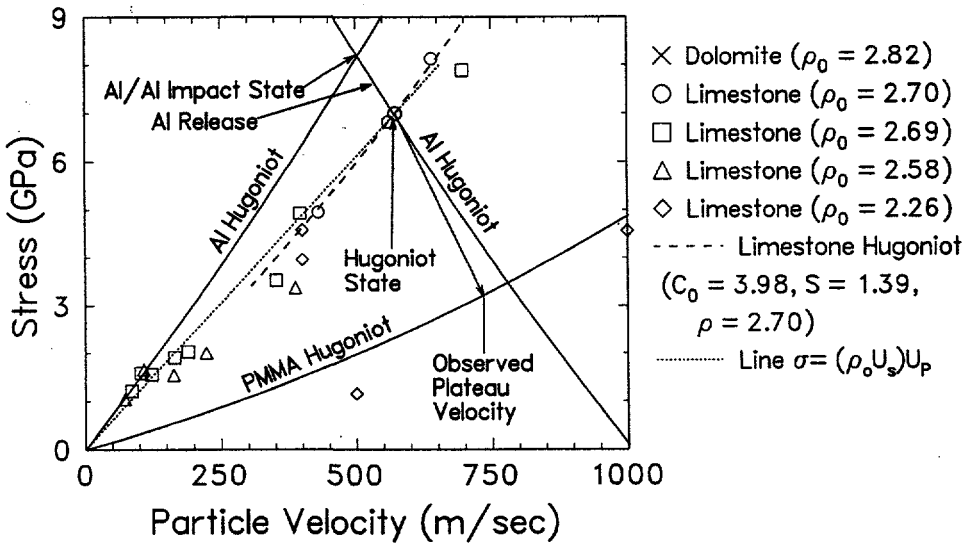

Figure 3-7. Calculation of Hugoniot and partial released states for forward-ballistics experiment. Sample used is a dolomitized limestone (test PF-3; $\rho_0 = 2.786$ gm/cm^3; aluminum impactor and cup; PMMA buffer and window, 1008 m/sec impact velocity; see Section 4).

For the experiment of Figure 3-7, the sample was immediately released to approximately half of the Hugoniot stress by the release (a) (in Fig. 2-1). The stress/particle-velocity state of this release lies on the PMMA Hugoniot, as shown in Fig. 3-7. The density of this state cannot be determined from this experiment because a continuous stress/particle velocity curve from the Hugoniot point to the partially released state is not available and the necessary Riemann integration cannot be performed:

$$\int_{\sigma_{Hug}}^{\sigma_{Rel}} \left.\frac{\partial U_P}{\partial \sigma}\right|_S d\sigma = -\int_{U_{P(Hug)}}^{U_{P(Rel)}} \left.\frac{\partial V}{\partial U_P}\right|_S dU_P = V_{Rel} - V_{Hug} \qquad \text{(Eq. 3.2)}$$

This particular experiment illustrates the need to estimate the sample EOS prior to constructing the experiment; here, we were surprised by how high the material density was and might have more profitably used lithium fluoride windows and buffers (whose Hugo-

niot is slightly softer than that of aluminum).

The resulting values for the water-saturated Indiana limestone are tabulated in Table 3.4, together with the input values measured. Because timing could not be determined for the transmitted-waveform test on dry limestone, results of that test have been omitted.

Table 3.4. Precursor and Hugoniot values from transmitted-wave experiments on Indiana limestone.

				Precursor/Hugoniot Conditions					
Shot #	Proj. Velocity km/sec	Plastic TOA μsec	ρ_0 gm/cm^3	Particle Vel km/sec	Pressure GPa	ρ gm/cm^3	Shock Vel. km/sec	ρ/ρ_0	Specific Vol cm^3/gm
ILS 6	0.129	3.29	2.376						
	Precursor Conditions →			0.064	0.501	2.423	3.369	1.0198	0.4127
	Hugoniot Conditions →			0.082	0.624	2.438	2.970	1.0261	0.4102
ILS 7	0.417	3.15	2.377						
	Precursor Conditions →			0.000	0.000	2.377	0.000	1.0000	0.4207
	Hugoniot Conditions →			0.268	2.023	2.565	3.180	1.0791	0.3899
ILS 8	0.735	2.97	2.382						
	Precursor Conditions →			0.000	0.000	2.382	0.000	1.0000	0.4198
	Hugoniot Conditions →			0.470	3.680	2.780	3.285	1.1671	0.3597

	Partial Release Conditions		
Shot #	Plateau Velocity	Stress	Particle Vel.
ILS 6	0.152	0.531	0.152
ILS 7	0.345	1.267	0.345
ILS 8	0.590	2.430	0.590

These values will be plotted together with the values from the reverse-ballistics tests (Figures 3-9 and 3-10).

There are no clear precursors apparent in these data. Some of the waveforms (ILS 7 and DLS 9) are dispersed; this may be a consequence of yielding at the 0.2 - 0.3 GPa level. Fully-dense limestones typically produce precursors at about 1.4 GPa amplitude (see Sections 4 - 6 of this report). Such a precursor in the present tests would have an amplitude of about 0.25 m/sec (observed plateau velocity); there is no evidence of a precursor near this amplitude. The porosity (18%) of the present samples might explain a lack of a pronounced precursor, whether strength-related or phase-transition related. This will be discussed further in the interpretation of the reverse-ballistics tests.

Reverse-Ballistic Tests: Hugoniot conditions

Hugoniot data are derived from these profiles by standard impedance-match methods [McQueen et. al. 1970; Grady and Furnish, 1988] (Figure 3-8). Information required is the projectile velocity, the initial sample density and the velocity level of the long plateau in the observed velocity profile. In addition, the Hugoniot and release properties of the cup and window materials are required, although these are known to good precision for materials such as aluminum and lithium fluoride (better than 1 percent stress at a given particle velocity over the range 6 - 150 GPa).

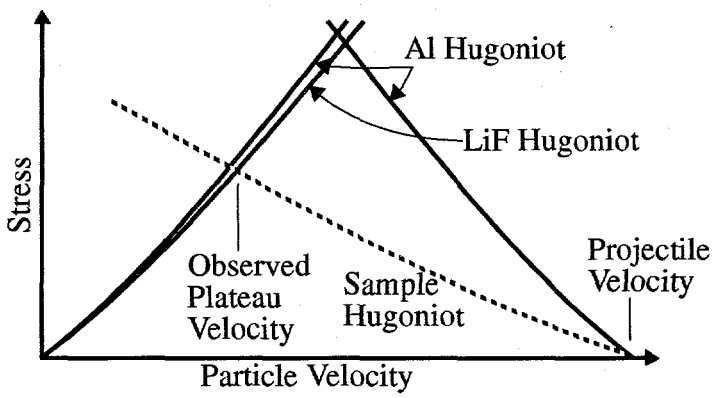

Figure 3-8.
Impedance match diagram for standard reverse-ballistics configuration.

Provides σ, U_p
If loading wave is steady, then:
$U_s = \sigma/\rho_0 U_p$
$\rho = \rho_0 U_s/(U_s-U_p)$

This impedance-match procedure is generally similar for those experiments using fused silica components, and is simplified somewhat for experiments omitting a cup. It is necessary to calculate the stress-particle velocity relations for fused silica from Eq. 3.1. Details will not be discussed here.

The resulting values are tabulated in Table 3.5 and plotted in Figures 3-9 and 3-10. The Figures also show release paths and reshock points, which will be further discussed later in this Section. As noted in the Table, these values assumed no precursors. Alternate calculations were made assuming a 1.4 GPa precursor barely ahead of the observed arrivals; this had a significant effect on the Hugoniot points. These results are plotted as squares in Figures 3-9 and 3-10. I do not feel that these points are physically meaningful.

The Hugoniot results and release paths are juxtaposed on theoretical curves due to Kerley [1990], constructed to represent the Hugoniots for water-saturated 18% porosity calcite undergoing a partial transformation to ikaite ($CaCO_3 \cdot 6H_2O$), the same mixture with no water-calcite reactions, and dry 18% porosity calcite.

One particularly interesting feature may be noted in these Hugoniot plots. The Hugoniot data for the water-saturated samples show reasonable agreement with the model curve corresponding to ikaite production, but not with the curve assuming no water-calcite chemical reactions. Since ikaite is not stable under ambient pressure/temperature conditions, it must have been produced during the experiment, i.e. on a microsecond time scale. This is not an unreasonable time scale in view of the large water-calcite contact area (see Section 3.1.1).

The issue of strength also deserves comment. The plot of shock velocity vs. particle veloc-

Table 3.5. Hugoniot conditions for reverse-ballistic tests on Indiana Limestone.

Water-saturated limestone:

				Hugoniot Conditions					
				Particle			Shock		Specific
Shot #	Proj. Velocity km/sec	Observed Vel. km/sec	ρ_0 gm/cm^3	Vel km/sec	Pressure GPa	ρ gm/cm^3	Vel. km/sec	ρ/ρ_0	Vol cm^3/gm
ILS 1	1.00(1)	0.368(4)	2.375(3)	0.641(11)	5.65(9)	2.87(3)	3.71(10)	1.209(11)	0.348(3)
ILS 2	1.30(1)	0.502(3)	2.371(3)	0.808(14)	7.92(10)	2.94(3)	4.14(9)	1.243(13)	0.229(3)
ILS 3	1.53(1)	0.601(4)	2.380(3)	0.948(16)	9.76(12)	3.05(3)	4.33(10)	1.280(14)	0.328(4)
ILS5	1.42(1)	0.561(5)	2.381(3)	0.878(15)	9.02(13)	2.99(3)	4.31(11)	1.255(13)	0.335(4)
ILS 9	0.210(2)	0.088(3)	2.382(3)	0.125(4)	1.26(5)	2.454(7)	4.24(27)	1.030(3)	0.417(1)
ILS 10	0.449(5)	0.173(3)	2.382(3)	0.281(6)	2.54(5)	2.573(11)	3.78(13)	1.080(4)	0.389(2)
ILS 11	0.675(7)	0.241(2)	2.380(3)	0.441(8)	3.58(5)	2.733(16)	3.41(8)	1.148(6)	0.366(2)
ILS 12	0.820(8)	0.297(4)	2.379(3)	0.530(10)	4.48(7)	2.80(2)	3.55(10)	1.176(10)	0.358(3)
ILS 13	0.124(1)	0.045(1)	2.389(3)	0.079(2)	0.62(8)	2.448(11)	3.29(45)	1.025(5)	0.408(2)
ILS 14	0.840(8)	0.346(0)	2.385(3)	0.494(8)	4.03(4)	2.79(2)	3.42(7)	1.169(7)	0.359(2)
ILS 15	1.457(15)	0.597(8)	2.378(3)	0.875(17)	9.67(17)	2.93(3)	4.65(15)	1.232(15)	0.341(4)
Bulk	0.000	0.000	2.380	0.000	0.00	2.380	3.7010	1.000	0.4202
Long	0.000	0.000	2.380	0.000	0.00	2.380	4.4436	1.000	0.4202

Dry limestone:

				Hugoniot Conditions					
				Particle			Shock		Specific
Shot #	Proj. Velocity km/sec	Observed Vel. km/sec	ρ_0 gm/cm^3	Vel km/sec	Pressure GPa	ρ gm/cm^3	Vel. km/sec	ρ/ρ_0	Vol cm^3/gm
DLS 1	0.338(3)	0.087(5)	2.202(3)	0.251(6)	1.09(6)	2.52(3)	1.98(16)	1.145(16)	0.396(6)
DLS 3	0.868(9)	0.270(12)	2.193(3)	0.598(15)	3.19(14)	2.91(8)	2.44(16)	1.325(35)	0.344(9)
DLS 5	1.116(11)	0.401(4)	2.214(3)	0.715(12)	4.63(7)	2.93(4)	2.93(7)	1.323(17)	0.341(4)
DLS 6	2.042(20)	0.749(3)	2.202(3)	1.29(2)	12.19(18)	3.15(5)	4.28(9)	1.433(23)	0.317(5)
DLS 7	1.586(16)	0.552(4)	2.212(3)	1.034(16)	8.60(14)	3.05(4)	3.76(9)	1.379(20)	0.328(5)
DLS 8	1.308(13)	0.503(12)	2.213(2)	0.805(18)	5.76(15)	2.95(6)	3.23(14)	1.332(27)	0.339(7)

Notes:

Uncertainties in the last 1-2 digits presented are shown in parentheses.
Values are calculated assuming no precursors
Bulk and longitudinal ultrasonic velocities ("Bulk" and "Long") are for water-saturated limestone.

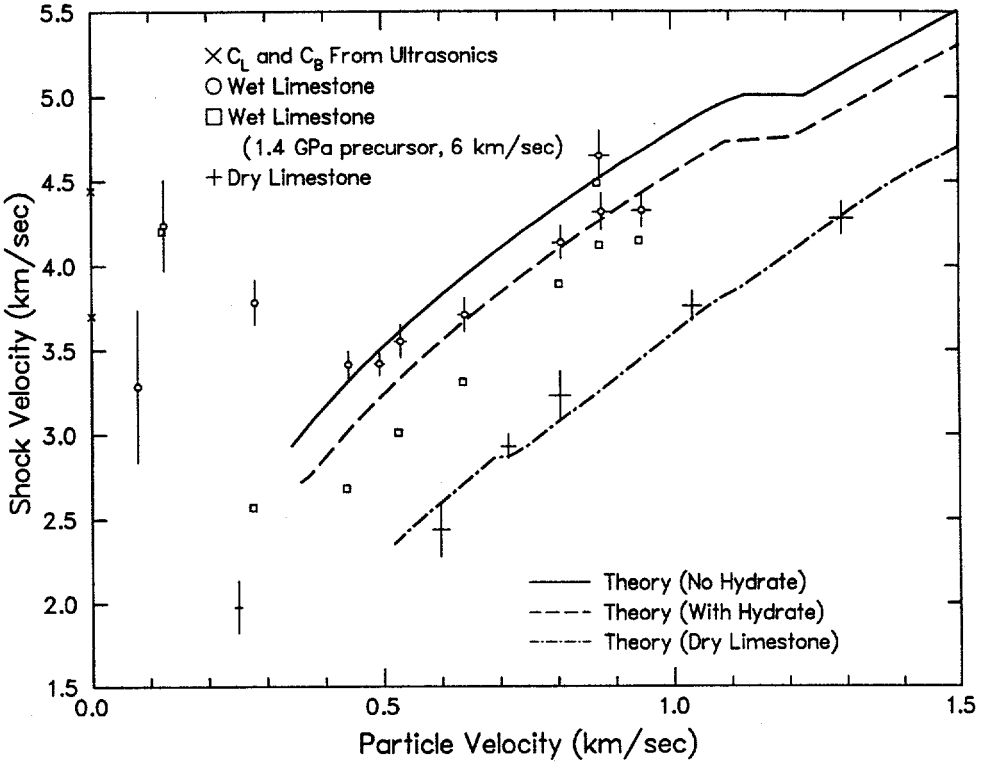

Figure 3-9. Shock velocity - particle velocity plot of Indiana limestone Hugoniot points, juxtaposed on theoretical curves from Kerley [1990].

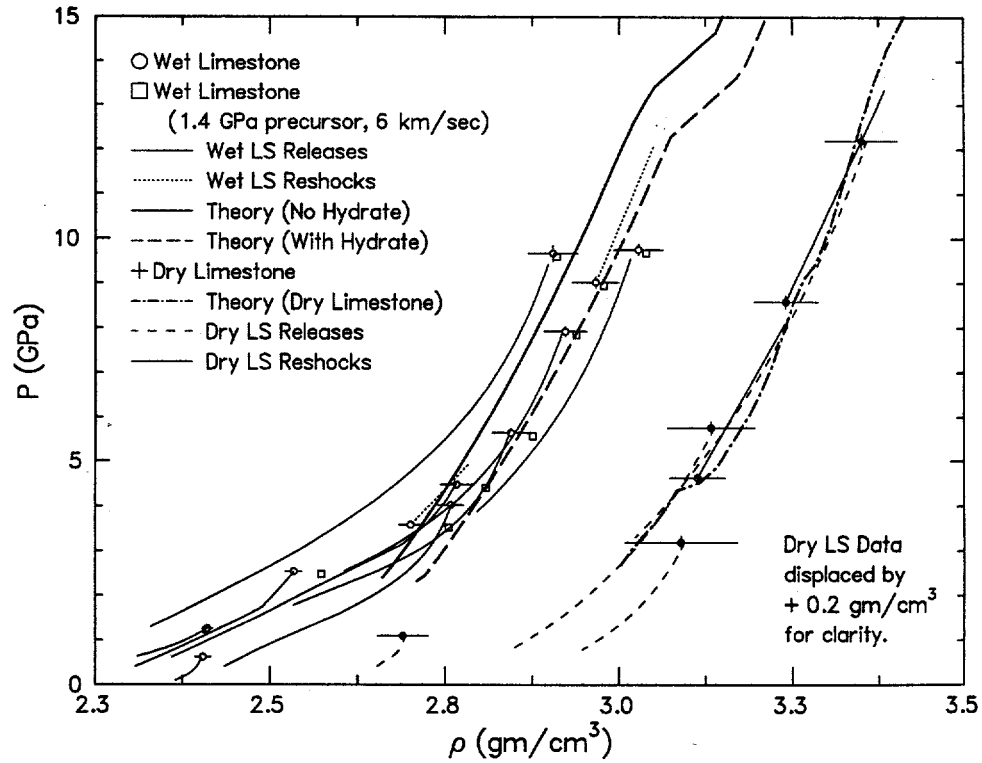

Figure 3-10. Stress - density plot of Indiana limestone Hugoniot points and release paths, juxtaposed on theoretical curves from Kerley [1990].

ity (Fig. 3-9) extrapolates to the ultrasonic measurement of the longitudinal velocity for zero particle velocity, suggesting an increasing role of strength for stresses below about 4 GPa. Recall, however, that the transmitted-wave tests did not show an explicit precursor. A possible explanation is that the role of elastic processes in the single shock increases with decreasing stress.

Reverse-ballistic tests - Release paths (curve fitting)

These reverse-ballistic release tests have been modeled with the wavecode WONDY V [Kipp and Lawrence, 1982] and parameters varied to extract information about the release behavior of this material. Details of the method and uncertainties are discussed in detail in Furnish [1993a, b]; I reproduce the critical equation here for reference:

$$(-V_0)\left.\frac{\partial \sigma}{\partial V}\right|_S \equiv B_S = B_0\left(1 + \chi B_1 + \chi^2 B_2 + \chi^3 B_3\right) \qquad \text{(where } \chi \equiv \frac{\sigma}{\sigma_H} - 1\text{)} \quad \text{(Eq. 3.3).}$$

The resulting modelings of the wave profiles are shown in Figs. 3-11 through 3-14. The coefficients used in Eq. 3.3 are listed, with other test parameters taken as listed in Tables 3.2 and 3.3. Note that two tests required two-part release fits (ILS10 and ILS12); release parameters for these are as listed in Table 3.6.

Table 3.6. WONDY Input Parameters - Two-Part Releases

	Above stress σ_{tran}				Below stress σ_{tran}					
Test #	B_0 GPa	B_1	B_2	B_3	B_0 GPa	B_1	B_2	B_3	σ_H GPa	σ_{tran}/σ_H*
ILS10	57	1.05	1.0	0.4	32	1.1	1.0	0.5	2.536	0.69
ILS12	97	3.0	3.0	0.0	26.5	0.2	0.2	0.5	4.484	0.7

*σ_{tran}/σ_H is the fraction of the Hugoniot stress σ_H at which the transition occurs.

Associated release results are summarized in Figure 3.10 (pressure-density plot) and in Appendix A (table).

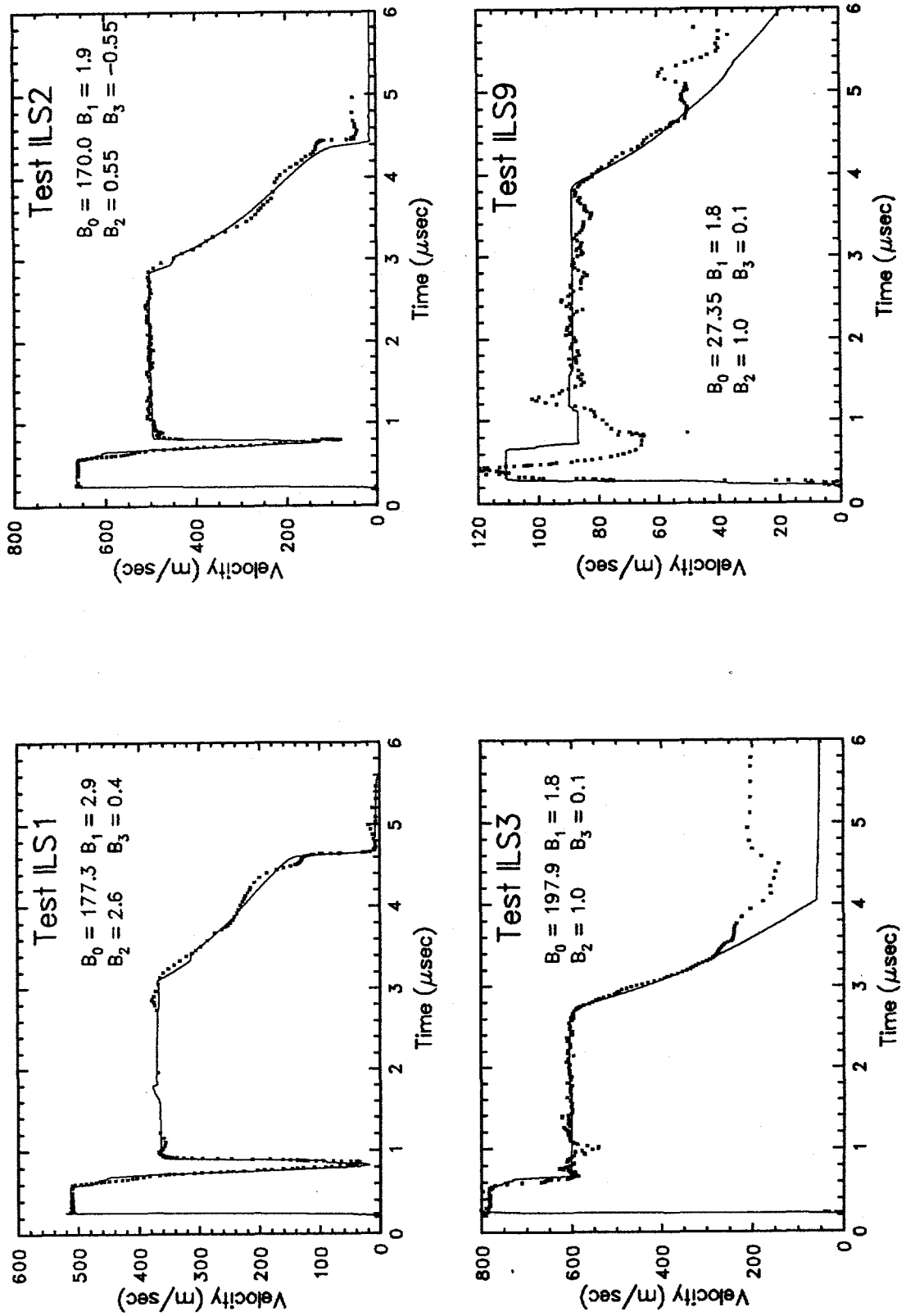

Figure 3-11. WONDY curve matches for saturated Indiana limestone release tests ILS 1, 2, 3 and 9.

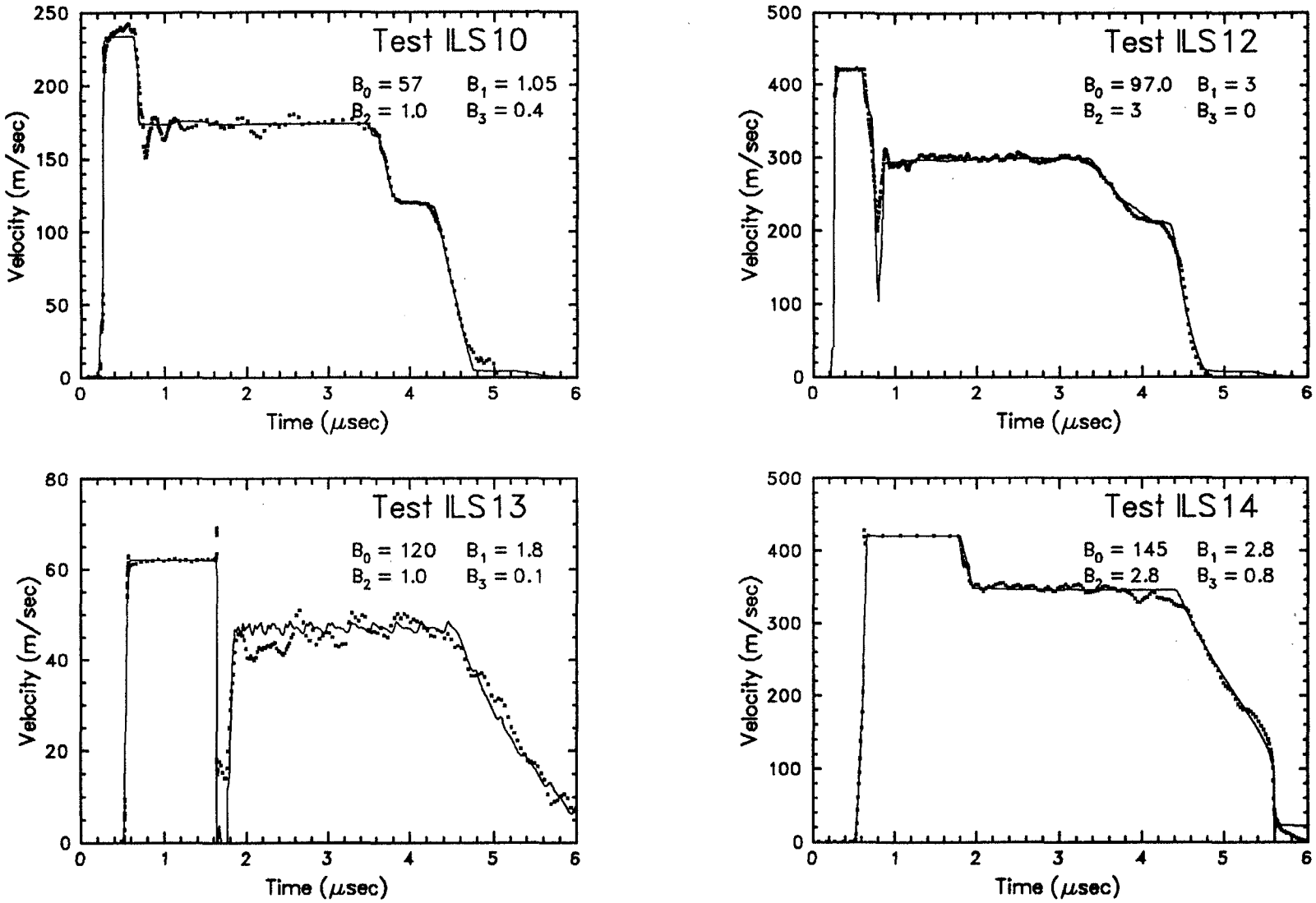

Figure 3-12. WONDY curve matches for saturated Indiana limestone release tests ILS 10, 12, 13 and 14.

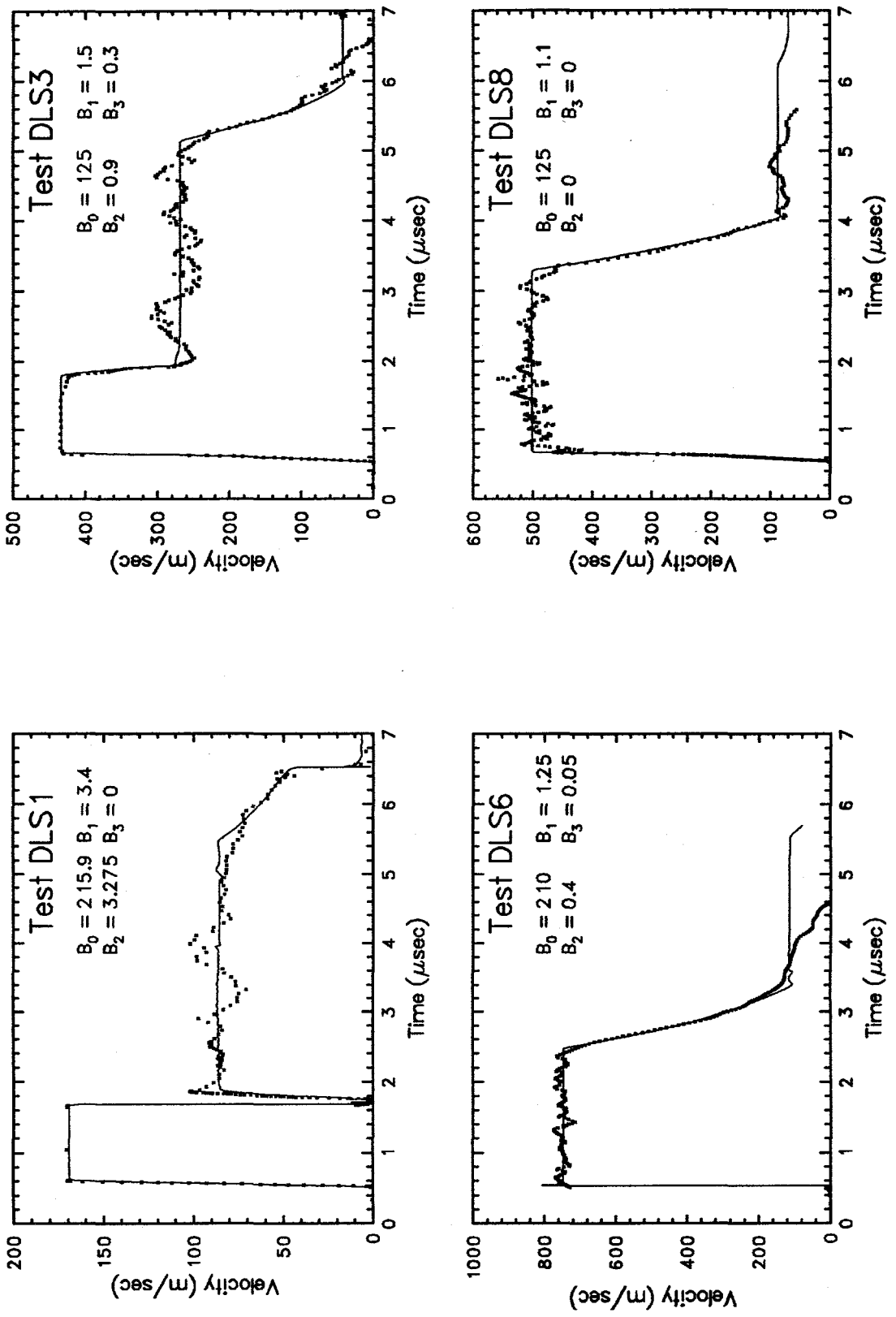

Figure 3-13. WONDY curve matches for dry Indiana limestone release tests DLS 1, 3, 6 and 8.

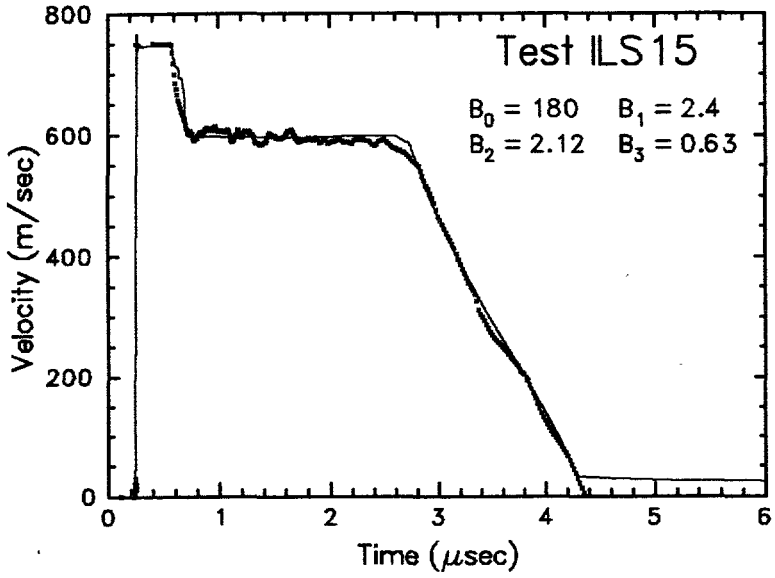

Figure 3-14. WONDY curve match for saturated Indiana limestone release test ILS 15

In general, the release curves lie close to the Hugoniots and share the same concave-upward nature (stress-density or stress-volume spaces). The two tests which required two-part release fits (ILS10 and ILS12) show a more pronounced initial sharp release.

Reverse Ballistic Tests - Reshock Paths (Impedance Match Analysis)

Four of the reverse-ballistic tests were designed with aluminum disks behind the samples in place of foam. For these tests, a significant reshock was produced and propagated forward to the interface monitored by VISAR. This reshock was manifested in the wave profile as a jump in the interface velocity (see Fig. 3-5). It is worthwhile to evaluate the stress, particle velocity and density in the reshocked state

Consider the stress vs. particle-velocity diagram in Figure 3-15. The Eulerian velocity of the reshock is given by the steady-wave equations [McQueen et al., 1970] as:

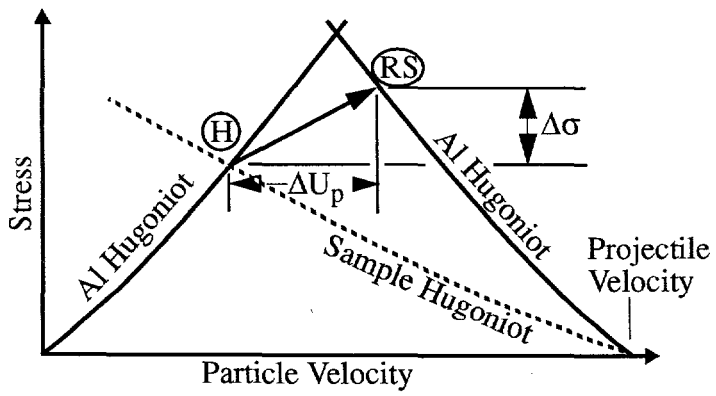

Figure 3-15. Impedance-match diagram for reverse-ballistic configuration (Al buffer, cup) illustrating reshock state calculation.

(H) = Hugoniot state

(RS)= Reshock state

$$U_{S(Eul)} = V_H\sqrt{-\frac{\Delta P}{\Delta V}} \qquad \text{(Eq. 3.4)}$$

(where V_H is the Hugoniot specific volume). Combining this with a second steady-wave equation,

$$\Delta U_P = \sqrt{\frac{-\Delta P}{\Delta V}} \qquad \text{(Eq. 3.5)}$$

and eliminating ΔV gives the slope of the reshock in stress/particle velocity space. The

$$\left|\frac{\Delta P}{\Delta U_P}\right| = U_{S(Eul)}/V_H \qquad \text{(Eq. 3.6)}$$

reshock vector is then drawn from the Hugoniot point until it crosses the Hugoniot of the sample backing material (see Fig. 3-15), establishing the stress and particle velocity of the reshocked material. We then return to either of the two earlier equations to calculate the change in specific volume from the Hugoniot state to the reshocked state,

$$\Delta V = -\frac{(\Delta U_P)^2}{\Delta P} \qquad \text{(Eq. 3.7)}$$

The Eulerian velocity of this reshock, $U_{S(Eul)}$ may be calculated as follows:

(1) Calculate the time at which the initial shock entered the sample, taking into account sample/cup gap widths where appropriate. For tests without cups, this time is zero.

(2) Calculate the time at which the reshock was generated from the sample dimensions and Hugoniot.

(3) Calculate the time at which the reshock entered the cup or buffer from the observed arrival time in the wave profile and the shock/release properties of the cup and buffer.

(4) Calculate the reshock transit time across the compressed sample as the difference of the results of (2) and (3).

(5) Divide the compressed thickness of the sample by the results of (4).

The results of this analysis are shown in Table 3.7 and Figure 3-10 (stress-density space). In general, these reshocks are directed nearly up the Hugoniot, consistent with a minimal role of thermal effects and of strength. The lowest-pressure reshock test (ILS11) showed a reshock arrival earlier than reshocking along the Hugoniot would suggest; this is reflected in the steeper reshock drawn in pressure/density space (Fig. 3-10). Also of note, the reshock arrival for ILS11 is much more dispersed than for the other tests. For these two reasons, I feel that sample strength may play a significant role in this test.

Table 3.7. Reshock states and input parameters for Indiana Limestone tests

Test #	Reshock Time-of-Arrival (μsec)	Reshock Velocity (km/sec)	← Reshocked State → Stress (GPa)	Particle Vel*. (km/sec)	Specific Vol. (cm^3/gm)	Density (gm/cm^3)
ILS 5	2.82	6.272	12.12	0.712	0.326	3.069
ILS 11	4.00	4.188	4.97	0.355	0.355	2.815
DLS 5	4.75	5.451	8.09	0.617	0.328	3.049
DLS 7	2.80	6.004	13.34	0.811	0.314	3.188

*Particle velocity corrected to that of analogous transmitted-wave experiment (see text).

3.3.3 Release structure association with a calcite multiphase model

It is worthwhile to briefly ask whether the release structure shown in Fig. 3-1 (reverse-ballistic tests) is likely due to strength or phase changes. The previous analyses have treated it phenomenologically by, for example, assigning separate release behavior to the upper and lower sections of the release in WONDY analyses of ILS 10 and ILS 12.

Material strength typically gives rise to a somewhat blurred shoulder at the beginning of the release in wave profiles from reverse-ballistic experiments. The decrease in particle velocity across this shoulder may be combined with the Hugoniot state to estimate the material strength, while the onset of the release provides information about the elastic wave velocity at the Hugoniot.

On the other hand, phase transitions occurring during the release tend to provide a step-type structure at interface velocities not closely related to the Hugoniot levels. This structure is slightly complicated by transitions which may occur during the initial sample loading (which may cause the loading wave to break into several waves, which reflect from the rear of the sample at separate times). It is likely in the porous samples used in the present study that the wave splitting would be minimized, as discussed earlier.

Since the structure observed on the release portion of the velocity profiles is more consistent with the signatures of phase transitions, I prepared a modeling of two reverse-ballistic tests using fully dense calcite as the starting material and assuming a pressure/density relation based on the compression curves measured by Singh and Kennedy [1974]. These compression curves clearly demark the $CaCO_3$ I, II and III phases. Although these simulations do not precisely represent the 18% porous samples used, they serve to give an indication of the structure the $CaCO_3$ I ↔ (II) ↔ III transitions would give to the observed wave profiles.

Figure 3-16 shows the models used and the WONDY V representation of them (constructed to replace the $CaCO_3$ II phase with a ramp from $CaCO_3$ I to $CaCO_3$ III for simplicity). The resulting model wave profiles for tests at 700 m/sec and 1297 m/sec (Fig. 3-16) show a step pattern which in fact closely resembles that seen in the experimental data for saturated limestone (Figure 3-1). The wave evolution for the 700 m/sec experiment may be seen in Figure 3-17.

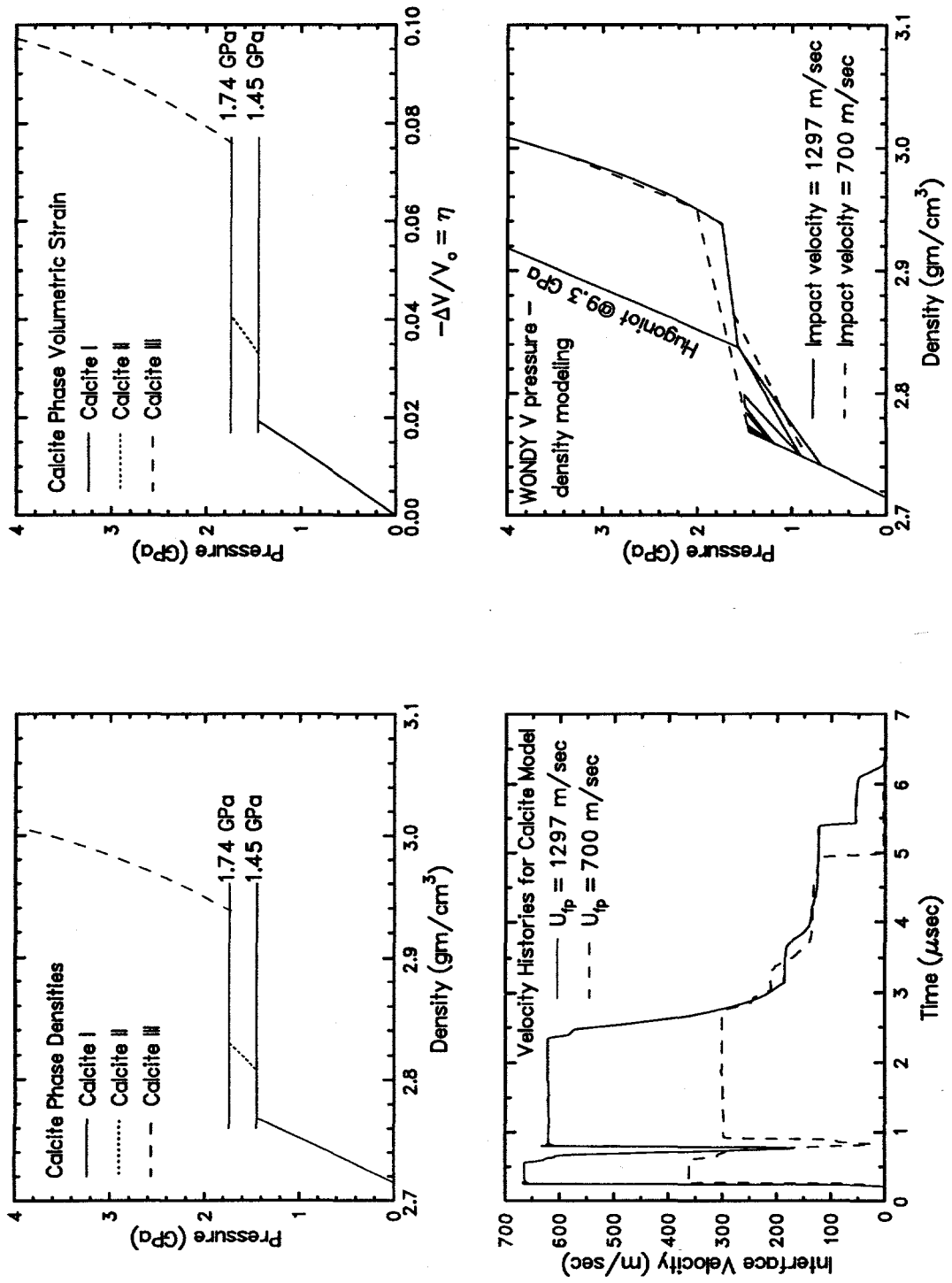

Figure 3-16. (Top) $CaCO_3$ I ↔ (II) ↔ III compression behavior [Singh and Kennedy, 1974]. (Lower left) Pressure/density paths traced in WONDY V simulation of this compression behavior. (Lower right) Resulting model wave profiles. See text for details.

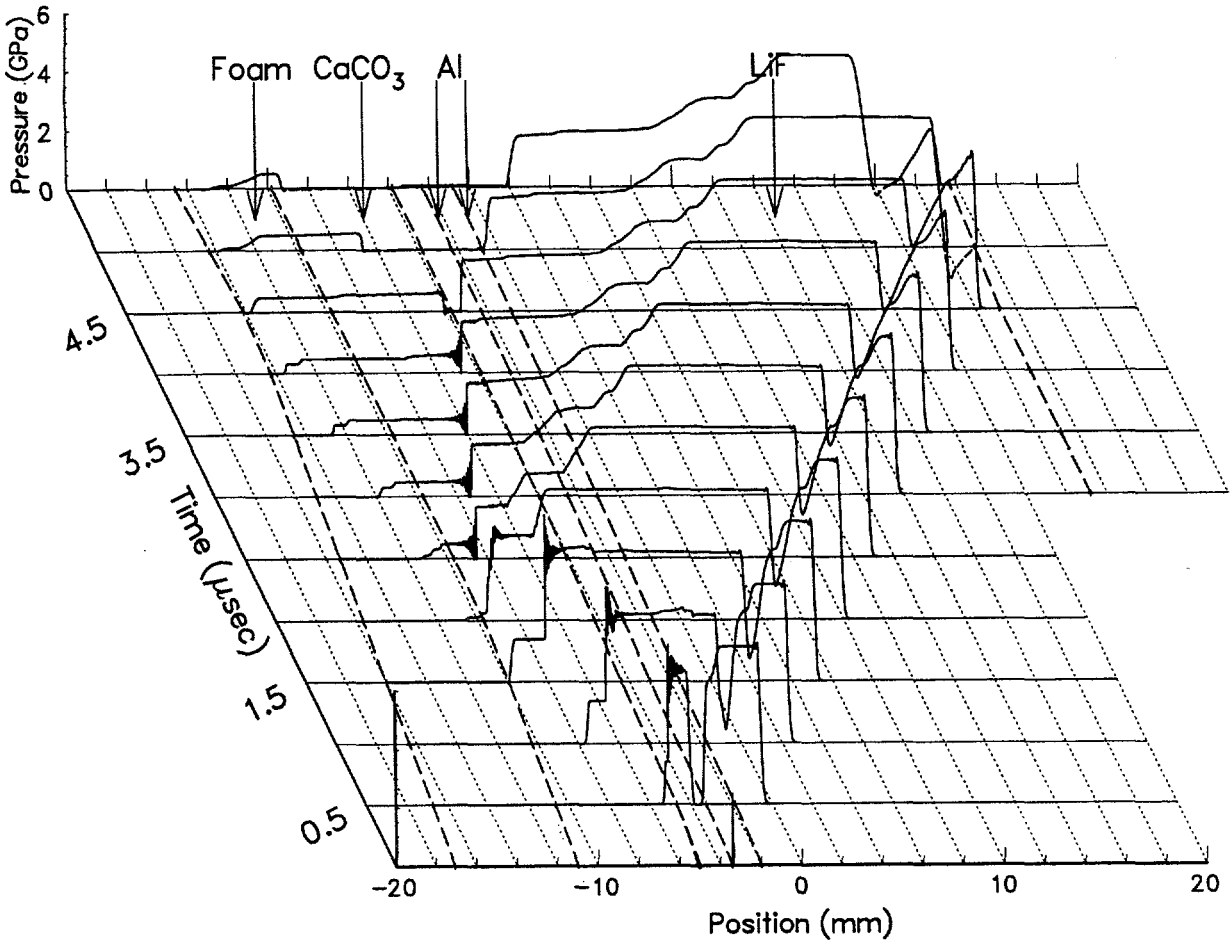

Figure 3-17. Wave evolution for 700 m/sec reverse-ballistic experiment, simulated with WONDY V to include $CaCO_3$ I ↔ (II) ↔ III transitions according to Singh and Kennedy [1974] compression curves.

Although the sample used in these modelings is different from the material tested, the modelings strongly suggest that the structure observed in the release portion of the wave profiles of Figure 3-1 is due to phase transitions in the $CaCO_3$ I ↔ (II) ↔ III system.

3.3.4 SESAME CTH Modeling: Wave structures associated with Crush-Up

As a brief evaluation of the effects of crush-up on the transmitted wave profiles, a transmitted-wave experiment performed on dry Indiana limestone (DLS9) was modeled using a calcite SESAME equation of state (see below for details). A reverse-ballistic release test on the same material was modeled as well (DLS6).

The important adjustable constitutive and equation-of-state parameters in these runs were the porosity (via the initial density `RO`), the initial sound speed of the porous material (`CS`), the initial crush pressure (`PT`), and the modulus of crushup (`BT`).

The CTH wavecode was used to allow use of the desired EOS (not available in WONDY V). These calculations were performed in one dimension to optimize zone resolution available within workstation calculation limits, although two- and three-dimensional calculations can also be performed with the CTH software. One thousand zones were used (0.07 mm/zone). The code is Eulerian; hence zone size remained constant in the laboratory frame through the calculation.

Results of this calculation are shown in Figure 3-18. It should be noted that the timing of the wave profile in test DLS9 is translated to fit the results of the present calculation. DLS9 is the only test in this report for which timing relative to impact was not established from the experimental data. This diminishes the material property information available from this test somewhat.

For test DLS9 (transmitted-wave experiment producing a maximum stress level estimated as 1.2 GPa), the parameters governing the uncrushed material and the crush-up process have a marked effect on the calculated wave profile. The predictions for this shot were obtained by using the SNL-SESAME two-state porosity-phase transition model described by Kerley [1992], with the following parameters (all of which are in cgs units):

```
TYP = 1.2    R0 = 2.2    CS = 2.0e5    s = 1.0    G0 = 1.0

PT = 0.15E10    BT = 2.5E10
```

The parameters `CS`, `PT`, and `BT` were selected to be in agreement with the static data of Heard [1974]. The resulting model wave profile is in reasonable agreement with the observed wave profile to about 7 μsec after impact, after which two-dimensional effects may become important.

By contrast, model profiles for test DLS6 (reverse-ballistic test producing stress levels of 12 GPa) are relatively insensitive to details of parameters governing the uncrushed material and the crush-up process. The same model used above gives good agreement with the experimental data for DLS6.

3.4 Summary

A relatively pure, fine-grained limestone of about 18% porosity was tested in water-saturated and desiccated conditions. Hugoniot stresses produced ranged from 0.6 GPa to 12 GPa. A comparison of the Hugoniot results for the saturated material suggests that a hydration reaction to produce ikaite ($CaCO_3 \cdot 6H_2O$) occurs on a shock timescale (< 1 μsec).

Wave profiles provided loading, release and reshock information. Release paths tend to lie along the Hugoniot, showing little hysteresis. Reshock results are similar except at stresses below 4 GPa, where strength effects become significant. Strength effects are also significant in the shock velocity of the Hugoniot state at stresses less than 4 GPa. Structure observed on the releases is tentatively attributed to phase transitions in the $CaCO_3$ I ↔ (II) ↔ III system. Finally, transmitted-wave experiments did not show evidence for phase-transition related precursors.

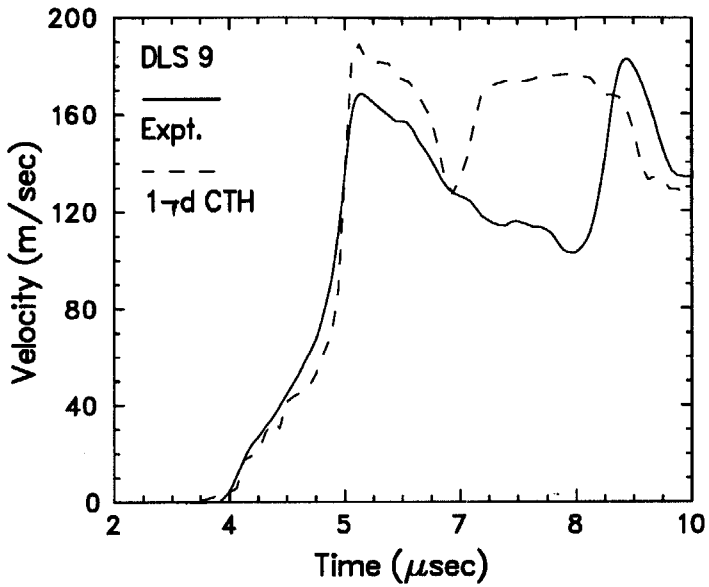

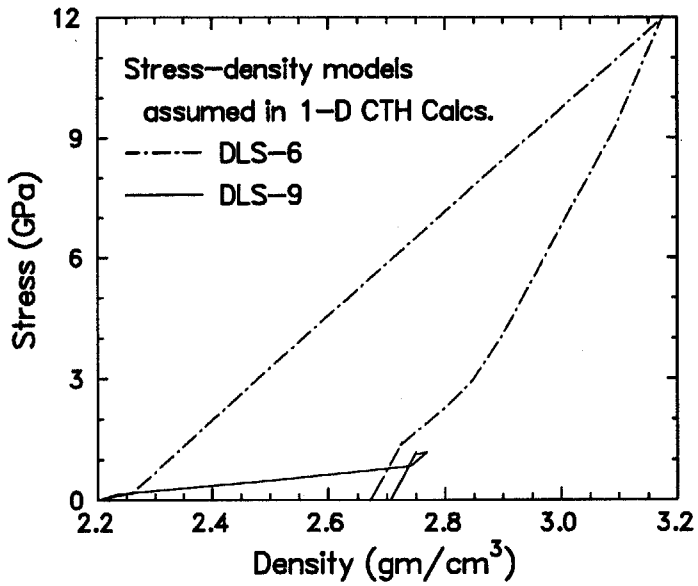

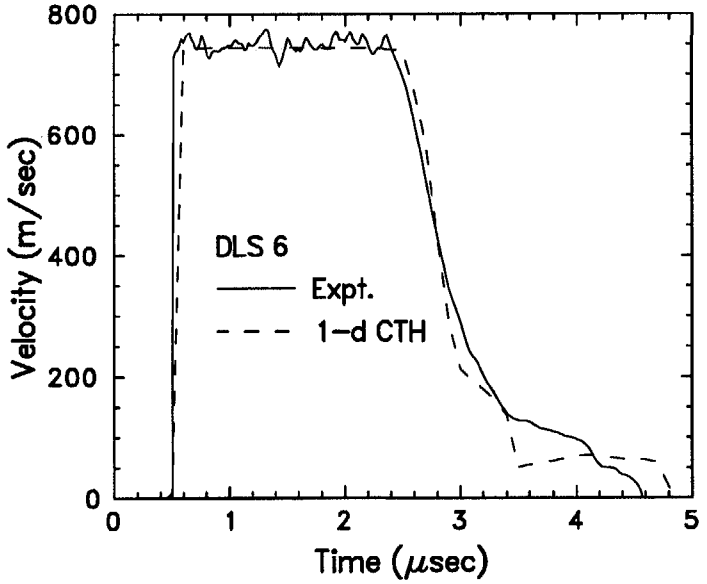

Figure 3-18. SESAME model profiles and stress-density histories for dry limestone. (Upper left) Test DLS9, max. stress ~1.25 GPa, transmitted wave. (Lower left) Test DLS6, maximum stress ~12.5 GPa, reverse-ballistic. (Upper right) Stress-strain paths corresponding to wave profiles shown at left.

4.0 Jeffersonville and Louisville Limestones

4.1 Motivation for study

The studies described on the present samples were conducted to address the question of how strongly the shock responses of frozen and thawed carbonate samples differed. The major goal of the DNA HYDROPLUS program, which funded this study, was to measure the yields of underground tests from measurements of particle velocities and stresses at various radii from the working point. Converting these measurements to yield determinations requires some knowledge of the dynamic properties of the local rockmasses.

In order to produce such dynamical properties data, samples of the local rockmass must be acquired, transported to a facility where they are machined as needed for testing, machined, transported to the testing facility, and tested (impact or explosives tests). If an underground test is conducted in frozen terrain, the frozen samples may be handled in any of three ways:

(1) The samples may be cored without melting, and conducted through all subsequent stages of preparation, transportation and shock testing without being allowed to melt,

(2) The samples may be allowed to thaw at some point in the process, then refrozen immediately or shortly before testing, or

(3) The samples may be allowed to thaw at some point in the process, and tested in the thawed condition.

The cost and difficulty of each stage in this process is increased substantially if a frozen state must be maintained. If the uncertainties in the end yield measurement introduced by allowing the samples to thaw are small, then the third alternative above is preferable, followed by the second, with the first being the most difficult and expensive.

The present study includes comparable impact tests on frozen and room-temperature dolomitized limestones from the Fort Knox, Kentucky area. It is relatable to a parallel study conducted simultaneously by Ktech Corp [Gaffney and Smith, 1994].

A later impact study conducted on quartzite permafrost recovered from the Lupin Mine (Canada) included samples in three states (preserved-frozen, thawed-and-refrozen and thawed). This study is described in Furnish [1993a].

4.2 Materials studied

The samples used in the present study were acquired in nearly water-saturated condition from the UTP (Underground Test Program) site at Fort Knox, Kentucky. Two formations are represented; materials acquired from these are referred to here as the Louisville and Jeffersonville limestones. In general, the Louisville limestone is more variable and more dolomitized (substitution of Mg for Ca) than the Jeffersonville. Both formations have very

low porosity ($\phi \lesssim 0.5\%$).

The Louisville limestone samples were acquired from bore CB-7 at depths of 601.2 - 602.3 feet (samples 2, 5, and 8) and 642.3 - 642.9 feet (samples 9 and 14). Cores in these intervals were divided into samples so that samples provided to Sandia, Ktech and retained by Waterways were interleaved. The Jeffersonville limestone samples were obtained from the depth interval 523.2 - 523.45 feet (samples for Ktech were taken from the adjacent interval 523.6 - 523.9 feet).

All samples were encased in plastic wrap, aluminum foil and 50/50 paraffin/microcrystalline wax ("artificial beeswax") in the field to minimize moisture loss. The Louisville limestone samples were prepared for impact testing at Waterways Experiment Station [Jackson, personal communication] by slicing, then hand grinding, while immersed in tap water (Vicksburg, MS). The Jeffersonville limestone samples were prepared by Terra Tek using diamond saws and industrial surface grinding equipment, preserving saturation through a continuous flow of cooling water over the samples.

4.3 Experiments conducted

The overall matrix of tests (including tests conducted at Ktech) is indicated in Table 4.1. The Ktech tests will not be discussed in detail in the present report; the reader is referred to Gaffney and Smith [1994]. This matrix was constructed to afford comparisons among (1) frozen and thawed samples; (2) Louisville and Jeffersonville samples; and (3) Sandia and Ktech tests.

Table 4.1. Overall impact test matrix (including non-Sandia tests) on Louisville and Jeffersonville limestones.[1]

Pressure (kbar)	Frozen Tests			Warm Tests			Gun, Velocity (SNL tests only)
15		K(L)			K(L)		
25	$S(J)_6$	K(L)	K(L)	$S(J)_1$	$S(J)_2$	K(J)	Gas; 0.57
35		K(L)			K(L)		
50	$S(L)_7$	$S(J)_8$	K(L)	$S(L)_3$	K(L)	K(J)	Powder; 1.02
80		$S(J)_{10}$			$S(J)_4$		Powder; 1.60
140		$S(L)_9$			$S(L)_5$		Powder; 2.25

1. K = Ktech; S = Sandia; (J) = Jeffersonville Limestone; (L) = Louisville Limestone; boldface = completed. Subscripts represent shot number (PF*n*) for Sandia tests (e.g. $S(L)_7$ is test PF7, as detailed in Table 4.2). Test PF2 is reverse-ballistics.

The Sandia test matrix is presented in detail in Table 4.2. All of the tests were conducted in a transmitted-wave configuration (Figure 2-1) except for test PF-2, which was conducted in a reverse-ballistic configuration (Figure 2-2).

Table 4.2. Test matrix of Sandia tests on Louisville and Jeffersonville Limestones

Reverse Ballistic

Shot #	Gun Facility	Impact Velocity (km/sec)	Foam Density (gm/cm^3)	Foam Thick (mm)	Sample ID	Sample Density (gm/cm^3)	Sample Thick (mm)	Al Cup Thick (mm)	Buffer Material[1]	Buffer Thick (mm)	Window[2] Thick (mm)	Velocity[3] Per Fringe (km/sec)
PF2	Gas	0.597	0.296	4.981	Jeff (25°C)	2.722	5.0088	2.0024	Al	1.462	25.533	0.055995

Forward Ballistic

Shot #	Gun Facility	Impact Velocity (km/sec)	Flyer Plate Thick[4] (mm)	Cup Thick (mm)	Sample ID[5]	Sample Density (gm/cm^3)	Sample Thick (mm)			Buffer[6] Thick (mm)	Window[6] Thick (mm)	Velocity Per Fringe (km/sec)
PF1	Gas	0.670	12.665	2.0265	Jeff (25°C)	2.738	8.016			3.183	25.808	0.07240
PF3	Powder	1.008	12.622	2.046	Louis (25°C)	2.768	8.000			3.136	25.656	0.16399
PF4	Powder	1.540	12.658	2.009	Jeff (25°C)	2.725	8.025			3.102	25.628	0.25286
PF5	Powder	2.230	12.648	2.051	Louis (25°C)	2.771	8.015			3.124	25.632	0.34626
PF6	Gas	0.636	12.672	2.0275	Jeff (-10°C)	2.714	8.025			3.203	25.537	0.07240
PF7	Powder	1.056	12.667	2.025	Louis(-10°C)	2.786	8.009			2.974	25.798	0.16399
PF8	Powder	1.026	12.667	2.035	Jeff(-10°C)	2.722	8.017			3.014	25.55	0.16399
PF9	Powder	2.250	12.628	2.058	Louis(-10°C)	2.777	8.008			3.021	25.621	0.34626
PF10	Powder	1.539	12.590	2.054	Jeff(-10°C)	2.707	8.017			3.084	25.687	0.25286

Notes:

[1]Standard aluminum used is 6061-T6 throughout assembly.

[2]Window is composed of lithium fluoride for reverse-ballistic test in this study.

[3]Velocity per fringe (VPF) corresponds to a setting of the VISAR.

[4]In these forward-ballistic tests, the flyer plate is backed by a void (gas gun) and a void with a phenolic support tube (31.75mm ID, 44.45 mm OD) (powder gun).

[5]Jeff = Jeffersonville Limestone; Louis = Louisville Limestone.

[6]Buffer and window are composed of PMMA for forward-ballistic tests in this study.

The present experiments all began with thawed samples held at ambient temperature (approx. 25°C). For the five tests conducted on frozen samples, target fixtures used were constructed as shown in Figure 5-1. Gaseous nitrogen evolved from liquid nitrogen was circulated through the target plate to cool the sample, with thermocouples emplaced to monitor the temperature. Because of the very low moisture content of the samples, they were found to thermally equilibrate with the target at -10°C after a short time (several minutes) of cooling.

All samples (refrigerated and ambient) were protected from moisture loss during storage, assembly into the test assemblies and impact testing.

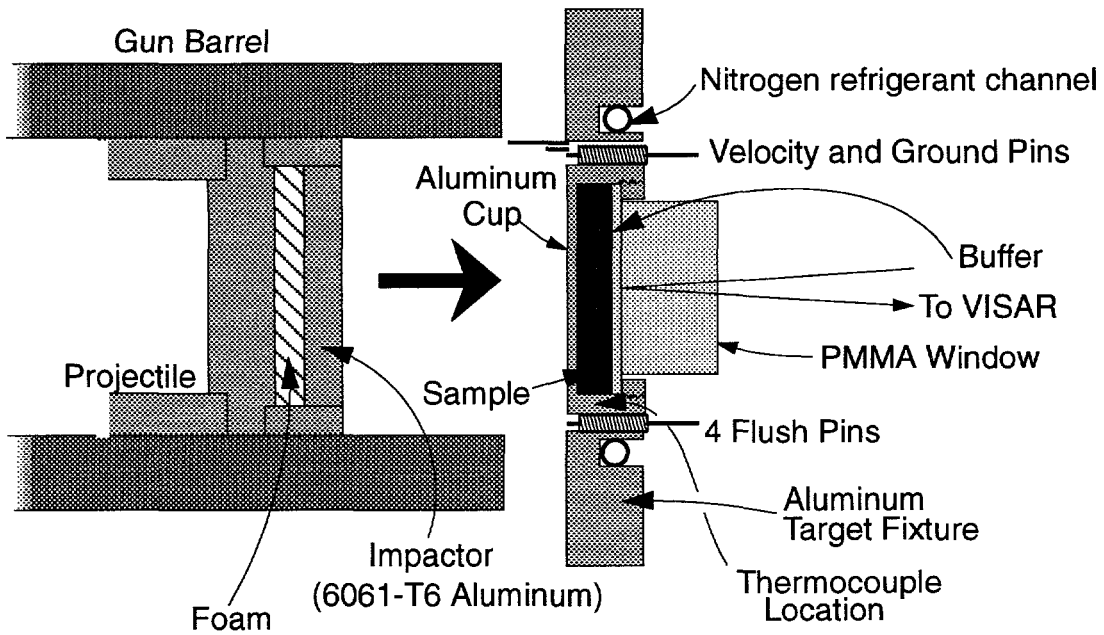

Figure 4-1. Schematic of the refrigerated target configuration used in the Fort Knox limestone tests.

4.4 Dynamic properties results

4.4.1 Velocity profiles observed

The velocity profiles observed for the eight transmitted-wave experiments are shown in Figure 4-2. The timebases have been shifted (shot-by-shot) so that zero represents the time of impact. Details of this procedure are presented in Appendix B.

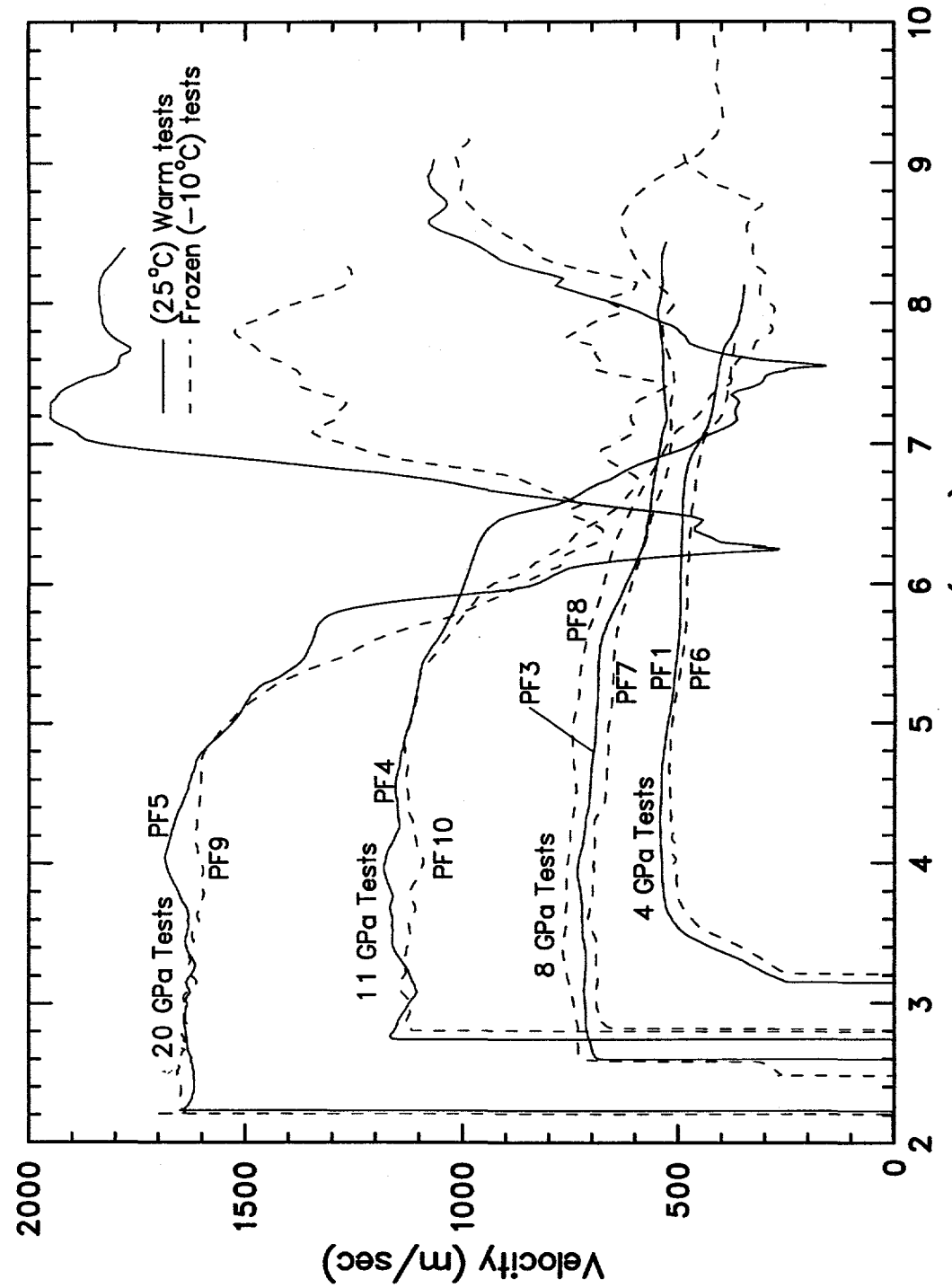

Figure 4-2. Velocity profiles measured for transmitted-wave impact experiments on Fort Knox limestones: Jeffersonville (PF1, 4, 6, 8, and 10) and Louisville (PF3, 5, 7, and 9). See Table 4.2 for experimental parameters.

All waveforms display a loading interval, a plateau (height corresponding to the impedance match relationships depicted in Figure 3-7), and a release propagated forward from the impactor/foam boundary in the projectile.

The less dolomitized samples (Jeffersonville Limestone, used in tests 1, 4, 6, 8 and 10) showed precursors for Hugoniot stresses below 11 GPa, while the more dolomitized samples (Louisville Limestone, used in the remaining transmitted-wave tests) did not show precursors. This is consistent with observations by Grady et al [1976a] that the precursors in dolomite-rich carbonates are less pronounced than those in calcite-rich carbonates if they are present at all.

4.4.2 Precursor, Hugoniot and partial release conditions

Derivation of these states has been discussed previously (Section 3.3.2; Furnish [1993a,b]), and will not be belabored here. This process is summarized graphically in Figure 4-3. Results for the present materials are presented in Table 4.3.

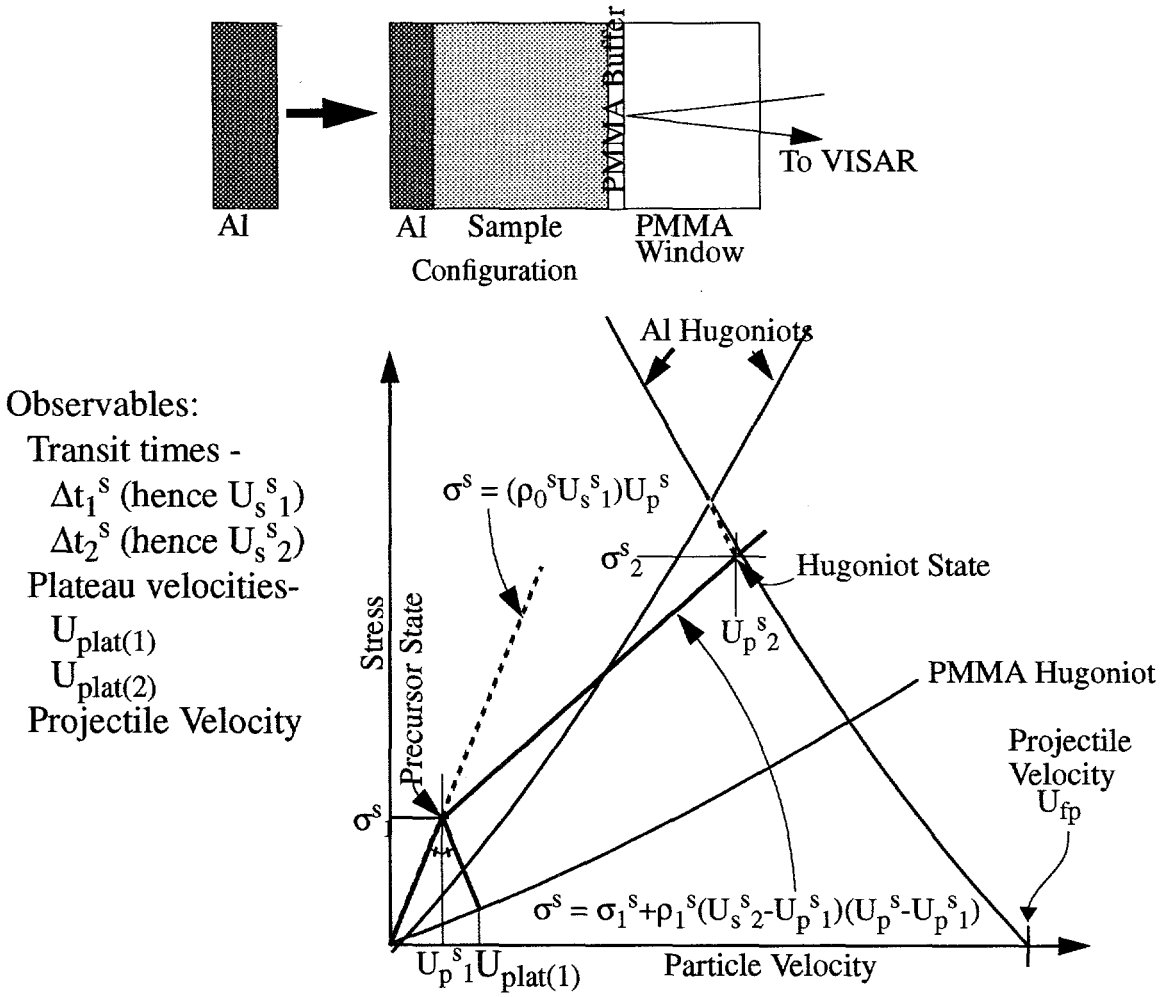

Figure 4-3. Calculation of Shock States, Forward-Ballistic, 2-Wave Case. $U_s^s{}_2$ is referenced to compressed medium (is Lagrangian). Superscript S refers to "sample." Subscripts 1 and 2 refer to first and second shocked states. "U_{Plat}" refers to plateau velocity.

Table 4.3. Precursor and Hugoniot values from transmitted-wave experiments on Jeffersonville and Louisville (Fort Knox) limestones.

				Precursor/Hugoniot Conditions					
Shot #	Proj. Velocity km/sec	Plastic TOA μsec	ρ_0 gm/cm^3	Particle Vel km/sec	Pressure GPa	ρ gm/cm^3	Shock Vel. km/sec	ρ/ρ_0	Specific Vol cm^3/gm
PF 1	0.670(7)	3.307(8)	2.738						
	Precursor Conditions →			0.17(7)	2.3(9)	2.84(5)	4.88(19)	1.036(17)	0.352(6)
	Hugoniot Conditions →			0.379(9)	4.33(10)	3.02(1)	3.62(14)	1.103(4)	0.331(1)
PF 3	1.008(10)	0.719(7)	2.768						
	Precursor Conditions →			0.00(0)	0.0(0)	2.768(0)	0.00(0)	1.000(0)	0.3613(0)
	Hugoniot Conditions →			0.511(5)	8.03(9)	3.041(5)	5.68(3)	1.099(2)	0.3288(6)
PF 4	1.540(15)	2.752(30)	2.725						
	Precursor Conditions →			0.00(0)	0.0(0)	2.725(0)	0.00(0)	1.000(0)	0.3670(0)
	Hugoniot Conditions →			0.865(17)	11.0(2)	3.35(2)	4.65(9)	1.229(9)	0.299(2)
PF 5	2.230(22)	2.242(9)	2.771						
	Precursor Conditions →			0.00(0)	0.0(0)	2.771(0)	0.00(0)	1.000(0)	0.3609(0)
	Hugoniot Conditions →			1.158(13)	19.4(2)	3.426(12)	6.06(4)	1.236(4)	0.2919(11)
PF 6	0.636(6)	3.397(9)	2.714						
	Precursor Conditions →			0.17(7)	2.2(9)	2.82(5)	4.74(18)	1.038(18)	0.355(6)
	Hugoniot Conditions →			0.364(9)	4.02(10)	2.988(13)	3.50(13)	1.101(5)	0.335(2)
PF 7	1.056(10)	2.822(15)	2.786						
	Precursor Conditions →			0.00(0)	0.0(0)	2.786(0)	0.00(0)	1.000(0)	0.3589(0)
	Hugoniot Conditions →			0.572(7)	7.65(12)	3.162(9)	4.80(4)	1.135(3)	0.3163(9)
PF 8	1.026(10)	2.602(11)	2.722						
	Precursor Conditions →			0.15(2)	3.0(3)	2.782(8)	7.16(12)	1.022(3)	0.3590(10)
	Hugoniot Conditions →			0.525(6)	8.09(9)	3.008(6)	5.08(6)	1.105(2)	0.3324(6)
PF 9	2.250(23)	2.217(5)	2.777						
	Precursor Conditions →			0.00(0)	0.0(0)	2.777(0)	0.00(0)	1.000(0)	0.3601(0)
	Hugoniot Conditions →			1.168(14)	19.6(2)	3.441(12)	6.05(2)	1.239(4)	0.2906(10)
PF 10	1.539(16)	2.802(7)	2.707						
	Precursor Conditions →			0.00(0)	0.0(0)	2.707(0)	0.00(0)	1.000(0)	0.3694(0)
	Hugoniot Conditions →			0.873(18)	10.8(2)	3.350(16)	4.55(2)	1.237(6)	0.2985(15)

	Partial Release Conditions			
Shot #	Plateau Velocity km/sec	Stress GPa	Particle Vel. km/sec	Release Slope GPa/(km/sec)
PF 1	0.540(6)	2.48(15)	0.540(6)	11.5(1.3)
PF 3	0.719(7)	3.13(6)	0.719(7)	23.6(1.4)
PF 4	1.17(6)	6.05(44)	1.170(60)	16.1(4.2)
PF 5	1.62(2)	9.70(23)	1.620(20)	21.0(1.7)
PF 6	0.508(14)	2.30(13)	0.508(14)	11.9(2.0)
PF 7	0.690(5)	2.97(5)	0.690(05)	13.0(0.9)
PF 8	0.732(2)	3.63(7)	0.732(02)	22.8(1.2)
PF 9	1.648(4)	9.95(16)	1.648(04)	20.2(1.2)
PF 10	1.127(12)	5.74(12)	1.127(12)	19.7(2.7)

Uncertainties in the Table 4.3 values were derived by perturbing the following quantities (quantities in parentheses were the state quantities most strongly affected by the respective perturbations). The resulting variations in state values were propagated in quadrature.

- Precursor amplitude ($\Rightarrow$ precursor state)
- Projectile velocity ($\Rightarrow$ Hugoniot P, ρ, U_P)
- Plastic plateau velocity ($\Rightarrow$ Hugoniot U_S, partial release P, U_P)
- Aluminum strength (varied from the nominal value of 3 kb with thermal softening to a perturbed value of zero strength) ($\Rightarrow$ Hugoniot P, ρ, U_P)
- Aluminum Hugoniot (increased stress at particle velocity by 1%) (little effect)
- PMMA Hugoniot (increased starting density by 1%, an extreme variation) ($\Rightarrow$ partial release P)

The density on the partial release cannot be determined directly from these experiments because a continuous stress/particle velocity curve from the Hugoniot point to a partially released state is not available (see Section 3.3.2). If a form for such a curve is estimated, densities may also be estimated.

The reverse-ballistic experiment was analyzed to give the values in Table 4.4 (waveform shown, together with WONDY match, in Figure 4-4). This analysis assumed a 1.4 GPa precursor (see discussion of Danby Marble test interpretation, Section 5, for details).

Table 4.4. Hugoniot conditions for reverse-ballistic test on Jeffersonville Limestone.

			Hugoniot Conditions						
				Particle			Shock		Specific
Shot #	Proj. Velocity km/sec	Observed Vel. km/sec	ρ_0 gm/cm^3	Vel km/sec	Pressure GPa	ρ gm/cm^3	Vel. km/sec	ρ/ρ_0	Vol cm^3/gm
PF 2	0.579(18)	0.278(2)	2.722(13)	0.306(17)	4.15(4)	2.90(3)	5.0(3)	1.165(12)	0.345(3)

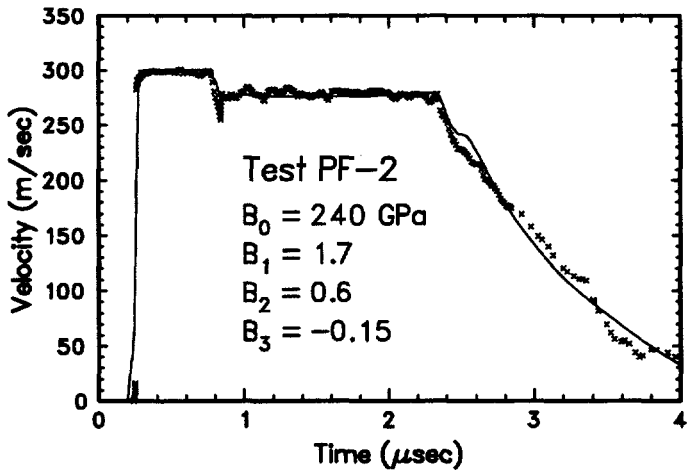

Figure 4-4. Wave profile for reverse-ballistic test PF-2 (Jeffersonville limestone). Shot parameters shown in Table 4.2. WONDY match also shown (solid line).

These Hugoniot data are plotted with results from Danby marble (Section 5) as Figures 4-5 through 4-8. The Danby marble is a nearly pure calcite marble. These figures also indicate a representative limestone Hugoniot, fit to data reported by Marsh [1980] for dry calcite limestone near theoretical density (2.687 - 2.703 gm/cm^3). This fit is described by C_0 = 3.7225 km/sec, S = 1.4788, and ρ_0 = 2.70. In most cases, the less dolomitized limestones and the Danby Marble lie fairly close to this fit.

Figure 4-6 (P vs. ρ) also shows the Singh and Kennedy [1974] compression curves for calcite to 4 GPa. Although detailed agreement of the present results with these curves is spotty (principally in the variability of the Hugoniot points at 4 GPa), the general sense of these results is to agree with the $CaCO_3$ I compressibility for stresses below 1.44 GPa, and with the $CaCO_3$ III compressibility for stresses above 1.74 GPa.

Figure 4-7 (particle velocity vs. shock velocity) shows slopes for the various compositions in rough agreement with the limestone fit for particle velocities above about 0.35 km/sec. Below this level, the precursors show much higher shock velocities (to nearly 8 km/sec).

In general, the more highly dolomitized Louisville limestone showed higher impedance than did the Jeffersonville limestone. No systematic difference between the frozen and corresponding thawed samples was observed, either in the Hugoniot state achieved or in the release. This is not surprising in view of the very low porosity of the samples tested.

4.5 Summary

Nine transmitted-wave experiments and one reverse-ballistic experiment were conducted to assess the relative responses of frozen and ambient carbonate materials to shock and release phenomena. Low-porosity samples were used with relatively discrete levels of dolomitization. In general, the more highly dolomitized Louisville limestone showed higher impedance than did the Jeffersonville limestone. It also did not show the precursors present in most of the more calcite-rich tests with Hugoniot stresses less than about 10 GPa. No systematic difference between the frozen and corresponding thawed samples was observed, either in the Hugoniot state achieved or in the release. This is not surprising in view of the very low porosity of the samples tested.

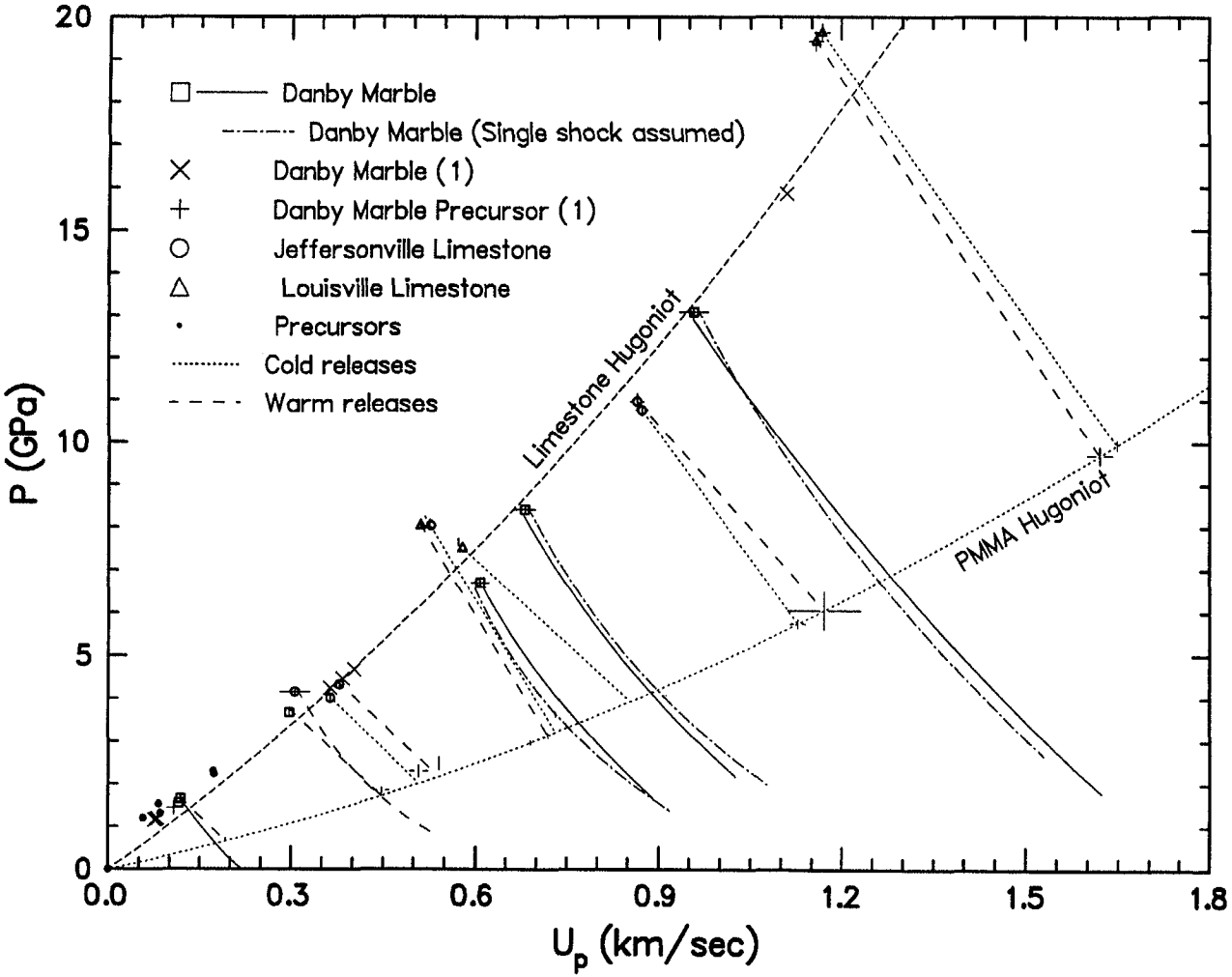

Figure 4-5. Stress-particle velocity diagram of Hugoniot and release results for Jeffersonville and Louisville Limestones and Danby Marble. Partial releases (straight) were determined from transmitted-wave experiments; curved were determined from reverse-ballistic experiments with alternate assumptions of single shocks and 2-wave loading. Precursor values shown are from transmitted wave experiments. (1) is Ktech data supplied by Gaffney.

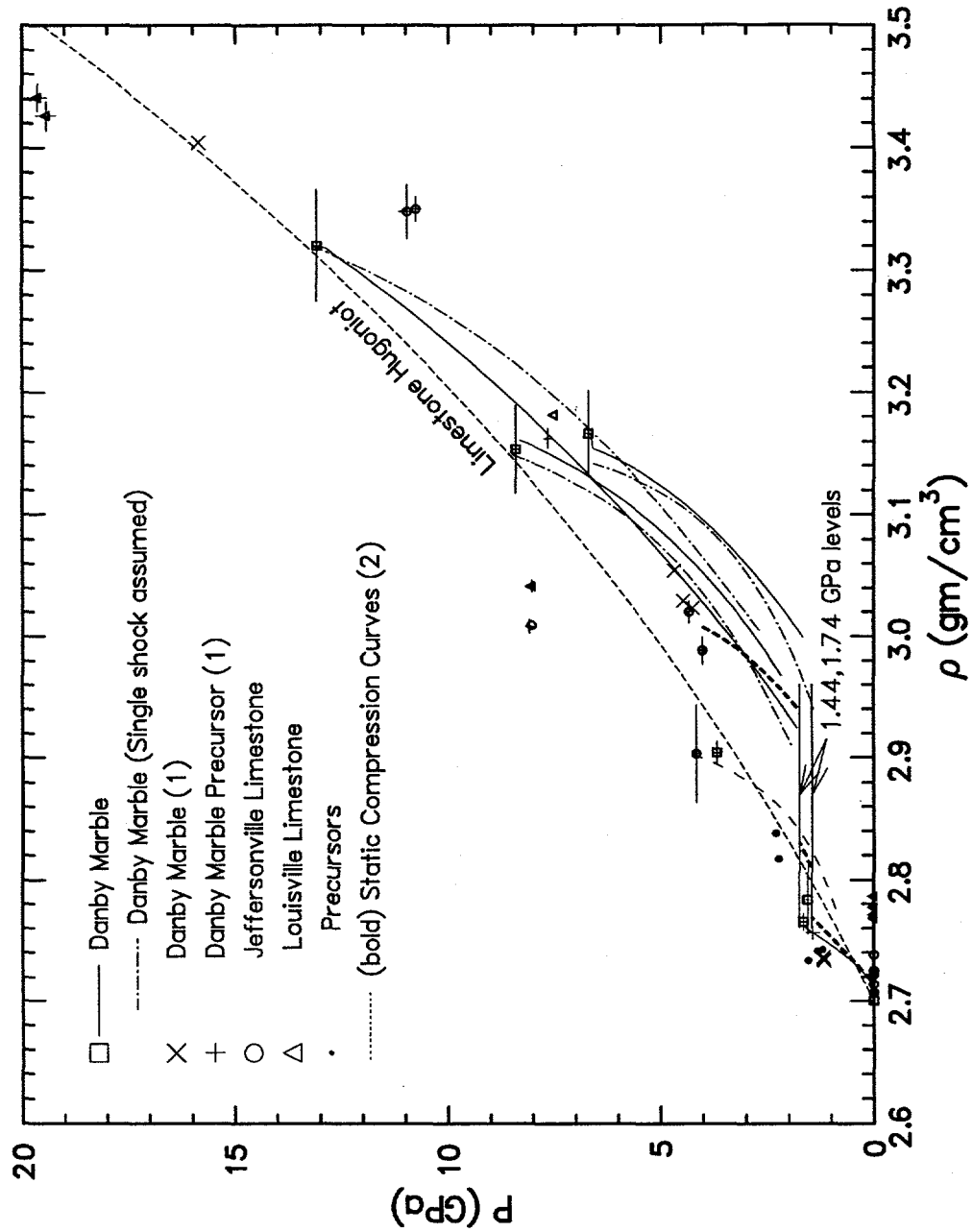

Figure 4-6. Stress-density diagram of Hugoniot results for Jeffersonville and Louisville Limestones and Danby Marble, with release paths from the applicable reverse-ballistic tests. Precursor values shown are from transmitted wave experiments. (1) is Ktech data supplied by Gaffney. Compression data (2) is from Singh and Kennedy [1974].

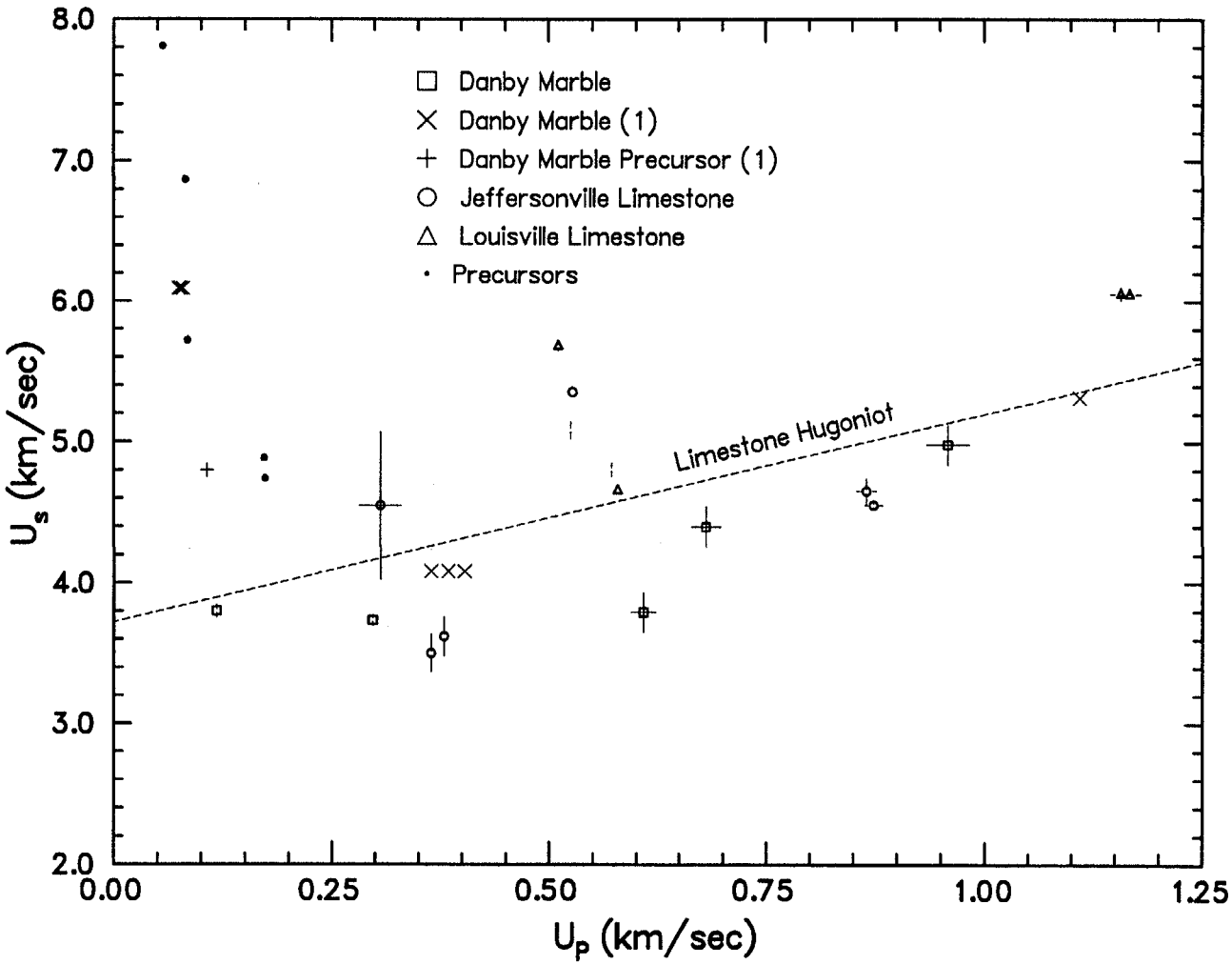

Figure 4-7. Shock velocity - particle velocity diagram of Hugoniot and release results for Jeffersonville and Louisville Limestones and Danby Marble. Precursor values shown are from transmitted wave experiments. (1) is Ktech data supplied by Gaffney.

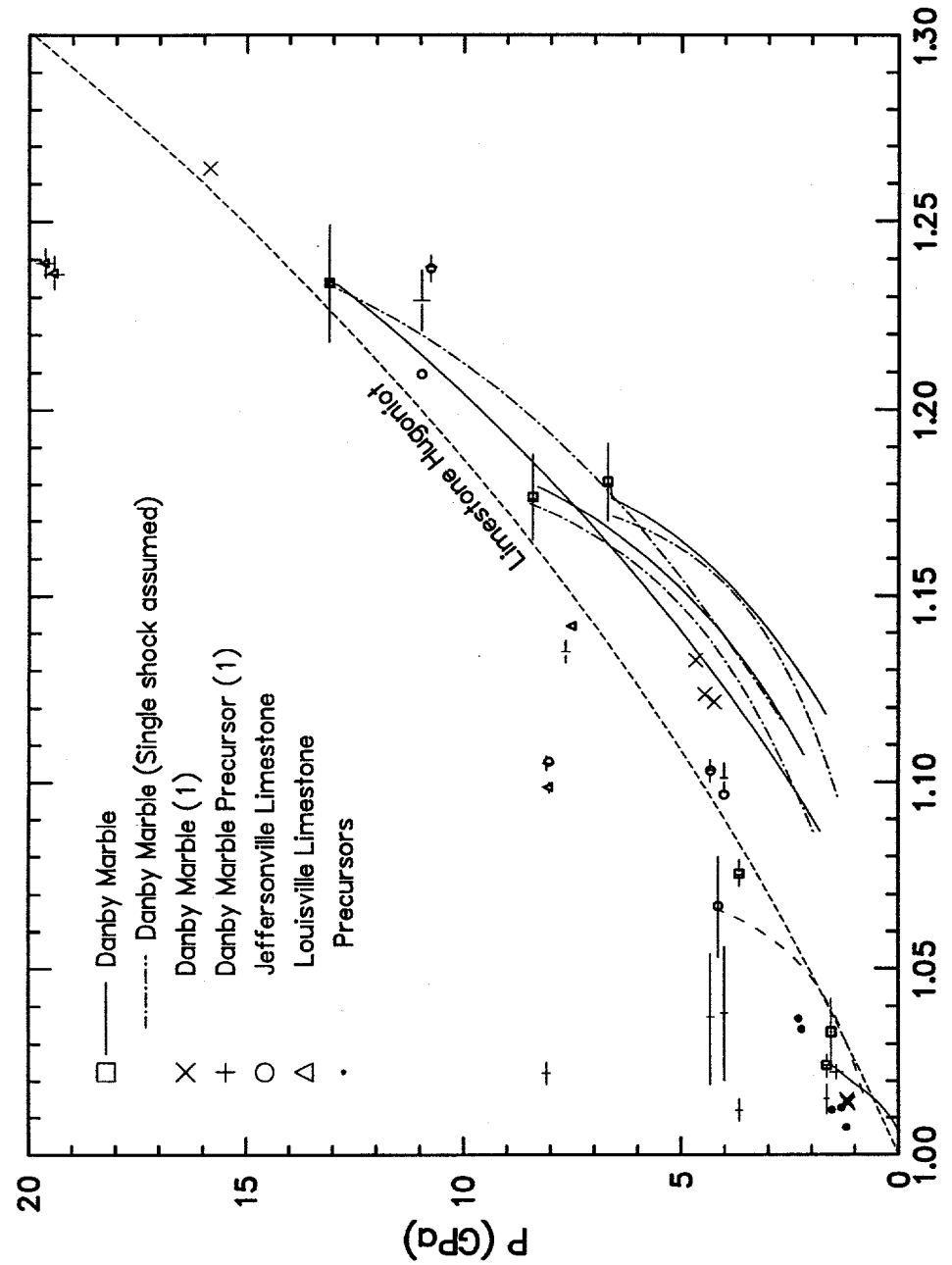

Figure 4-8. Stress-ρ/ρ_0 diagram of Hugoniot and release results for Jeffersonville and Louisville Limestones and Danby Marble. Releases were determined from reverse-ballistic experiments with alternate assumptions of single shocks and 2-wave loading. Precursor values shown are from transmitted wave experiments. (1) is Ktech data supplied by Gaffney.

5.0 Danby Marble

5.1 Motivation for study

A major issue throughout the groundshock community has been the scalability of rock properties between laboratory equation-of-state/constitutive properties tests and underground tests (UGT's). To this end, a portion of the HYDROPLUS program was devoted to intermediate-scale tests (several tons of high-explosive). Included in this effort were several carefully-controlled large-scale plane wave tests under the Distant Mountain label. A large volume (small swimming pool) of nitromethane was initiated by several thousand electrical detonators, driving a plane wave into a carefully constructed bed of quarried stone containing standard UGT groundshock instrumentation. Two of these tests were performed using marble provided by the Vermont Marble Company (Proctor, Vermont).

Laboratory-scale impact experiments were conducted on marble from the same source. Experiments were conducted at Sandia National Laboratories using VISAR instrumentation, and at the DNA Impact Facility, using predominately carbon stress-gauge instrumentation. The stress range of interest was 0 - 14 GPa.

The present section presents the results of the Sandia effort.

5.2 Material studied

Six tiles of marble were supplied by the Vermont Marble Company from which both Sandia and Ktech extracted disks for impact testing. The trade name for this material is Montclair Danby, from Proctor, Vermont. The tile utilized for the Sandia samples had discrete bands of lithics coursing through an apparently (visual appearance) nearly pure calcite marble. Samples were cut avoiding these bands.

The densities of these samples (2.68 - 2.70 gm/cm^3) are consistent with nearly pure marble with negligible dolomitization. Porosity is believed to be extremely low, in view of the density of the material and expected properties of marble. Crystal faces were easily seen by reflection; sizes were determined to be approximately a millimeter.

Sample preparation was done by machining the diameters required and surface-grinding to plane parallelism of approximately 0.0002" (5 μm). The tile faces were not assumed to be planar or parallel in this process.

5.3 Experiments conducted

Six impact experiments were conducted using VISAR instrumentation for measuring particle velocity histories. Parameters are summarized in Table 5.1. Two tests were conducted in a transmitted-wave configuration and four in a reverse-ballistics configuration.

Table 5.1. Test Matrix for Impact Studies of Danby Marble

Shot #	Gun Facility	Impact Velocity (km/sec)	Foam Density (gm/cm^3)	Foam Thick (mm)	Sample ID	Sample Density (gm/cm^3)	Sample Thick (mm)	Al Cup Thick (mm)	Buffer Material[1]	Buffer Thick (mm)	Window[2] Thick (mm)	Velocity[3] Per Fringe (km/sec)
DM6	Gas	0.219	0.322	4.864	Marble	2.694	5.971	(None)	Al	1.481	25.527	0.055995
DM7	Powder	1.0286	0.284	5.054	Marble	2.682	5.988	(None)	Al	1.680	25.624	0.10889
DM8	Powder	1.1985	0.290	4.958	Marble	2.680	5.969	(None)	Al	1.668	25.588	0.10889
DM9	Powder	1.721	5.044	0.621	Marble	2.691	5.965	(None)	Al	1.678	25.594	0.15527
Shot #	Gun Facility	Impact Velocity (km/sec)	Flyer Plate Thick[4] (mm)	Cup Thick (mm)	Sample ID	Sample Density (gm/cm^3)	Sample Thick (mm)			Buffer[5] Thick (mm)	Window[5] Thick (mm)	Velocity Per Fringe (km/sec)
DM10	Gas	0.2305	12.675	(None)	Marble	2.700	9.678			3.003	25.79	0.07240
DM11	Gas	0.5432	12.708	(None)	Marble	2.7006	9.424			2.995	25.505	0.07240

Reverse Ballistic

Forward Ballistic

[1]Standard aluminum used is 6061-T6 throughout assembly.

[2]Window is composed of lithium fluoride for reverse-ballistic tests in this study.

[3]Velocity per fringe (VPF) corresponds to a setting of the VISAR.

[4]In these forward-ballistic tests, the flyer plate is backed by a void

[5]Buffer and window are composed of PMMA for forward-ballistic tests in this study.

No cups were used in either configuration because the samples were competent and fluid loss was not an issue. Otherwise, the configurations were as described elsewhere in this report.

5.4 Dynamic properties results

5.4.1 Velocity profiles observed

The observed velocity profiles are presented in Figure 5-1. The transmitted-wave tests indicate the existence of a precursor of approximately 1.4 GPa amplitude. (see section

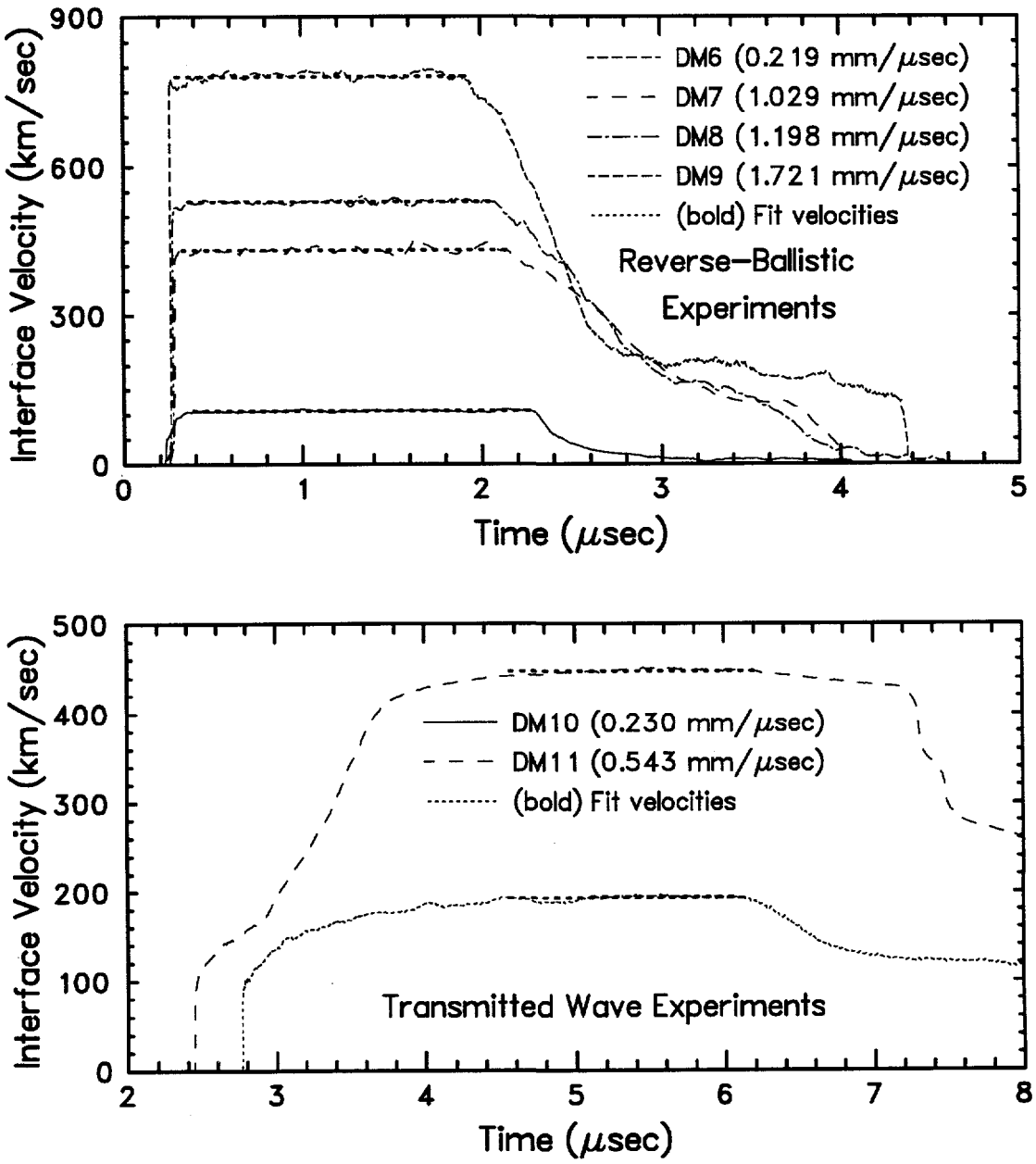

Figure 5-1. Velocity profiles for Danby Marble impact tests.

5.4.2), consistent with earlier studies of calcite mineralogies. This is shown most clearly in test DM-11; test DM-10 was conducted at a low-enough impact velocity that the plastic loading wave is dispersed and somewhat indistinct. The viscoelastic behavior of the PMMA buffers produced a prominent rounding of the loading and unloading portions of both velocity histories (see Schuler and Nunziato [1975]).

The reverse-ballistic tests provided the waveforms shown in the upper part of Figure 5-1. Because no cups were used, the initial plateau produced by the interaction of the cup with the target (Fig. 2-2) is absent. The releases show an indistinct step in the 150 - 250 m/sec interval, possibly corresponding to a $CaCO_3$ III $\rightarrow$ I transition (see Section 3.3.3). Interestingly, the step structure in the present release is markedly less distinct than for the 18% porosity Indiana Limestone. Perhaps the porosity and water saturation of the Indiana limestone facilitated the phase transition.

5.4.2 Dynamical properties calculated from wave profiles

Transmitted-Wave Experiments

For the transmitted-wave experiments, precursor and Hugoniot states were calculated from the times-of-arrival of the precursor and final waves and the plateau level of the precursor. The particle velocity and stress of a partial release point were calculated for each test from the main plateau level. The method was described in Section 3.3.2 and by Furnish [1993a, b]. Results are listed in Table 5.2

Table 5.2. Precursor and Hugoniot values from transmitted-wave experiments on Danby Marble.

				Precursor/Hugoniot Conditions					
Shot #	Proj. Velocity km/sec	Plastic TOA μsec	ρ_0 gm/cm^3	Particle Vel km/sec	Pressure GPa	ρ gm/cm^3	Shock Vel. km/sec	ρ/ρ_0	Specific Vol cm^3/gm
DM 10	0.230(3)	3.479(16)	2.700						
	Precursor Conditions →			0.08(2)	1.3(3)	2.741(10)	5.72(8)	1.015(4)	0.365(1)
	Hugoniot Conditions →			0.118(4)	1.65(5)	2.765(7)	3.80(4)	1.024(3)	0.3617(9)
Dm 11	0.543(6)	3.348(7)	2.701						
	Precursor Conditions →			0.08(2)	1.5(3)	2.733(7)	6.87(10)	1.012(3)	0.366(9)
	Hugoniot Conditions →			0.297(6)	3.67(9)	2.904(9)	3.74(3)	1.075(3)	0.3444(11)

	Partial Release Conditions		
Shot #	Plateau Velocity km/sec	Stress GPa	Particle Vel. km/sec
DM 10	0.193(4)	0.71(2)	0.193(4)
DM 11	0.447(12)	1.85(7)	0.447(12)

Reverse-Ballistic Experiments

The reverse-ballistic experiments provided Hugoniot information from the plateau velocity level. Release information derived from a wavecode matching of the observed release, which originated at the sample-foam interface was also available. Details of these calculations are described in Sections 2.2.2 and 3.3.2, and by Furnish [1993a,b]. The results are presented in Table 5.3. Uncertainties in the Hugoniot conditions are derived by adding in quadrature uncertainties in the following quantities:

- Precursor levels (taken as 1.4 ± 0.4 GPa at 6.26 km/sec). The difference made by assuming no precursor is tabulated in Table 5.3.
- Projectile Velocity
- Observed Plateau Velocity
- Initial Density
- Equations of state of aluminum and lithium fluoride (1% in stress at given particle velocity)

These are plotted together with the Jeffersonville and Louisville Limestone results in Figures 4-5 through 4-8. In general, the agreement with the expected physics ($CaCO_3$ I $\rightarrow$ III

Table 5.3. Hugoniot conditions for reverse-ballistic tests on Danby Marble.

(1) Assuming precursor 1.4 ± 0.4 GPa at 6.26 km/sec (the best guess)

				Hugoniot Conditions					
				Particle			Shock		Specific
Shot #	Proj. Velocity km/sec	Observed Vel. km/sec	ρ_0 gm/cm^3	Vel km/sec	Pressure GPa	ρ gm/cm^3	Vel. km/sec	ρ/ρ_0	Vol cm^3/gm
DM 6	0.219(2)	0.107(2)	2.694(14)	0.115(3)	1.54(3)	2.78(3)	1.7(1.9)	1.033(9)	0.359(4)
DM 7	1.029(10)	0.431(4)	2.682(14)	0.608(14)	6.69(5)	3.16(3)	3.79(14)	1.180(11)	0.316(3)
DM 8	1.199(12)	0.529(4)	2.680(14)	0.681(17)	8.41(6)	3.15(4)	4.40(14)	1.176(11)	0.317(4)
DM 9	1.721(17)	0.780(4)	2.691(13)	0.958(24)	13.09(10)	3.32(5)	4.98(14)	1.234(15)	0.301(4)

(2) Assuming no precursor (probably invalid)

				Hugoniot Conditions					
				Particle			Shock		Specific
Shot #	Proj. Velocity km/sec	Observed Vel. km/sec	ρ_0 gm/cm^3	Vel km/sec	Pressure GPa	ρ gm/cm^3	Vel. km/sec	ρ/ρ_0	Vol cm^3/gm
DM 6	0.219(2)	0.107(2)	2.694(14)	0.114(3)	1.54(3)	2.757(15)	5.02(21)	1.023(8)	0.363(2)
DM 7	1.029(10)	0.431(4)	2.682(14)	0.605(11)	6.64(7)	3.15(3)	4.09(10)	1.173(11)	0.318(3)
DM 8	1.199(12)	0.529(4)	2.680(14)	0.678(13)	8.35(8)	3.14(3)	4.60(11)	1.173(11)	0.318(3)
DM 9	1.721(17)	0.780(4)	2.691(13)	0.955(17)	13.03(11)	3.31(4)	5.07(11)	1.232(14)	0.302(3)

transition) and the fit to the data presented in Marsh [1980] (C_0 = 3.7225 km/sec, S = 1.4788, and ρ_0 = 2.70) is good.

Release paths were derived from the reverse-ballistic experiments by modeling the experiments with the Lagrangian finite-element wavecode WONDY V [Kipp and Lawrence, 1982]. The modeling chosen including a 2-step loading chosen to match the calculated Hugoniot pressure/density values of Table 5.3 (top) and appropriate precursor conditions. (Figure 5-2). These precursor conditions are a stress of 1.4 GPa and a density corresponding to that stress, the initial density (varying from test to test) and a precursor velocity of 6.26 km/sec. The unloading was governed by the usual release modulus:

$$(-V_0)\left.\frac{\partial\sigma}{\partial V}\right|_S \equiv B_S = B_0\left(1+\chi B_1+\chi^2 B_2+\chi^3 B_3\right) \qquad (\text{where } \chi \equiv \frac{\sigma}{\sigma_H}-1) \quad \text{(Eq. 5.1).}$$

These tests were also modeled assuming no precursor as a sensitivity study.

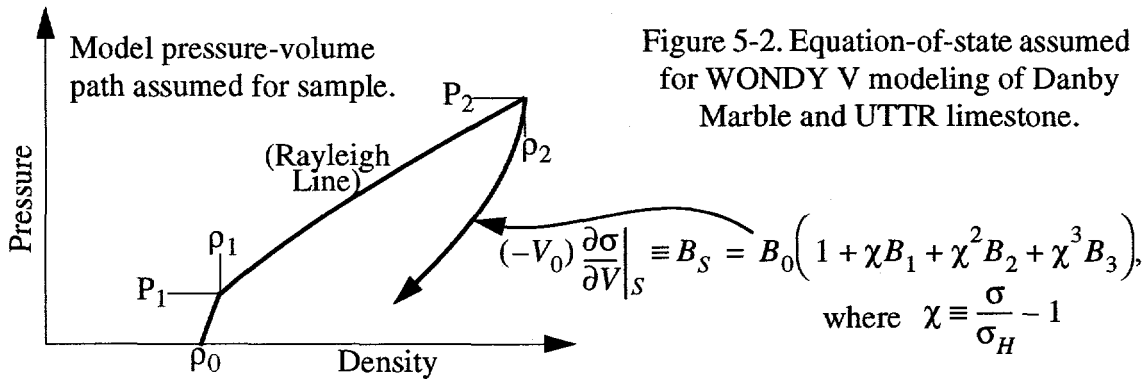

Figure 5-2. Equation-of-state assumed for WONDY V modeling of Danby Marble and UTTR limestone.

The release paths derived via these modelings are plotted in Figures 4-5, 4-6 and 4-8. Corresponding fits to the data are shown in Figures 5-3 (assuming two-wave loading for all tests except DM-6), and 5-4 (one-wave loading assumed for all tests).

I believe the two-wave loading to be the correct modeling (except for test DM-6, where the precursor state lies close to the final state). On physical grounds and to be consistent with the results of the forward-ballistic tests, the two-wave loading is strongly suggested. Furthermore, the two-wave loading model is predicted to give a shoulder at the start of the release; this is observed. The time-of-arrival of the onset of this shoulder does not agree well with the calculation, but the magnitude of the velocity drop across this shoulder is well reproduced by the calculation.

5.5 Summary

Six impact tests were conducted on a clean marble quarried from the same source as the marble used in large-scale tests in the Distant Mountain series. The transmitted-wave tests are consistent with a precursor propagating at 6.2 km/sec with a stress of 1.4 GPa, followed by a plastic loading. The reverse-ballistic tests provided Hugoniot points and release paths also consistent with such a loading. In general, the releases are hysteretic and strongly curved throughout the 1 - 13 GPa region studied.

Precursor Assumed:
Stress = 1.4 GPa
Shock Velocity = 6.26 km/sec

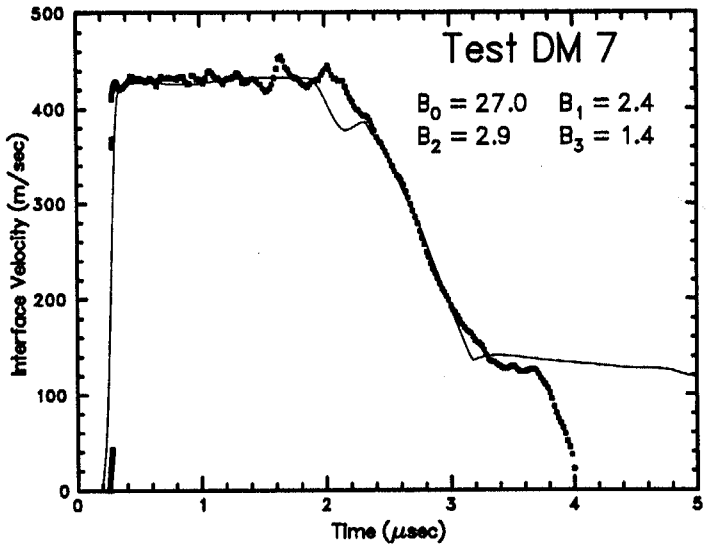

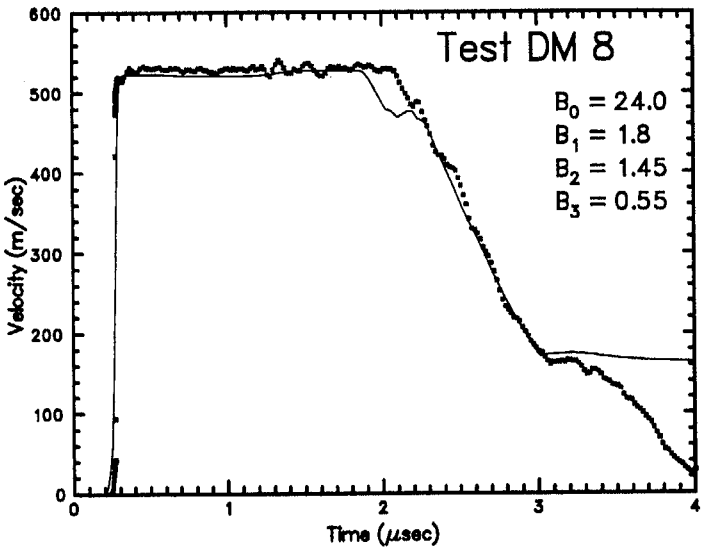

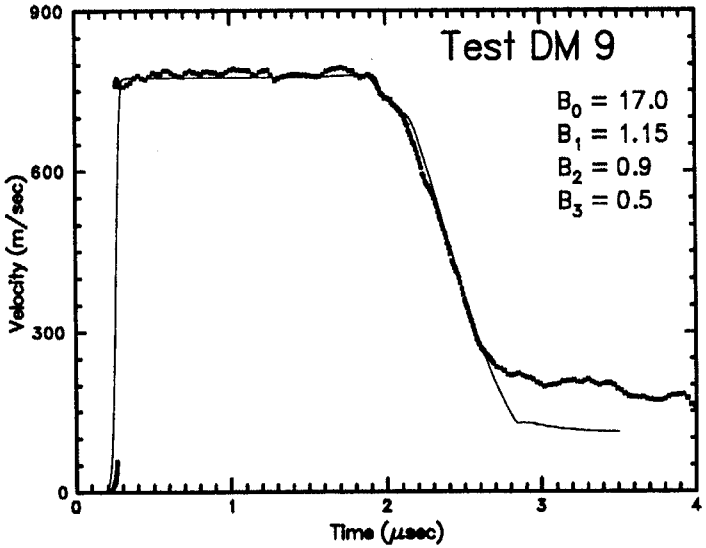

Figure 5-3. WONDY fits for Danby Marble tests DM7 - DM9, assuming 2-wave loading.

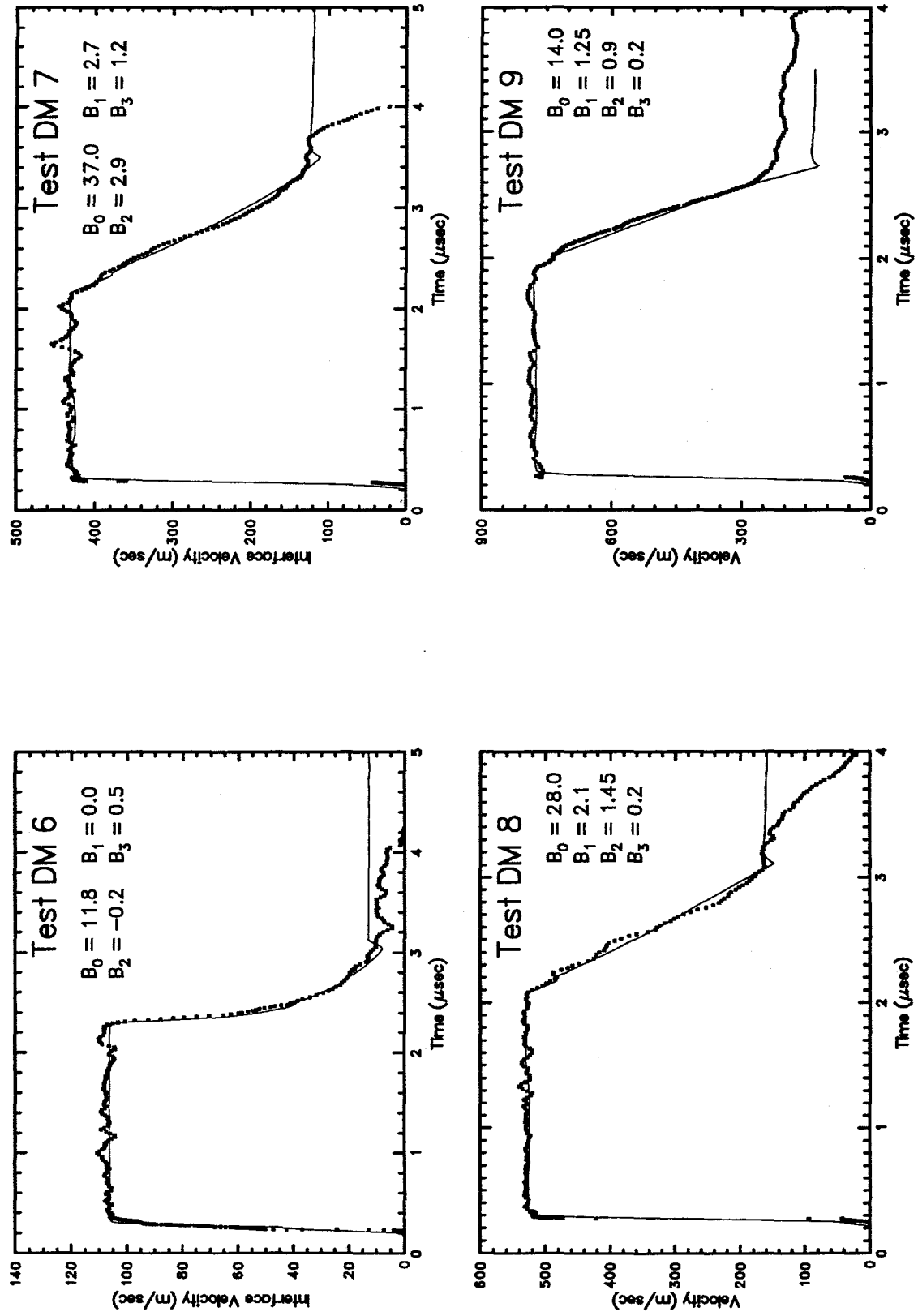

Figure 5-4. WONDY fits for Danby Marble tests DM7 - DM9, assuming 1-wave loading.

6.0 UTTR Limestone

6.1 Motivation for study

A study proposed under HYDROPLUS was to continue the study of scalability mentioned in the Motivation for Section 5. This study, planned for the Utah Test and Training Range, was to have included a large spherical detonation in a carbonate-rich mineralogy.

Sandia National Laboratories and the DNA Impact Facility performed laboratory-scale impact tests on material chosen as representative of the site of this large-scale test. As before, experiments conducted at Sandia National Laboratories used VISAR instrumentation, and those at the DNA Impact Facility used predominately carbon stress-gauge instrumentation. The stress range of interest was 0 - 14 GPa.

The present section presents the results of the Sandia effort, a set of five transmitted-wave experiments.

6.2 Material studied

A core of material was obtained from the CM02 drill hole (118' 4.2 - 7.3") [Martin, 1993]. Gas gun samples were prepared by Terra Tek, with no attempt made to preserve any moisture content. The densities of these samples were 2.678 - 2.688 gm/cm^3 (Terra Tek measurements) or 2.666 - 2.677 gm/cm^3 (Sandia measurements). The normative mineralogy was reported to us as 22% quartz, 75% calcite and 3% dolomite, which would correspond to an average grain density of 2.701 gm/cm^3. The porosity is then (very approximately) estimated as 0.7% to 1.1%.

6.3 Experiments conducted

A total of five tests were conducted, all in a transmitted-wave geometry. The geometry is shown in Figure 6-1, with the experimental parameters listed in Table 5.1. These tests utilized velocity interferometry (VISAR) as the primary diagnostic. As with the transmitted-wave tests reported in previous sections, Hugoniot states and loading information were obtained. In addition, since the sample shock impedance was very close to those of lithium fluoride and 6061-T6 aluminum (in fact, slightly softer), these tests also yielded release information from a state very close to the Hugoniot state. The traces were timed relative to impact using an electronic fiducial triggered by a shorting pin flush with the impact surface. This timing has been corrected for projectile tilt and data/fiducial travel time differences. The procedure is discussed in detail in Appendix B.

Table 6.1. Test matrix for UTTR limestone impact tests

Shot #	Gun Facility[3]	Impact Velocity (km/sec)	Flyer Plate Thick[2] (mm)	Foam Density (gm/cm^3)	Sample ID	Sample Density (gm/cm^3)	Sample Thick (mm)	Window[1] Thick (mm)
UT1	Gas	0.276	6.070	0.2986	# 1	2.669	9.903	25.439
UT2	Gas	0.516	6.070	0.2942	# 2	2.672	9.925	25.392
UT3	Gas	0.766	6.058	0.3015	# 3	2.666	9.961	25.324
UT4	Powder	1.011	5.979	0.2844	# 5	2.677	10.065	25.378
UT5	Powder	1.340	6.103	0.2844	# 6	2.673	10.058	25.436

Notes:

1. Window is composed of lithium fluoride for all tests in this study.
2. In these forward-ballistic tests, the flyer plate is backed by foam (density as noted; thickness ~ 5 mm)
3. Velocity per fringe (VPF) is 0.055995 km/sec for the present gas gun tests and 0.155296 m/sec for the present powder gun tests. This VPF assumes $\Delta v/v_0 = 0.28$ for LiF

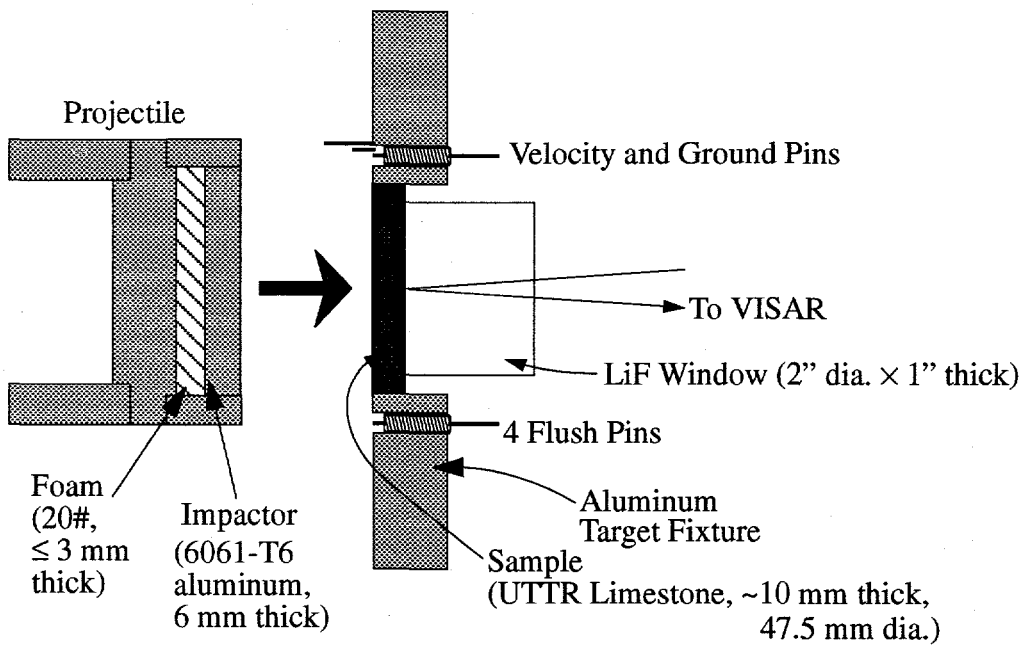

Figure 6-1. Transmitted-wave configuration used for UTTR limestone impact tests.

6.4 Dynamic properties results

6.4.1 Velocity profiles observed

The five tests produced the velocity profiles shown in Figure 6-2. All of the tests yielded distinct precursors which we interpret as due to the $CaCO_3$ I $\rightarrow$ III transition; the stress levels presented later corroborate this interpretation. UT-3 may show three distinct loading waves $CaCO_3$ I $\rightarrow$ II $\rightarrow$ III?). The plastic waves show the expected ramp-up behavior, trending toward overtake with increasing stress levels. Releases (propagated forward from the flyer/foam interface in the projectile through the sample) are show distinct structure in the two lower-stress tests (in fact, a rarefaction shock in the lowest-stress test), but less structure in the higher-stress tests. This is as expected. Velocity increases after about 5 μsec are probably due to reshock propagated through the foam (although the reshock behavior in UT-2 is earlier than expected). No analysis of this late-time behavior has been attempted.

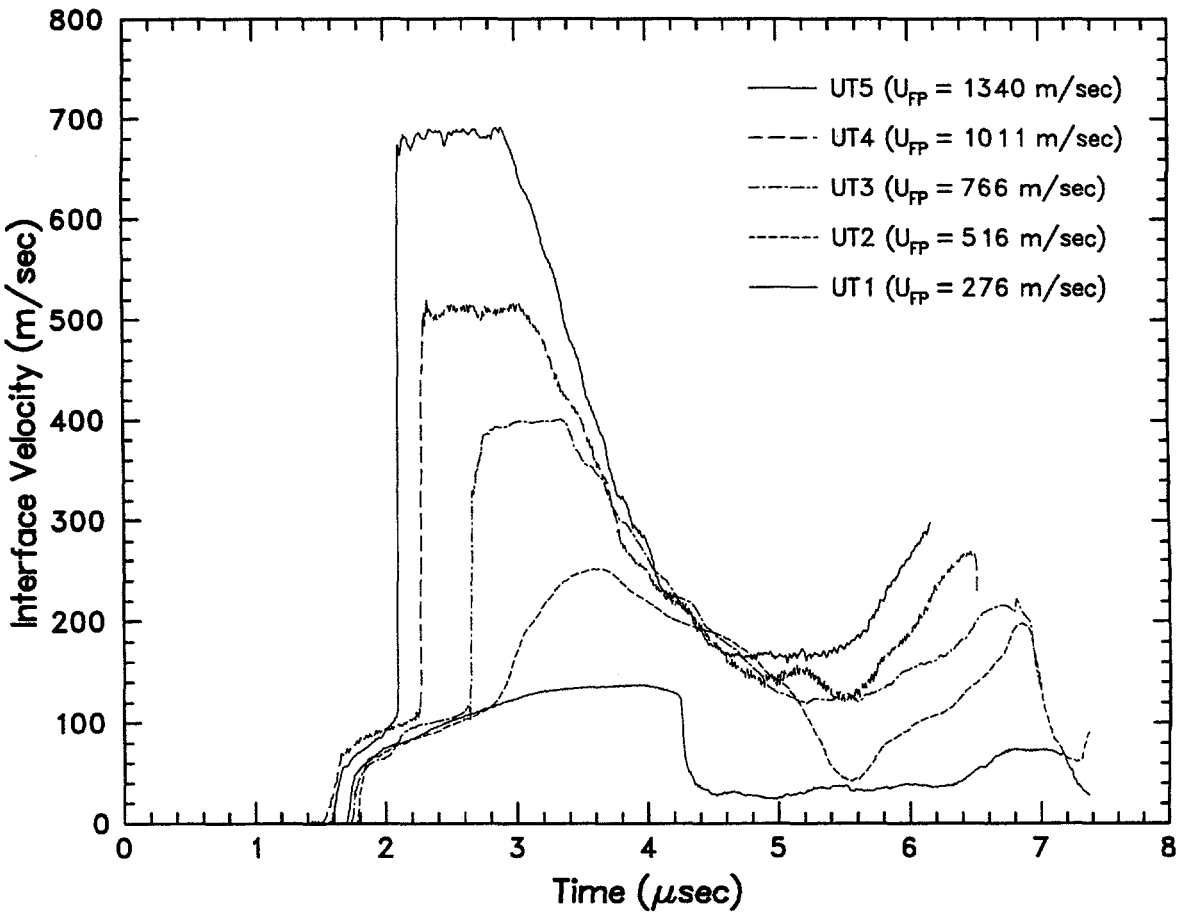

Figure 6-2. Velocity profiles from UTTR limestone impact tests.

6.4.2 Dynamical properties calculated from wave profiles

Three principal types of data reduction have been performed: (1) impedance-match calculations of precursors and Hugoniot states, (2) WONDY V modeling to extract release paths, and (3) explicit Lagrangian wave-evolution calculations to extract stress-strain loops (which are compared with the WONDY V results).

Impedance Match Results

Impedance match calculations proceed as discussed in earlier sections, with simple modifications to account for the use of a LiF window and elimination of a buffer. The results are presented in Table 6.2. The times-of-arrival used are given, and may be compared with

Table 6.2. Precursor and Hugoniot values from transmitted-wave experiments on UTTR Limestone.

				Precursor/Hugoniot Conditions →					
Shot #	Proj. Velocity km/sec	Plastic TOA μsec	ρ_0 gm/cm^3	Particle Vel km/sec	Pressure GPa	ρ gm/cm^3	Shock Vel. km/sec	ρ/ρ_0	Specific Vol cm^3/gm
UT 1	0.276	3.00(10)	2.669(5)						
	Precursor Conditions →			0.076(2)	1.17(4)	2.705(6)	5.7(3)	1.013(2)	0.370(1))
	Hugoniot Conditions →			0.153(3)	1.83(5)	2.77(1)	3.26(12)	1.038(2)	0.361(1)
UT 2	0.516	3.00(10)	2.672(6)						
	Precursor Conditions →			0.076(2)	1.12(3)	2.709(7)	5.5(3)	1.014(3)	0.369(1)
	Hugoniot Conditions →			0.309(5)	3.13(8)	2.92(2)	3.26(12)	1.092(5)	0.343(2)
UT 3	0.766	2.65(10)	2.666(12)						
	Precursor Conditions →			0.088(2)	1.28(4)	2.710(13)	5.5(3)	1.016(5)	0.369(2)
	Hugoniot Conditions →			0.454(8)	4.85(13)	3.01(2)	3.69(15)	1.128(8)	0.333(3)
UT 4	1.011	2.27(10)	2.677(11)						
	Precursor Conditions →			0.081(3)	1.40(5)	2.711(11)	6.4(4)	1.013(4)	0.369(2)
	Hugoniot Conditions →			0.569(11)	7.07(20)	3.05(3)	4.37(19)	1.140(12)	0.328(3)
UT 5	1.340	2.09(10)	2.673(10)						
	Precursor Conditions →			0.069(2)	1.14(4)	2.703(10)	6.2(4)	1.011(4)	0.370(1)
	Hugoniot Conditions →			0.750(15)	9.76(28)	3.16(4)	4.75(22)	1.181(15)	0.317(4)

	Reshock Conditions →		
Shot #	Plateau Velocity km/sec	Stress GPa	Particle Vel. km/sec
UT 1	0.137	2.02	0.137
UT 2	0.250	3.71	0.250
UT 3	0.398	6.09	0.398
UT 4	0.512	8.07	0.512
UT 5	0.690	11.28	0.690

the waveforms. In general, they correspond to half-maximum points. The calculations take into account the two-wave nature of the loading, and assume that the higher-pressure equation of state and index of refraction corrections for lithium fluoride can be used over the stress interval 0 - 7 GPa (a point discussed in Section 12 of Furnish [1993a]).

The precursors all show stresses in the general range of 1.4 GPa, with wave velocities generally in the 5.5 - 6.4 km/sec range.

Rather large uncertainties have been assigned the times-of-arrival due to an observed systematic timing discrepancy between the compressed gas gun test traces and the powder gun traces. These uncertainties have been propagated through the analysis.

Wavecode modeling to extract release paths

The WONDY V Lagrangian wavecode [Kipp and Lawrence, 1982] was used to model all of the experiments to infer release paths. The modeling used including a 2-step loading chosen to match the calculated precursor and Hugoniot pressure/density values of Table 6.2 (see Figure 5-2). The unloading was governed by the usual release modulus:

$$(-V_0)\left.\frac{\partial \sigma}{\partial V}\right|_S \equiv B_S = B_0\left(1 + \chi B_1 + \chi^2 B_2 + \chi^3 B_3\right) \qquad \left(\text{where } \chi \equiv \frac{\sigma}{\sigma_H} - 1\right) \quad \text{(Eq. 6.1).}$$

Note that this procedure has generally been applied to reverse-ballistic experiments, while here it is applied to a set of transmitted-wave experiments. This is reasonable because the Hugoniot state is relatively close to the reshock state reached after shock interaction with the lithium fluoride window (not the case in previous sections where a PMMA window was used).

The precursor and Hugoniot states are plotted in Figure 6-3, together with the release paths inferred from matching the WONDY V wave profile predictions to the observed waveforms. The perturbation corresponding to the trace timing uncertainty is illustrated in the stress vs. particle velocity plots in Figure 6-3.

The WONDY V wave profile calculations corresponding to the release paths in Figure 6-3 are shown in Figure 6-4. In general quite good agreement was obtained. The final plateau level is the most rigorous test of the models used; that is not prescribed in the input deck for the wavecode, but rather is a consequence of the Hugoniot and reshock/release properties specified. For UT2, 4 and 5, the plateau level agreement is excellent; for UT1 the calculated plateau is high (note that determining a plastic wave arrival time was difficult for this test because of the dispersed, slow arrival); and for UT3 it is low (this test may have had a three-wave loading, which was not accounted for in the model). The two versions of fits for UT4 are presented as indications of the robustness of this fitting process in determining release paths (see the corresponding release paths in Fig. 6-3).

Lagrangian wave-evolution calculation of stress-strain paths

In general, the waveform ($\sigma(t)$ or $U_p(t)$) must be known at a minimum of two locations in a sample to perform an explicit analysis of stress-strain paths traversed by the sample. For

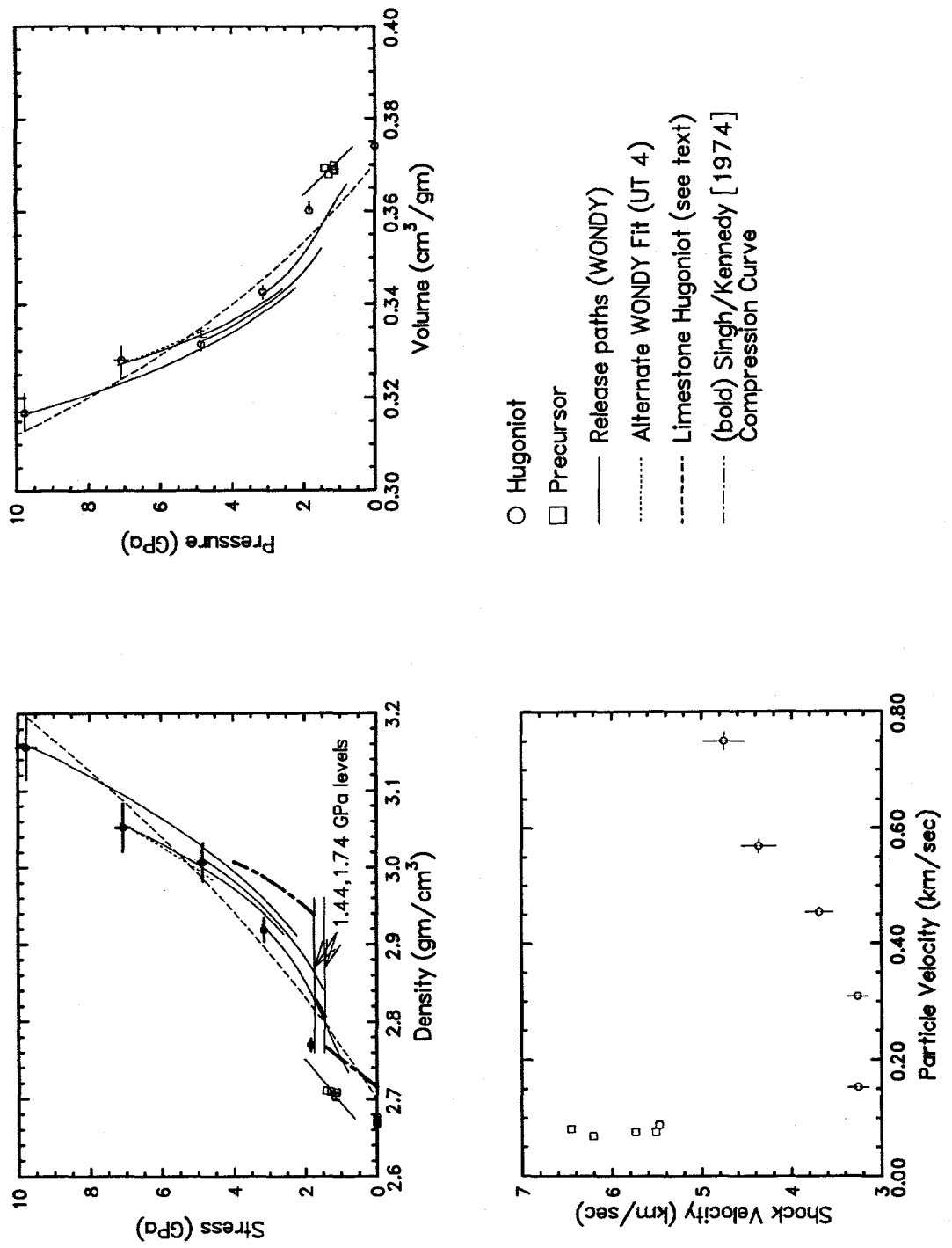

Figure 6-3. Precursor and Hugoniot conditions for UTTR limestone (derived by impedance-match methods) and release paths (derived by WONDY model waveform matching to experimental waveforms). Dashed Hugoniot is fit to data from Marsh [1980]

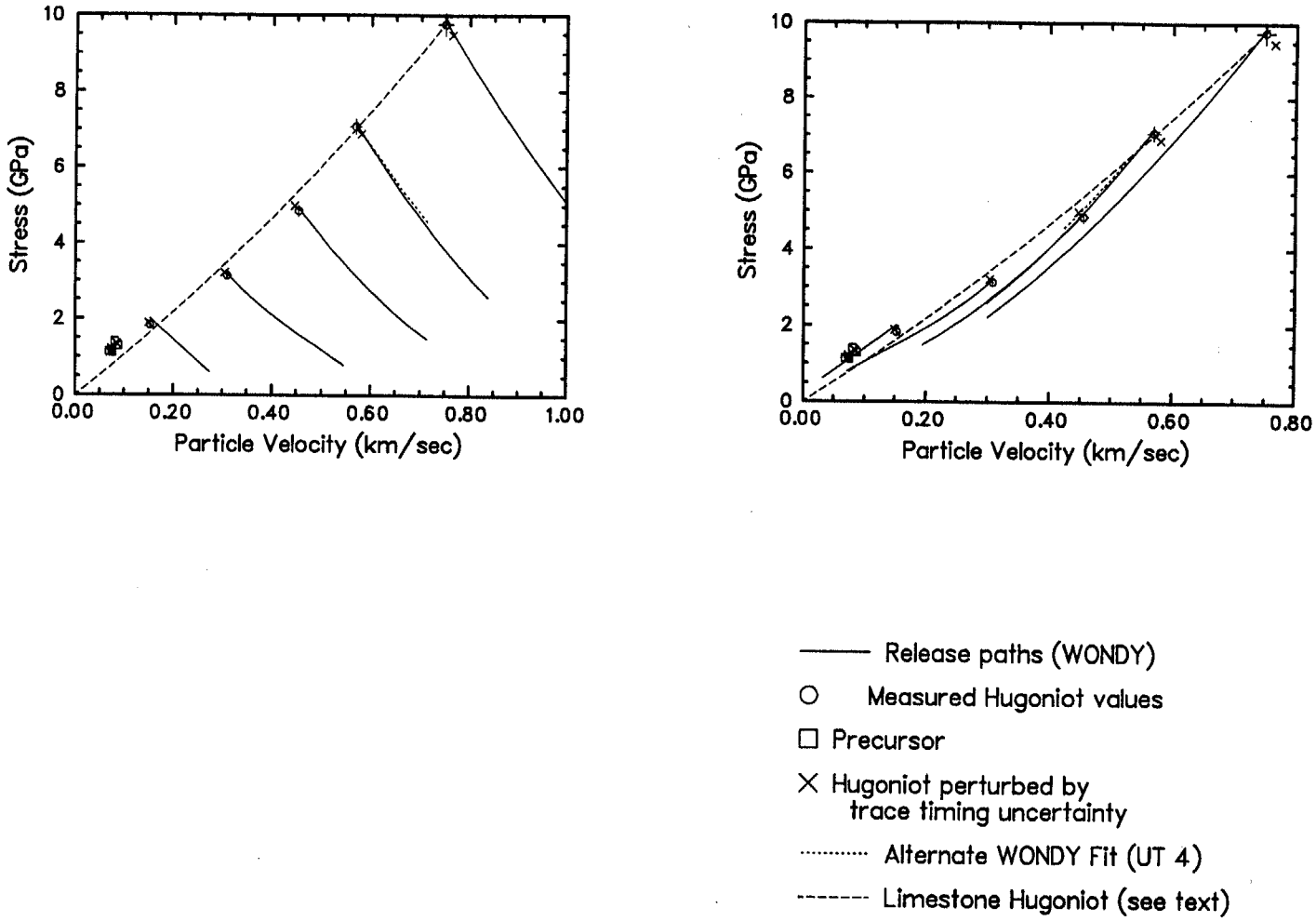

Figure 6-3 (Continued). Precursor and Hugoniot conditions for UTTR limestone (derived by impedance-match methods) and release paths (derived by WONDY model waveform matching to experimental waveforms).Dashed Hugoniot is fit to data from Marsh [1980].

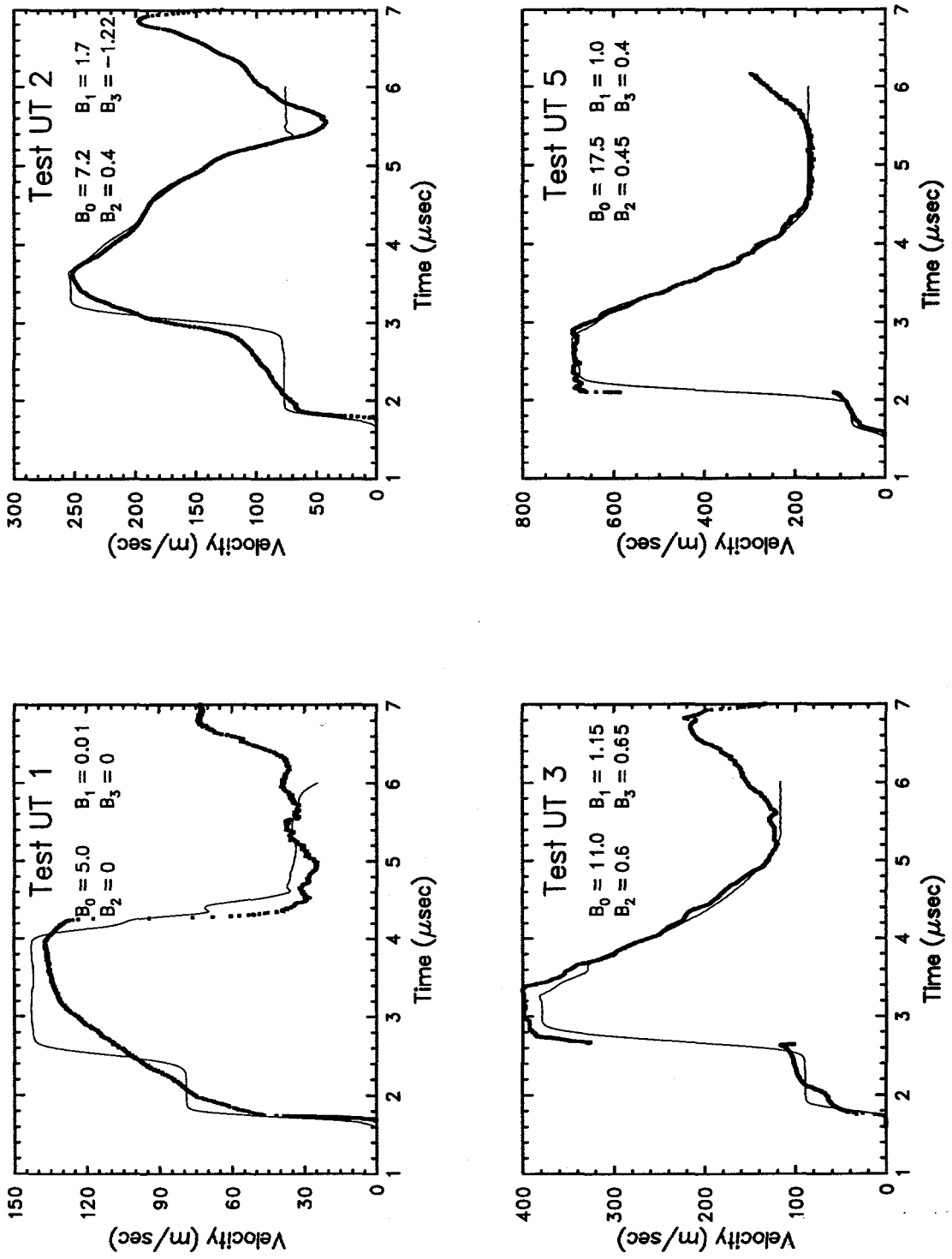

Figure 6-4. WONDY model waveforms corresponding to release paths of Figure 6-3, overlain on experimental waveforms

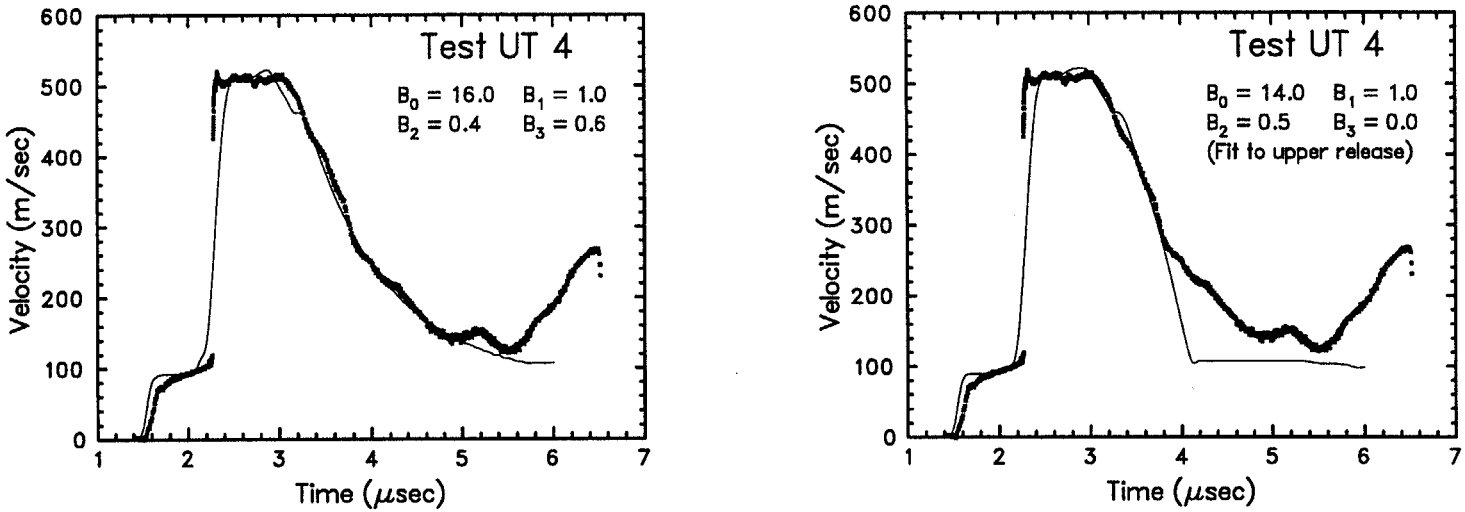

Figure 6-4 (Continued). WONDY model waveforms corresponding to release paths of Figure 6-3, overlain on experimental waveforms

the case of a VISAR experiment, this condition is met only for a forward ballistic experiment with VISAR monitoring of an interface contacting the sample, where other considerations allow the calculation or determination of the waveform entering the sample.

These conditions are met in the present set of experiments. The input wave to the sample may be calculated (more details below), and the output wave is measured. By contrast with the tests described in earlier sections of this report, the UTTR limestone tests utilized lithium fluoride windows. The waveforms measured at the sample/window interface are somewhat perturbed by the relatively small impedance mismatch, but wave contamination by reflected waves is small and nonlinear wave interactions are presumed to have a negligible effect in the present experiments.

Therefore, a Lagrangian wave-evolution calculation was undertaken to complement the WONDY V release path determinations and the impedance match precursor and Hugoniot calculations.

There are several programs available for implementing such a calculation for VISAR tests. In the present case it is possible to supply the observed waveform directly, along with information about sample thickness, original state of sample (stress, density, zero-stress density, initial material velocity), and the input waveform. Details of this procedure may be found in Grady and Young [1976].

A particularly simple version of the problem occurs when the input waveform is taken as a step loading at zero time, followed at a time T_1 by the onset of a ramp unloading of duration ΔT. Using this as an illustration, consider an iteration through the observed output velocity profile as follows (sequence of steps performed at each point in the iteration):

(1) Establish the impedance of the window material at the particular velocity in question, $Z_{win} = \rho_{0win} * C_{win}$ (where $C_{win} = (d\sigma_{win}/d\varepsilon_{win})^{1/2}$)

(2) Calculate the average Lagrangian wave velocity C_{sam} for this step (thickness/time for loading; thickness/(time-T_1) for unloading; further correct if unloading is a ramp)

(3) Calculate the impedance of the sample for this iteration as $Z_{sam} = \rho_{0sam} C_{sam}$.

(4) Calculate the stress increment as the average of the two impedances, Z_{avg}, times the observed particle velocity increment

(5) Calculate the sample particle velocity increment as Z_{avg}/Z_{sam} times the observed particle velocity increment

(6) Calculate the strain increment as the particle velocity increment divided by the Lagrangian wave speed (cf. eq. 11.5)

These steps have been implemented in a Fortran code and applied to the present tests. The input waveforms assumed are shown in Figure 6-5, juxtaposed on the WONDY predictions of the input waveforms.

The resulting stress-strain paths, recalculated as stress-density, are shown in Figure 6-6. These are juxtaposed on the trajectories extracted from the WONDY V matchings to the

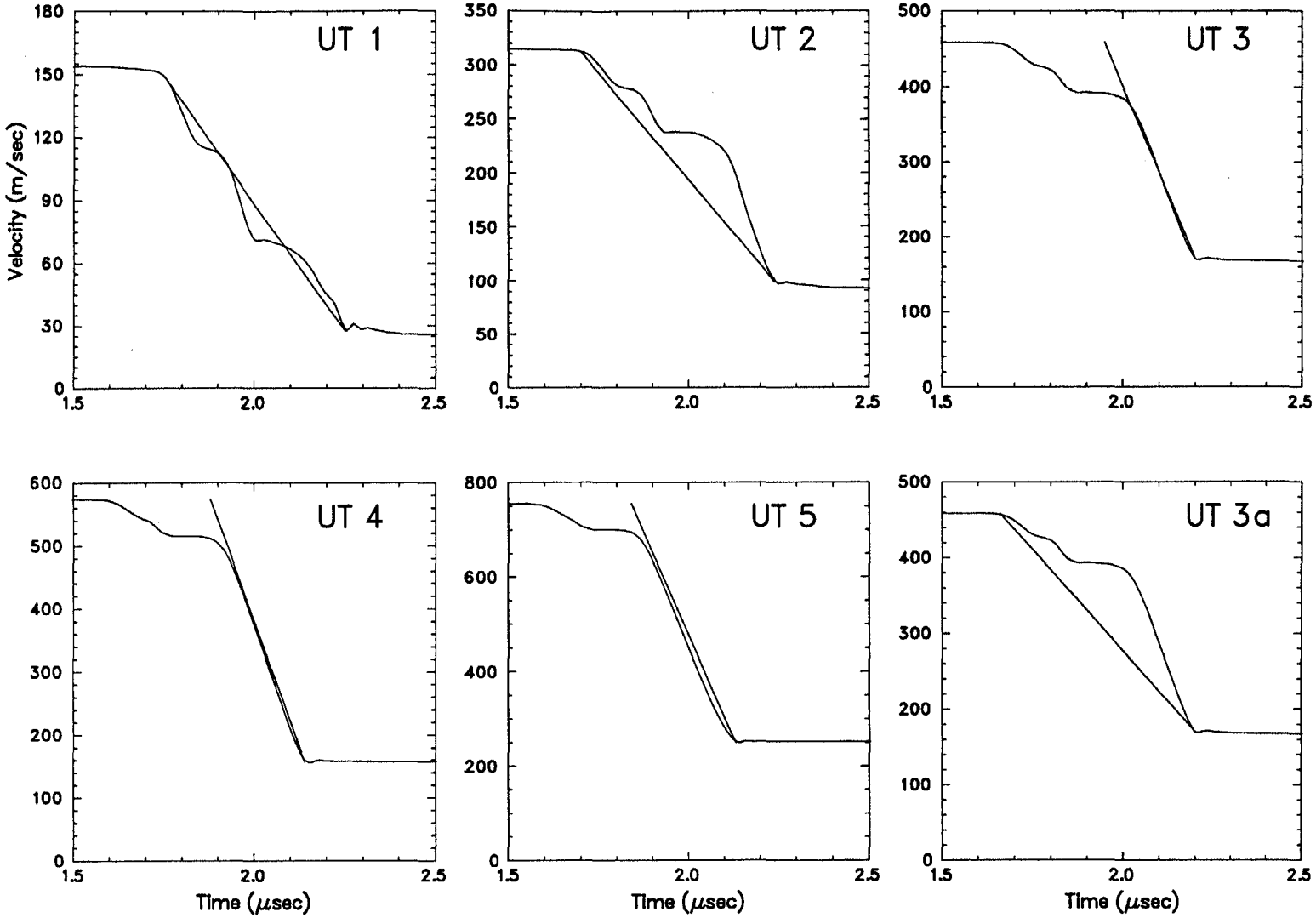

Figure 6-5. Assumed input waveforms for Lagrangian wave evolution analysis, juxtaposed on WONDY V models of input waveforms calculated during WONDY modeling of tests to extract release paths. UT3 and UT3a represent alternate inputs.

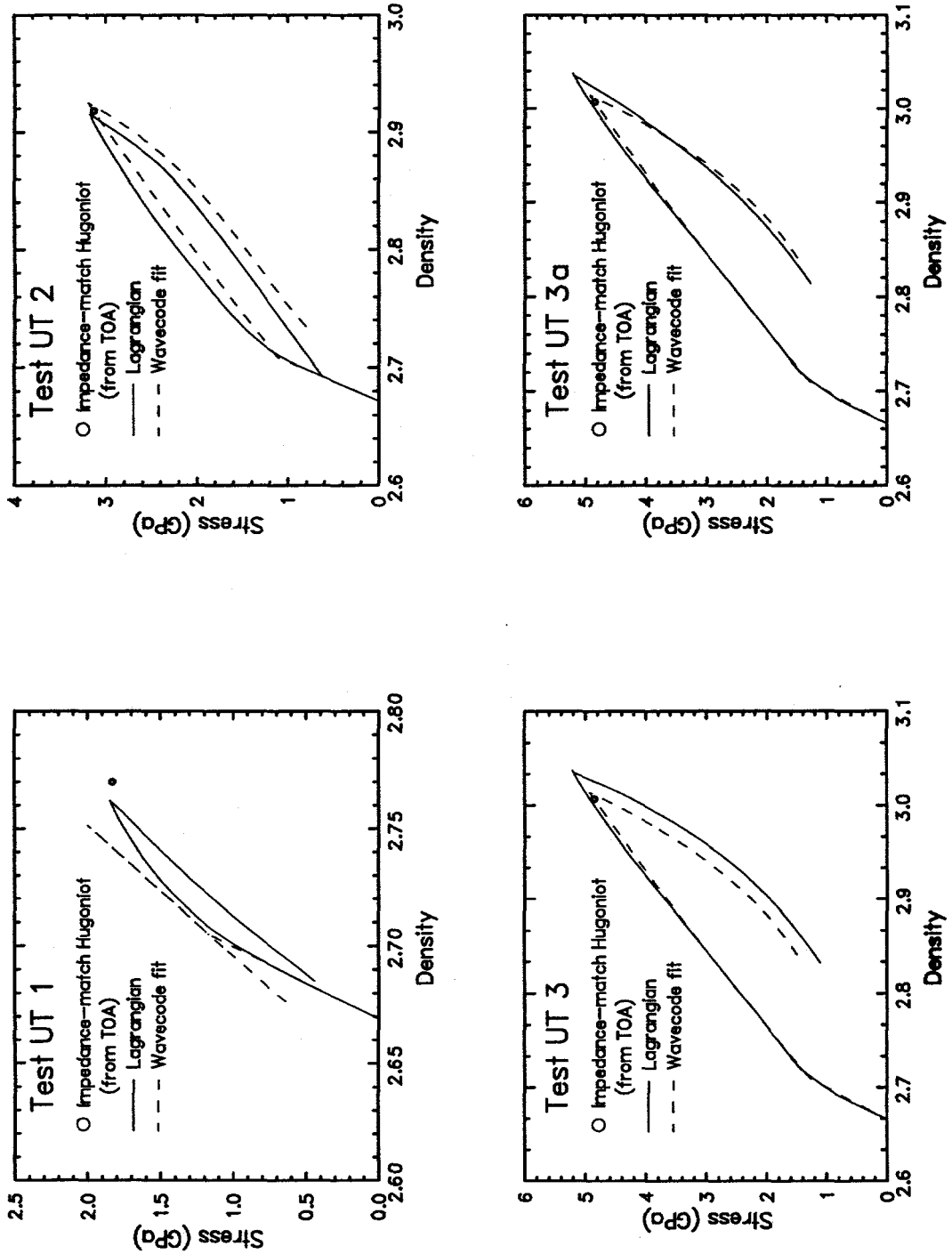

Figure 6-6. Stress-density paths calculated by Lagrangian waveform analysis for UTTR limestone tests. Similar paths calculated by iterative WONDY V matching of experimental wave profiles, and impedance-match Hugoniot states, are juxtaposed.

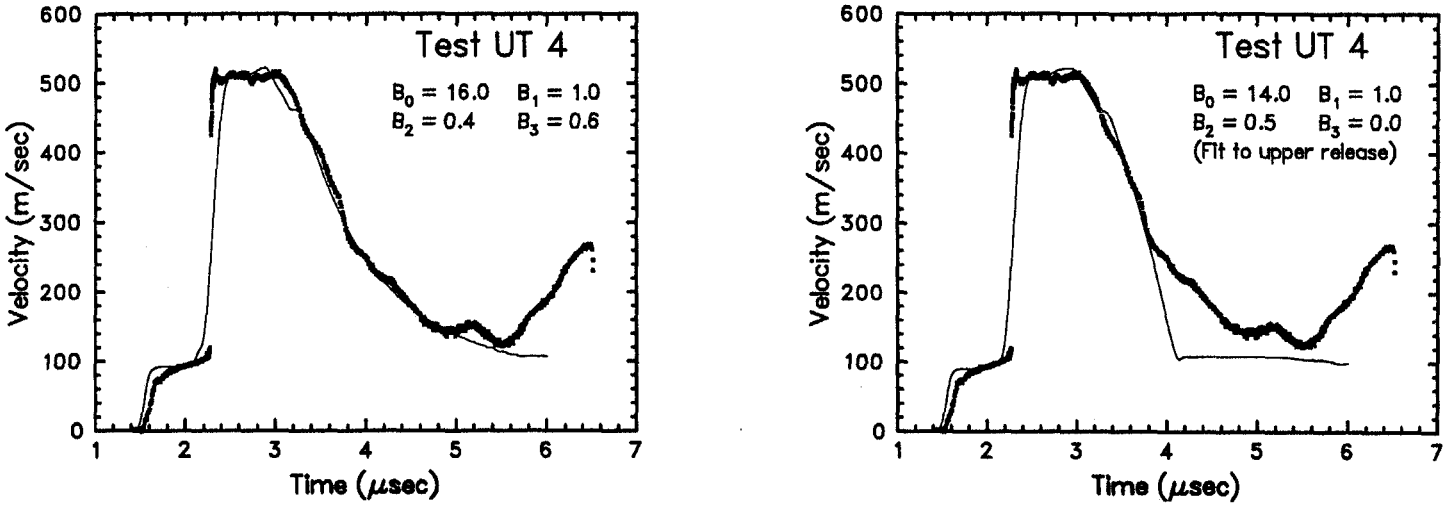

Figure 6-6 (continued). Stress-density paths calculated by Lagrangian waveform analysis for UTTR limestone tests. Similar paths calculated by iterative WONDY V matching of experimental wave profiles, and impedance-match Hugoniot states, are juxtaposed. UT3 and UT3a correspond to the alternate inputs shown in Figure 6-5.

experimental wave profiles, and on the Hugoniot values calculated by impedance-match methods.

6.5 Summary

A set of five transmitted-wave impact experiments has been performed on an impure, low-porosity limestone from the Utah Test Range. VISAR diagnostics were used. The stress range of this study spanned 0 - 10 GPa. Clean waveforms were obtained, showing 2-wave loading (and 3-wave loading in one case), where the wave splitting is associated with the $CaCO_3$ I $\rightarrow$ II $\rightarrow$ III set of phase transitions. Precursor, Hugoniot and mildly reshocked states were obtained by impedance match methods. Release paths were obtained by iterative matching of the wave profiles with the Lagrangian finite-element wavecode WONDY V. Stress-strain paths were obtained by explicit Lagrangian wave-evolution calculations, assuming sample input waveforms simplified from those predicted in the WONDY V runs. These three calculations agreed well with one another for stress levels above 5 GPa. In general, the hystereses are comparable. The lower-pressure tests show poorer agreement between the reduction methods; I am not sure why but suggest that strength of the sample and window may play a role. The WONDY loops include the impedance-match Hugoniot point (except for the case of UT 1), but generally go beyond it.

7.0 Conclusions

The response of a variety of carbonate materials to shock loading and release has been measured. Various experimental configurations were used, some optimized to yield detailed waveform information, others to yield a clean combination of Hugoniot states and release paths. All made use of velocity interferometry as a primary diagnostic. The stress range of 0 - 20 GPa was probed (in most cases, emphasizing the stress range 0 - 10 GPa). The primary physical processes operating in carbonate materials in this stress regime are material strength, porosity, and polymorphic phase transitions between the $CaCO_3$ phases I, II, III and VI. Hydration is also a significant reaction under certain conditions.

Specific summary comments about the individual materials studied follow:

Indiana Limestone: A relatively pure, fine-grained limestone of about 18% porosity was tested in water-saturated and desiccated conditions. Hugoniot stresses produced ranged from 0.6 GPa to 12 GPa. A comparison of the Hugoniot results for the saturated material suggests that a hydration reaction to produce ikaite ($CaCO_3 \cdot 6H_2O$) occurs on a shock timescale (< 1 μsec).

Wave profiles provided loading, release and reshock information. Release paths tend to lie along the Hugoniot, showing little hysteresis. Reshock results are similar except at stresses below 4 GPa, where strength effects become significant. Strength effects are also significant in the shock velocity of the Hugoniot state at stresses less than 4 GPa. Structure observed on the releases is tentatively attributed to phase transitions in the $CaCO_3$ I $\leftrightarrow$ (II) $\leftrightarrow$ III system. Finally, transmitted-wave experiments did not show evidence for precursors.

Jeffersonville/Louisville (Fort Knox) Limestones: A set of nine transmitted-wave experiments and one reverse-ballistic experiment was conducted to assess the relative responses of frozen and ambient carbonate materials to shock and release phenomena. Low-porosity samples were used with relatively discrete levels of dolomitization. In general, the more highly dolomitized Louisville limestone showed higher impedance than did the Jeffersonville limestone. It also did not show the precursors present in most of the more calcite-rich tests with Hugoniot stresses less than about 10 GPa. No systematic difference between the frozen and corresponding thawed samples was observed, either in the Hugoniot state achieved or in the release. This is not surprising in view of the very low porosity of the samples tested.

Danby Marble: Six impact tests were conducted on a clean marble quarried from the same source as the marble used in large-scale tests in the Distant Mountain series. The transmitted-wave tests are consistent with a precursor propagating at 6.2 km/sec with a stress of 1.4 GPa, followed by a plastic loading. The reverse-ballistic tests provided Hugoniot points and release paths also consistent with such a loading. In general, the releases are hysteretic and strongly curved throughout the 1 - 13 GPa region studied.

Utah Test Range Limestone: A set of five transmitted-wave impact experiments has been performed on an impure, low-porosity limestone from the Utah Test Range. VISAR diag-

nostics were used. The stress range of this study spanned 0 - 10 GPa. Clean waveforms were obtained, showing 2-wave loading (and 3-wave loading in one case), where the wave splitting is associated with the $CaCO_3$ I $\rightarrow$ II $\rightarrow$ III set of phase transitions. Precursor, Hugoniot and mildly reshocked states were obtained by impedance match methods. Release paths were obtained by iterative matching of the wave profiles with the Lagrangian finite-element wavecode WONDY V. Stress-strain paths were obtained by explicit Lagrangian wave-evolution calculations, assuming sample input waveforms simplified from those predicted in the WONDY V runs. These three calculations agreed well with one another for stress levels above 5 GPa. In general, the hystereses are comparable. The lower-pressure tests show poorer agreement between the reduction methods; I am not sure why but suggest that strength of the sample and window may play a role. The WONDY loops include the impedance-match Hugoniot point (except for the case of UT 1), but generally go beyond it.

References

Aidun, J. B and Y. M. Gupta, Shear wave measurements for improved characterization of shock-induced phase transformations in Carrera marble, *Geophys. Res. Lett., 16*, 191-194, 1989.

Barker, L. M. and R. E. Hollenbach, Laser interferometer for measuring high velocities of any reflecting surface, *J. Appl. Phys, 43*, 4669-4675, 1972.

Barker, L. M. and R. E. Hollenbach, Shock-wave studies of PMMA, fused silica, and sapphire, *J. Appl. Phys., 41,* 4208-4226, 1970.

Bell, P. M. and J. L. England, High-pressure differential thermal analysis of a fast reaction with CaCO3, pp. 176 - 178 in *Carnegie Inst. Wash Yearb. 63*, 176-178 (1964).

Carlson, W. D., The polymorphs of CaCO3 and the aragonite-calcite transformation, in Carbonates: Mineralogy and Chemistry, *Rev. Mineral., 11*, R. J. Reeder (ed.), Mineral. Soc. Am., Wash., DC, pp. 191-225, 1983.

Chhabildas, L. C., Survey of diagnostic tools used in hypervelocity impact studies, *Int. J. Impact Engng*, 5, 205-220, 1987.

Chhabildas, L. C., L. M. Barker, J. R. Asay and T. G. Trucano, Spall strength measurements on shock-loaded refractory metals, pp. 429-432 in *Shock Compression of Condensed Matter - 1989*, S. C. Schmidt, J. N. Johnson and L. W. Davison (eds.), Elsevier Science Publishers, 1990.

Davison, L. and R. A. Graham, Shock compression of solids, *Physics Reports 55*, 255, 1979.

Furnish, M. D., Measuring the dynamic compression and release behavior of rocks and grouts associated with Hydro-Plus, Sandia National Laboratories report, SAND92-0984, 1993a.

Furnish, M. D., Recent advances in methods for measuring the dynamic response of geological materials to 100 GPa, pp. 267-278 in *Int. J. Impact Engng, 14* (proceedings of 1992 Hypervelocity Impact Symposium), 1993b.(ref??)

Furnish, M. D., L. C. Chhabildas, D. J. Steinberg and G. T. Gray III, Dynamic material properties of refractory materials: Molybdenum, pp. 229 - 240 in High Strain Rate Behavior of Refractory Metals and Alloys, R. Asfahani, E. Chen and A. Crowson (eds.), The Minerals, Metals and Materials Society, 1992.

Gaffney, E. S. and E. A. Smith, HYDROPLUS Experimental Study of Dry, Saturated, and Frozen Geological Materials, DNA Report DNA-TR-93-74, 1994

Grady, D. E. and M. D. Furnish, Shock- and Release-Wave Properties of MJ-2 Grout, Sandia report SAND88-1642, 1988.

Grady, D. E., W. J. Murri and K. D. Mahrer, Shock compression of dolomite, J. Geophys. Res., 81, 889 - 893, 1976a.

Grady, D. E., R. E. Hollenbach, K. W. Schuler and J. F. Callender, Compression wave studies in Blair dolomite, Sandia National Laboratories report SAND 76-0005, 1976b.

Grady, D. E., R. E. Hollenbach and K. W. Schuler, Compression wave studies on calcite rock, J. Geophys. Res., 83, 2839 - 2849, 1978.

Grady, D. E., Compression wave studies in Oakhall limestone, Sandia National Laboratories report, SAND83-0370, 1983.

Grady, D. E., R. L. Moody and D. S. Drumheller, Release equation of state of dry and water-saturated porous calcite, Sandia National Laboratories report, SAND86-2110, 1986. (This report also presents results for Z-cut Iceland Spar single crystal calcite)

Grady, D. E. and E. Young, Evaluation of constitutive properties from velocity interferometer data, Sandia National Laboratories report SAND75-1650, 1976.

Heard, H. C., A. E. Abey and B. P. Bonner, High pressure mechanical properties of Indiana limestone, Lawrence Livermore National Lab report UCID-16501, 1974.

Hurlbut, C. S. and C. Klein, Manual of mineralogy, 19th ed., John Wiley and Sons, 1977

Jackson, A. E., initial shipment of targets for HPEOS testing, memo to distribution, Nov. 22, 1991.

Kalashnikov, N. G., M. N. Pavlovskiy, G. V. Simakov and R. F. Trunin, Dynamic compressibility of calcite-group minerals, Izv., Earth Phys, 2, 23-29, 1973.

Kerley, G. I., Equations of state for calcite minerals. I. Theoretical model for dry calcium carbonate. *High Pressure Research*, 1989, vol. 2, pp. 29-47, 1989.

Kerley, G. I., Theory of calcite equation of state, pp. 613-616 in *Shock Compression of Condensed Matter - 1989*, S. C. Schmidt, J. N. Johnson and L. W. Davison (eds.), Elsevier Science Publishers, 1990.

Kerley, G. I., CTH equations of state package: Porosity and reactive burn models, Sandia National Laboratories report SAND92-0553, 1992.

Kipp, M. E. and R. J. Lawrence, WONDY V - A one-dimensional finite-difference wave propagation code, Sandia Report SAND81-0930 (1982)

Larson. D. B., Physical model experimental data for fully saturated Indiana limestone, informal (handwritten) memorandum to John Rambo, May 19, 1988.

Marland, G., The stability of $CaCO_3 \cdot 6H_2O$ (ikaite), Geochim. Cosmochim. Acta, 39, 83-91, 1975.

Martin, W., memo to Mike Furnish dated March 22, 1993.

McQueen, R. G., S. P. Marsh, J. W. Taylor, J. N. Fritz and W. J. Carter, The equation of state of solids from shock wave studies, pp. 293 - 417 in R. Kinslow (ed.), *High Velocity Impact Phenomena*, Academic Press, 1970.

Merrill, L. and W. A. Bassett, The crystal structure of $CaCO_3$ (II), a high-pressure metastable phase of calcium carbonate, Acta. Cryst. B31, 343-349, 1975.

Merrill, L. and W. A. Bassett, Crystal structures of the high pressure phases of calcite, EOS Trans. AGU 53, 1121, 1972.

Murri, W. J., D. E. Grady and K. D. Mahrer, Equation of state of rocks (SRI Report, 1975)

Schuler, K. W. and J. W. Nunziato, The dynamic behavior of polymethyl methacrylate, Rheol. Acta, 13, 265-273, 1975.

Singh, A. K. and G. C. Kennedy, Compression of calcite to 40 kbar, J. Geophys. Res., 79, 2615-2622, 1974.

Swegle, J. W. and D. E. Grady, Shock viscosity and the prediction of shock wave rise times, J. Appl. Phys., 58, 692, 1985.

VanValkenburg, A., H. K. Mao and P. M. Bell, Ikaite ($CaCO_3 \cdot 6H_2O$), a phase more stable than calcite and aragonite ($CaCO_3$) at high water pressure, Carnegie Inst. Wash. Yearb., 70, 237-238, 1971.

Wise, J. L. and L. C. Chhabildas, Laser interferometer measurements of refractive index in shock-compressed materials, pp. 441-454 in Shock Waves in Condensed Matter, Y. M. Gupta (ed), Plenum, 1985.

Appendix A

Tabulated Release Paths

Release paths for the tests discussed in this report are presented in a filtered form in this Appendix. Each path is represented by the first (Hugoniot), second and last points on the portion of the release considered valid, with the interval between the second and last points covered by five equally spaced points. Units are GPa for pressure, cm^3/gm for volume, gm/cm^3 for density, km/sec for particle velocity U_p, and MJ/kg for specific energy. Particle velocity is presented both incrementing upward and incrementing downward from the Hugoniot value to facilitate comparison with the results of other experiments; the true sense for the reverse-ballistic experiments is upward incrementation since the shock and the release are propagating in opposite directions.

Shot names and numbers are the same as those used in the text and tables. They are arranged alphabetically. The B_i parameters are listed consecutively; e.g. for ILS 1, we have $B_0 = 177.3\times10^{10}$ Pa, $B_1 = 2.9$, $B_2 = 2.6$ and $B_3 = 0.4$, and for DM 7, $B_0 = 27.0\times10^{10}$ Pa, $B_1 = 2.4$, $B_2 = 2.9$ and $B_3 = 1.4$, with a quadratic viscosity coefficient of 10 (default is 2), a 14 kb, and a 2.7 gm/cc precursor.0.163 mm gap between the sample and the cup. Tests ILS10 and ILS12 have two-part releases (two sets of the B_i parameters, with the switchover at a fraction X of the Hugoniot stress.

Indiana Limestone - Saturated

SHOT ILS1 (1000 M/S) B = 177.3, 2.9, 2.6, 0.4

Pressure	Volume	Density	Up (+)	Energy	Up(-)
0.57008E+10	0.34849E-03	0.28695E+04	0.64100E+03	0.20683E+06	0.64100E+03
0.56829E+10	0.34853E-03	0.28692E+04	0.64186E+03	0.20659E+06	0.64014E+03
0.50333E+10	0.35032E-03	0.28545E+04	0.67592E+03	0.19724E+06	0.60608E+03
0.43837E+10	0.35295E-03	0.28333E+04	0.71716E+03	0.18529E+06	0.56484E+03
0.37341E+10	0.35702E-03	0.28010E+04	0.76843E+03	0.16928E+06	0.51357E+03
0.30845E+10	0.36364E-03	0.27500E+04	0.83386E+03	0.14735E+06	0.44814E+03
0.24349E+10	0.37437E-03	0.26712E+04	0.91717E+03	0.11877E+06	0.36483E+03
0.17853E+10	0.38872E-03	0.25726E+04	0.10137E+04	0.92242E+05	0.26830E+03

SHOT ILS2 (1297 M/S) B = 170 1.9 0.55 -0.55

Pressure	Volume	Density	Up (+)	Energy	Up(-)
0.79162E+10	0.33988E-03	0.29422E+04	0.80800E+03	0.32409E+06	0.80800E+03
0.79142E+10	0.33989E-03	0.29421E+04	0.80810E+03	0.32405E+06	0.80790E+03
0.70192E+10	0.34237E-03	0.29208E+04	0.85522E+03	0.30612E+06	0.76078E+03
0.61241E+10	0.34556E-03	0.28940E+04	0.90855E+03	0.28620E+06	0.70745E+03
0.52291E+10	0.34984E-03	0.28585E+04	0.97041E+03	0.26290E+06	0.64559E+03
0.43341E+10	0.35589E-03	0.28098E+04	0.10439E+04	0.23513E+06	0.57209E+03
0.34390E+10	0.36489E-03	0.27406E+04	0.11335E+04	0.20149E+06	0.48249E+03
0.25440E+10	0.37848E-03	0.26422E+04	0.12436E+04	0.16262E+06	0.37240E+03

SHOT ILS3 (1534 M/S) B = 197.9 1.8 1.0 0.1

Pressure	Volume	Density	Up (+)	Energy	Up(-)
0.95423E+10	0.32938E-03	0.30360E+04	0.94800E+03	0.43315E+06	0.94800E+03
0.95403E+10	0.32939E-03	0.30359E+04	0.94809E+03	0.43311E+06	0.94791E+03
0.85975E+10	0.33167E-03	0.30151E+04	0.99417E+03	0.41329E+06	0.90183E+03
0.76547E+10	0.33440E-03	0.29904E+04	0.10449E+04	0.39247E+06	0.85111E+03
0.67118E+10	0.33775E-03	0.29607E+04	0.11011E+04	0.36965E+06	0.79492E+03
0.57690E+10	0.34194E-03	0.29245E+04	0.11639E+04	0.34509E+06	0.73210E+03
0.48262E+10	0.34722E-03	0.28799E+04	0.12345E+04	0.31864E+06	0.66151E+03
0.38834E+10	0.35404E-03	0.28246E+04	0.13145E+04	0.29066E+06	0.58150E+03

SHOT ILS9 (209.6 M/S) B = 27.35 1.8 1.0 0.1

Pressure	Volume	Density	Up (+)	Energy	Up(-)
0.12857E+10	0.40723E-03	0.24556E+04	0.12500E+03	0.80887E+04	0.12500E+03
0.12852E+10	0.40724E-03	0.24556E+04	0.12505E+03	0.80802E+04	0.12495E+03
0.11774E+10	0.40896E-03	0.24452E+04	0.13866E+03	0.59828E+04	0.11134E+03
0.10696E+10	0.41097E-03	0.24333E+04	0.15339E+03	0.37675E+04	0.96610E+02
0.96185E+09	0.41337E-03	0.24192E+04	0.16945E+03	0.13924E+04	0.80554E+02
0.85407E+09	0.41624E-03	0.24024E+04	0.18705E+03	-0.11611E+04	0.62954E+02
0.74628E+09	0.41974E-03	0.23825E+04	0.20644E+03	-0.38951E+04	0.43560E+02
0.63850E+09	0.42405E-03	0.23582E+04	0.22799E+03	-0.68119E+04	0.22010E+02

ILS10 BA=57 1.05 1 0.4; BB=32 1.1 1 0.5 X=0.69 (Two-part release)

Pressure	Volume	Density	Up (+)	Energy	Up(-)
0.25175E+10	0.38873E-03	0.25725E+04	0.28100E+03	0.39135E+05	0.28100E+03
0.25132E+10	0.38875E-03	0.25723E+04	0.28133E+03	0.39070E+05	0.28067E+03
0.21624E+10	0.39154E-03	0.25540E+04	0.31260E+03	0.32760E+05	0.24940E+03
0.18116E+10	0.39469E-03	0.25336E+04	0.34582E+03	0.26848E+05	0.21618E+03
0.14607E+10	0.40063E-03	0.24960E+04	0.39122E+03	0.17639E+05	0.17078E+03
0.11099E+10	0.40780E-03	0.24522E+04	0.44134E+03	0.92456E+04	0.12066E+03
0.75908E+09	0.41573E-03	0.24054E+04	0.49409E+03	0.26784E+04	0.67910E+02
0.40825E+09	0.42460E-03	0.23551E+04	0.54987E+03	-0.17149E+04	0.12130E+02

ILS12 BA=97 3 3 0; BB=26.5 0.2 0.2 0.5 X=0.7 (Two-part release)

Pressure	Volume	Density	Up (+)	Energy	Up(-)
0.44896E+10	0.35779E-03	0.27949E+04	0.53000E+03	0.14043E+06	0.53000E+03
0.44890E+10	0.35779E-03	0.27949E+04	0.53004E+03	0.14041E+06	0.52996E+03
0.38442E+10	0.36129E-03	0.27679E+04	0.57868E+03	0.12619E+06	0.48132E+03
0.31994E+10	0.36695E-03	0.27251E+04	0.63898E+03	0.10680E+06	0.42102E+03
0.25546E+10	0.37760E-03	0.26484E+04	0.72170E+03	0.78154E+05	0.33830E+03

ILS12 (Continued)

Pressure	Volume	Density	Up (+)	Energy	Up(-)
0.19098E+10	0.38912E-03	0.25701E+04	0.80788E+03	0.55878E+05	0.25212E+03
0.12650E+10	0.40156E-03	0.24904E+04	0.89740E+03	0.39185E+05	0.16260E+03
0.62023E+09	0.41574E-03	0.24054E+04	0.99300E+03	0.27580E+05	0.67000E+02

ILS13 B = 95, 1.79, 1.0, 0.1

Pressure	Volume	Density	Up (+)	Energy	Up(-)
0.60037E+09	0.40878E-03	0.24463E+04	0.82000E+02	0.29427E+04	0.82000E+02
0.60003E+09	0.40878E-03	0.24463E+04	0.82024E+02	0.29417E+04	0.81976E+02
0.51704E+09	0.40917E-03	0.24440E+04	0.87698E+02	0.27317E+04	0.76302E+02
0.43405E+09	0.40969E-03	0.24409E+04	0.94217E+02	0.24981E+04	0.69783E+02
0.35107E+09	0.41038E-03	0.24368E+04	0.10181E+03	0.22362E+04	0.62186E+02
0.26808E+09	0.41137E-03	0.24309E+04	0.11082E+03	0.19463E+04	0.53182E+02
0.18509E+09	0.41278E-03	0.24226E+04	0.12165E+03	0.16416E+04	0.42353E+02
0.10210E+09	0.41485E-03	0.24105E+04	0.13473E+03	0.13648E+04	0.29270E+02

ILS14 B = 145 2.8 2.8 0.8

Pressure	Volume	Density	Up (+)	Energy	Up(-)
0.40499E+10	0.35850E-03	0.27894E+04	0.49400E+03	0.12309E+06	0.49400E+03
0.40474E+10	0.35851E-03	0.27894E+04	0.49410E+03	0.12307E+06	0.49390E+03
0.34408E+10	0.36064E-03	0.27728E+04	0.52991E+03	0.11533E+06	0.45809E+03
0.28342E+10	0.36412E-03	0.27464E+04	0.57566E+03	0.10484E+06	0.41234E+03
0.22276E+10	0.36990E-03	0.27035E+04	0.63472E+03	0.90733E+05	0.35328E+03
0.16210E+10	0.37921E-03	0.26370E+04	0.70975E+03	0.73612E+05	0.27825E+03
0.10144E+10	0.39153E-03	0.25542E+04	0.79615E+03	0.59645E+05	0.19185E+03
0.40776E+09	0.40354E-03	0.24781E+04	0.88152E+03	0.54887E+05	0.10648E+03

ILS15 B = 180, 2.4, 2.12, 0.63

Pressure	Volume	Density	Up (+)	Energy	Up(-)
0.94259E+10	0.34222E-03	0.29221E+04	0.87500E+03	0.36903E+06	0.87500E+03
0.94241E+10	0.34222E-03	0.29221E+04	0.87509E+03	0.36899E+06	0.87491E+03
0.80711E+10	0.34622E-03	0.28884E+04	0.94854E+03	0.33550E+06	0.80146E+03
0.67181E+10	0.35204E-03	0.28406E+04	0.10371E+04	0.29445E+06	0.71285E+03
0.53652E+10	0.36072E-03	0.27723E+04	0.11453E+04	0.24431E+06	0.60471E+03
0.40122E+10	0.37391E-03	0.26745E+04	0.12786E+04	0.18545E+06	0.47136E+03
0.26592E+10	0.39358E-03	0.25409E+04	0.14415E+04	0.12380E+06	0.30849E+03
0.13062E+10	0.42083E-03	0.23763E+04	0.16334E+04	0.74590E+05	0.11660E+03

Indiana Limestone (Dry)

Dry Limestone DLS1 B0=215.86 (3.4,3.275,0)

Pressure	Volume	Density	Up (+)	Energy	Up(-)
0.10949E+10	0.39602E-03	0.25251E+04	0.25100E+03	0.31813E+05	0.25100E+03
0.10924E+10	0.39604E-03	0.25250E+04	0.25124E+03	0.31787E+05	0.25076E+03
0.96170E+09	0.39635E-03	0.25230E+04	0.25741E+03	0.31483E+05	0.24459E+03
0.83100E+09	0.39691E-03	0.25195E+04	0.26597E+03	0.30991E+05	0.23603E+03
0.70030E+09	0.39793E-03	0.25130E+04	0.27743E+03	0.30236E+05	0.22457E+03
0.56959E+09	0.39975E-03	0.25016E+04	0.29284E+03	0.29137E+05	0.20916E+03
0.43889E+09	0.40176E-03	0.24891E+04	0.30906E+03	0.28592E+05	0.19294E+03
0.30819E+09	0.40372E-03	0.24770E+04	0.32505E+03	0.28217E+05	0.17695E+03

Dry Limestone DLS3 (125, 1.5, 0.9, 0.3)

Pressure	Volume	Density	Up (+)	Energy	Up(-)
0.31951E+10	0.34352E-03	0.29110E+04	0.59800E+03	0.17968E+06	0.59800E+03
0.31914E+10	0.34354E-03	0.29109E+04	0.59827E+03	0.17962E+06	0.59773E+03
0.27919E+10	0.34512E-03	0.28975E+04	0.62299E+03	0.17510E+06	0.57301E+03
0.23923E+10	0.34706E-03	0.28813E+04	0.65084E+03	0.17038E+06	0.54516E+03
0.19928E+10	0.34945E-03	0.28617E+04	0.68170E+03	0.16550E+06	0.51430E+03
0.15932E+10	0.35242E-03	0.28375E+04	0.71611E+03	0.16054E+06	0.47989E+03
0.11937E+10	0.35618E-03	0.28076E+04	0.75485E+03	0.15567E+06	0.44115E+03
0.79413E+09	0.36112E-03	0.27692E+04	0.79923E+03	0.15114E+06	0.39677E+03

Dry Limestone DLS6 (B = 210,1.25,0.4,0.05)

Pressure	Volume	Density	Up (+)	Energy	Up(-)
0.12194E+11	0.31618E-03	0.31628E+04	0.12930E+04	0.84113E+06	0.12930E+04
0.12180E+11	0.31622E-03	0.31624E+04	0.12938E+04	0.84064E+06	0.12922E+04
0.10701E+11	0.31968E-03	0.31282E+04	0.13651E+04	0.80316E+06	0.12209E+04
0.92229E+10	0.32374E-03	0.30889E+04	0.14424E+04	0.76620E+06	0.11436E+04
0.77443E+10	0.32861E-03	0.30431E+04	0.15273E+04	0.72873E+06	0.10587E+04
0.62657E+10	0.33455E-03	0.29891E+04	0.16209E+04	0.69124E+06	0.96509E+03
0.47872E+10	0.34201E-03	0.29239E+04	0.17259E+04	0.65353E+06	0.86008E+03
0.33086E+10	0.35175E-03	0.28429E+04	0.18458E+04	0.61777E+06	0.74020E+03

Dry Limestone DLS8 (B = 125,1.1,0.25,0)

Pressure	Volume	Density	Up (+)	Energy	Up(-)
0.57605E+10	0.33871E-03	0.29524E+04	0.80500E+03	0.32595E+06	0.80500E+03
0.57543E+10	0.33880E-03	0.29516E+04	0.80577E+03	0.32540E+06	0.80423E+03
0.49353E+10	0.34193E-03	0.29246E+04	0.85575E+03	0.30967E+06	0.75425E+03
0.41163E+10	0.34572E-03	0.28925E+04	0.91140E+03	0.29377E+06	0.69860E+03

Dry Limestone DLS8 (Continued)

Pressure	Volume	Density	Up (+)	Energy	Up(-)
0.32973E+10	0.35034E-03	0.28544E+04	0.97291E+03	0.27820E+06	0.63709E+03
0.24783E+10	0.35609E-03	0.28082E+04	0.10415E+04	0.26296E+06	0.56849E+03
0.16594E+10	0.36354E-03	0.27508E+04	0.11195E+04	0.24892E+06	0.49050E+03
0.84037E+09	0.37372E-03	0.26758E+04	0.12107E+04	0.23756E+06	0.39930E+03

Fort Knox Limestone

PF 2 B = 24, 1.7, 0.6, -0.15

Pressure	Volume	Density	Up (+)	Energy	Up(-)
0.42071E+10	0.34459E-03	0.29020E+04	0.30983E+03	0.47998E+05	0.30983E+03
0.42005E+10	0.34460E-03	0.29019E+04	0.31008E+03	0.47958E+05	0.30958E+03
0.36360E+10	0.34556E-03	0.28939E+04	0.33340E+03	0.44284E+05	0.28626E+03
0.30715E+10	0.34681E-03	0.28834E+04	0.35994E+03	0.40259E+05	0.25972E+03
0.25070E+10	0.34851E-03	0.28694E+04	0.39095E+03	0.35678E+05	0.22871E+03
0.19425E+10	0.35098E-03	0.28492E+04	0.42821E+03	0.30390E+05	0.19145E+03
0.13780E+10	0.35484E-03	0.28181E+04	0.47477E+03	0.24231E+05	0.14489E+03
0.81349E+09	0.36145E-03	0.27666E+04	0.53563E+03	0.17344E+05	0.84030E+02

Danby Marble

DM 6 B = 11.8, 0, -0.2, 0.50 S = 2.50

Pressure	Volume	Density	Up (+)	Energy	Up(-)
0.15966E+10	0.36231E-03	0.27601E+04	0.11891E+03	0.70702E+04	0.11891E+03
0.15964E+10	0.36231E-03	0.27601E+04	0.11893E+03	0.70681E+04	0.11889E+03
0.13347E+10	0.36313E-03	0.27538E+04	0.13361E+03	0.59035E+04	0.10421E+03
0.10730E+10	0.36396E-03	0.27475E+04	0.14835E+03	0.50670E+04	0.89465E+02
0.81126E+09	0.36483E-03	0.27411E+04	0.16340E+03	0.43712E+04	0.74423E+02
0.54955E+09	0.36578E-03	0.27339E+04	0.17916E+03	0.38064E+04	0.58659E+02
0.28784E+09	0.36694E-03	0.27253E+04	0.19657E+03	0.33706E+04	0.41251E+02
0.26124E+08	0.36870E-03	0.27122E+04	0.21796E+03	0.31408E+04	0.19860E+02

DM 7 B = 27, 2.4, 2.9, 1.4 QVC=10.0; 14 kb 2.7 gm/cc precursor

Pressure	Volume	Density	Up (+)	Energy	Up(-)
0.66360E+10	0.31596E-03	0.31650E+04	0.60500E+03	0.18880E+06	0.60500E+03
0.65907E+10	0.31708E-03	0.31537E+04	0.61215E+03	0.18139E+06	0.59785E+03
0.57707E+10	0.31844E-03	0.31403E+04	0.64552E+03	0.17309E+06	0.56448E+03
0.49508E+10	0.32026E-03	0.31224E+04	0.68406E+03	0.16353E+06	0.52594E+03
0.41308E+10	0.32262E-03	0.30997E+04	0.72798E+03	0.15306E+06	0.48202E+03

DM 7 (Continued)

Pressure	Volume	Density	Up (+)	Energy	Up(-)
0.33108E+10	0.32557E-03	0.30716E+04	0.77716E+03	0.14234E+06	0.43284E+03
0.24909E+10	0.32914E-03	0.30382E+04	0.83129E+03	0.13229E+06	0.37871E+03
0.16709E+10	0.33342E-03	0.29992E+04	0.89049E+03	0.12372E+06	0.31951E+03

DM 8 B = 24, 1.8, 1.45, 0.55 QVC = 4.0 Prec: 14 kb rho=2.716

Pressure	Volume	Density	Up (+)	Energy	Up(-)
0.82980E+10	0.31639E-03	0.31607E+04	0.67800E+03	0.23545E+06	0.67800E+03
0.82357E+10	0.31648E-03	0.31597E+04	0.68047E+03	0.23464E+06	0.67553E+03
0.72274E+10	0.31828E-03	0.31419E+04	0.72295E+03	0.22099E+06	0.63305E+03
0.62190E+10	0.32051E-03	0.31200E+04	0.77038E+03	0.20630E+06	0.58562E+03
0.52107E+10	0.32331E-03	0.30931E+04	0.82347E+03	0.19074E+06	0.53253E+03
0.42023E+10	0.32683E-03	0.30598E+04	0.88301E+03	0.17464E+06	0.47299E+03
0.31940E+10	0.33127E-03	0.30186E+04	0.94994E+03	0.15875E+06	0.40606E+03
0.21856E+10	0.33698E-03	0.29675E+04	0.10258E+04	0.14395E+06	0.33020E+03

DM 9 B = 17, 1.15, 0.9, 0.5 QVC = 6.0 Prec: 14 kb rho=2.727

Pressure	Volume	Density	Up (+)	Energy	Up(-)
0.13031E+11	0.30130E-03	0.33190E+04	0.95500E+03	0.45813E+06	0.95500E+03
0.12881E+11	0.30136E-03	0.33183E+04	0.95805E+03	0.45734E+06	0.95195E+03
0.11034E+11	0.30580E-03	0.32702E+04	0.10485E+04	0.40486E+06	0.86145E+03
0.91879E+10	0.31095E-03	0.32158E+04	0.11462E+04	0.35409E+06	0.76381E+03
0.73414E+10	0.31693E-03	0.31553E+04	0.12512E+04	0.30669E+06	0.65885E+03
0.54948E+10	0.32385E-03	0.30879E+04	0.13641E+04	0.26446E+06	0.54591E+03
0.36482E+10	0.33199E-03	0.30122E+04	0.14867E+04	0.22949E+06	0.42330E+03
0.18017E+10	0.34196E-03	0.29243E+04	0.16223E+04	0.20417E+06	0.28770E+03

DM 7 B = 37, 2.7, 2.9, 1.2 QVC = 6.0 (No precursor assumed)

Pressure	Volume	Density	Up (+)	Energy	Up(-)
0.65726E+10	0.31837E-03	0.31410E+04	0.59842E+03	0.17905E+06	0.59842E+03
0.65661E+10	0.31838E-03	0.31409E+04	0.59863E+03	0.17901E+06	0.59821E+03
0.57042E+10	0.31948E-03	0.31301E+04	0.62939E+03	0.17241E+06	0.56745E+03
0.48423E+10	0.32108E-03	0.31145E+04	0.66645E+03	0.16420E+06	0.53039E+03
0.39805E+10	0.32344E-03	0.30918E+04	0.71149E+03	0.15409E+06	0.48535E+03
0.31186E+10	0.32696E-03	0.30585E+04	0.76650E+03	0.14195E+06	0.43034E+03
0.22567E+10	0.33223E-03	0.30100E+04	0.83378E+03	0.12827E+06	0.36306E+03
0.13948E+10	0.34032E-03	0.29384E+04	0.91710E+03	0.11410E+06	0.27974E+03

DM 8 B = 28, 2.1, 1.45, 0.2 QVC = 4.0 (No precursor assumed)

Pressure	Volume	Density	Up (+)	Energy	Up(-)
0.84755E+10	0.31764E-03	0.31483E+04	0.68581E+03	0.23516E+06	0.68581E+03
0.84690E+10	0.31764E-03	0.31482E+04	0.68605E+03	0.23509E+06	0.68557E+03
0.73796E+10	0.31929E-03	0.31320E+04	0.72837E+03	0.22231E+06	0.64325E+03
0.62901E+10	0.32151E-03	0.31104E+04	0.77742E+03	0.20763E+06	0.59420E+03
0.52007E+10	0.32457E-03	0.30809E+04	0.83520E+03	0.19051E+06	0.53642E+03
0.41113E+10	0.32894E-03	0.30401E+04	0.90403E+03	0.17084E+06	0.46759E+03
0.30218E+10	0.33517E-03	0.29836E+04	0.98630E+03	0.14943E+06	0.38532E+03
0.19324E+10	0.34367E-03	0.29098E+04	0.10825E+04	0.12931E+06	0.28912E+03

DM 9 B = 14, 1.25, 0.9, 0.2 QVC = 6.0 (No precursor assumed)

Pressure	Volume	Density	Up (+)	Energy	Up(-)
0.13174E+11	0.30124E-03	0.33196E+04	0.96288E+03	0.46357E+06	0.96288E+03
0.13172E+11	0.30124E-03	0.33196E+04	0.96294E+03	0.46355E+06	0.96282E+03
0.11422E+11	0.30384E-03	0.32912E+04	0.10304E+04	0.43217E+06	0.89538E+03
0.96724E+10	0.30722E-03	0.32550E+04	0.11072E+04	0.39775E+06	0.81858E+03
0.79226E+10	0.31161E-03	0.32092E+04	0.11947E+04	0.36065E+06	0.73105E+03
0.61728E+10	0.31726E-03	0.31520E+04	0.12941E+04	0.32257E+06	0.63165E+03
0.44230E+10	0.32438E-03	0.30829E+04	0.14057E+04	0.28715E+06	0.52010E+03
0.26732E+10	0.33293E-03	0.30036E+04	0.15280E+04	0.25968E+06	0.39776E+03

UTTR Limestone

UT 1 B = 5.0, 0.01, 0.0, 0.0

Pressure	Volume	Density	Up (+)	Energy	Up(-)
0.20008E+10	0.36344E-03	0.27515E+04	0.15300E+03	0.11240E+05	0.15300E+03
0.19931E+10	0.36349E-03	0.27511E+04	0.15366E+03	0.11127E+05	0.15234E+03
0.17620E+10	0.36522E-03	0.27380E+04	0.17367E+03	0.79312E+04	0.13233E+03
0.15309E+10	0.36696E-03	0.27251E+04	0.19368E+03	0.51531E+04	0.11232E+03
0.12998E+10	0.36870E-03	0.27123E+04	0.21371E+03	0.27674E+04	0.92293E+02
0.10687E+10	0.37044E-03	0.26995E+04	0.23374E+03	0.80561E+03	0.72260E+02
0.83764E+09	0.37217E-03	0.26870E+04	0.25379E+03	-0.80613E+03	0.52208E+02
0.60655E+09	0.37391E-03	0.26744E+04	0.27386E+03	-0.20048E+04	0.32140E+02

Ut 2 B = 7.2, 1.7, 0.4, -1.22

Pressure	Volume	Density	Up (+)	Energy	Up(-)
0.31934E+10	0.34191E-03	0.29248E+04	0.30900E+03	0.51643E+05	0.30900E+03
0.31928E+10	0.34191E-03	0.29247E+04	0.30905E+03	0.51631E+05	0.30895E+03
0.27926E+10	0.34416E-03	0.29056E+04	0.33903E+03	0.44965E+05	0.27897E+03

Ut 2 (Continued)

Pressure	Volume	Density	Up (+)	Energy	Up(-)
0.23923E+10	0.34703E-03	0.28816E+04	0.37290E+03	0.37604E+05	0.24510E+03
0.19921E+10	0.35075E-03	0.28510E+04	0.41147E+03	0.29535E+05	0.20653E+03
0.15919E+10	0.35543E-03	0.28134E+04	0.45475E+03	0.21286E+05	0.16325E+03
0.11917E+10	0.36074E-03	0.27720E+04	0.50084E+03	0.14191E+05	0.11716E+03
0.79142E+09	0.36578E-03	0.27339E+04	0.54570E+03	0.95624E+04	0.72300E+02

UT 3 B = 11.0, 1.15, 0.6, 0.65

Pressure	Volume	Density	Up (+)	Energy	Up(-)
0.49308E+10	0.33179E-03	0.30140E+04	0.45400E+03	0.10677E+06	0.45400E+03
0.49299E+10	0.33179E-03	0.30140E+04	0.45405E+03	0.10676E+06	0.45395E+03
0.43575E+10	0.33384E-03	0.29955E+04	0.48830E+03	0.97328E+05	0.41970E+03
0.37850E+10	0.33620E-03	0.29744E+04	0.52501E+03	0.87845E+05	0.38299E+03
0.32126E+10	0.33894E-03	0.29504E+04	0.56461E+03	0.78410E+05	0.34339E+03
0.26401E+10	0.34220E-03	0.29223E+04	0.60783E+03	0.69037E+05	0.30017E+03
0.20677E+10	0.34629E-03	0.28877E+04	0.65621E+03	0.59592E+05	0.25179E+03
0.14952E+10	0.35198E-03	0.28411E+04	0.71315E+03	0.49680E+05	0.19485E+03

UT 4 B = 16, 1.0, 0.4, 0.

Pressure	Volume	Density	Up (+)	Energy	Up(-)
0.71620E+10	0.32702E-03	0.30579E+04	0.56900E+03	0.16663E+06	0.56900E+03
0.71606E+10	0.32703E-03	0.30579E+04	0.56908E+03	0.16660E+06	0.56892E+03
0.63986E+10	0.32888E-03	0.30406E+04	0.60665E+03	0.15415E+06	0.53135E+03
0.56366E+10	0.33095E-03	0.30216E+04	0.64638E+03	0.14182E+06	0.49162E+03
0.48746E+10	0.33329E-03	0.30004E+04	0.68857E+03	0.12977E+06	0.44943E+03
0.41126E+10	0.33598E-03	0.29764E+04	0.73384E+03	0.11796E+06	0.40416E+03
0.33506E+10	0.33919E-03	0.29482E+04	0.78330E+03	0.10624E+06	0.35470E+03
0.25886E+10	0.34328E-03	0.29131E+04	0.83905E+03	0.94337E+05	0.29895E+03

UT 5 B= 17.5, 1, 0.5, 0.4

Pressure	Volume	Density	Up (+)	Energy	Up(-)
0.98564E+10	0.31628E-03	0.31618E+04	0.75000E+03	0.28500E+06	0.75000E+03
0.98550E+10	0.31628E-03	0.31617E+04	0.75007E+03	0.28497E+06	0.74993E+03
0.85827E+10	0.31915E-03	0.31333E+04	0.81052E+03	0.25870E+06	0.68948E+03
0.73104E+10	0.32244E-03	0.31013E+04	0.87514E+03	0.23307E+06	0.62486E+03
0.60381E+10	0.32623E-03	0.30653E+04	0.94455E+03	0.20837E+06	0.55545E+03
0.47658E+10	0.33071E-03	0.30239E+04	0.10200E+04	0.18474E+06	0.48004E+03
0.34935E+10	0.33620E-03	0.29744E+04	0.11036E+04	0.16246E+06	0.39642E+03
0.22212E+10	0.34349E-03	0.29113E+04	0.11997E+04	0.14222E+06	0.30030E+03

Appendix B

Establishing Impact Time on Observed Waveform

The procedure used for timing velocity (or stress-wave) profiles relative to impact may best be presented as a series of corrections. The data available for this process is as follows:

(1) A fiducial mark in the data traces produced by a shorting event signaling a contact between the projectile and a pin mounted on the target, nearly flush with the impact surface.

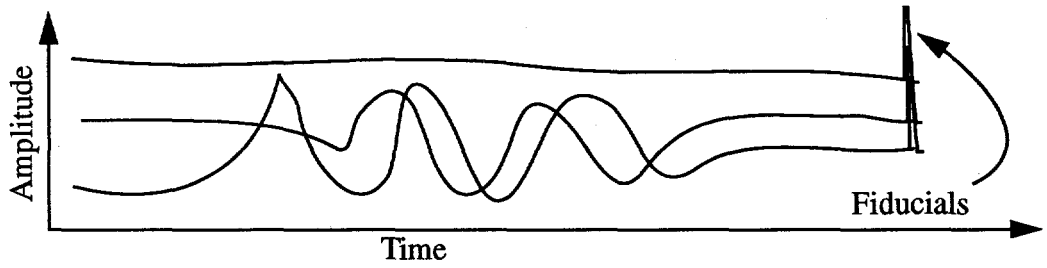

(2) Measurements of projectile velocity based on time intervals between shorting events involving pins of well-calibrated positions relative to the target contacting the advancing projectile,

(3) Measurements of impact tilt based on time intervals between shorting events involving pins nearly flush with the impact surface on the target, distributed at 90° intervals around the target circumference.

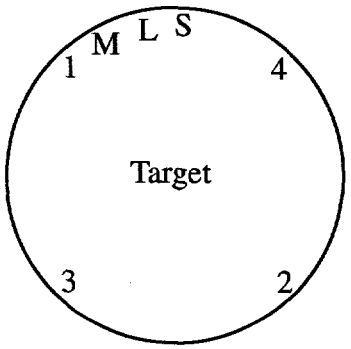

Flush Pins 1 - 4
Velocity Pins S, M, L

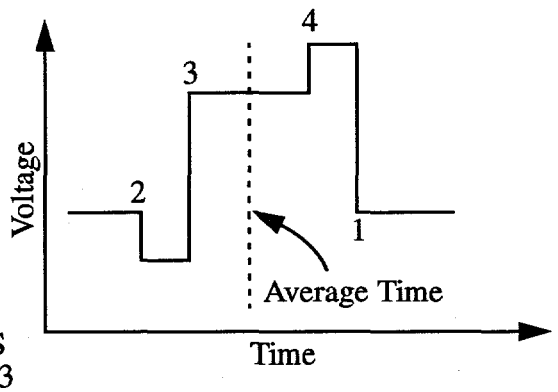

Trigger from S
Fiducial from 3

(4) Measurements of the relative travel times of the data and the fiducial between the target and the digitizing electronics (this includes settable delay generators).

In an "ideal" experiment similar to the powder and gas gun tests presented in this report (similar, that is, except assumed to be ideal), all flush pins would be truly flush, impacts would be totally planar, and data transit time (via laser and electronics) would be identical to fiducial transit time (via electronics). Hence setting the delay generator for the fiducial to 7 μsec would give a fiducial appearing on the data trace at a position corresponding to

7μsec after impact.

To decide what actual time (relative to impact) is represented by the fiducial on a particular data trace, several corrections must be made:

1) "Pin 3 Correction" -- If the pin which generates the fiducial (Flush Pin 3 for the target-mounted circuit boards, or the first pin to fire for the OR circuit configuration) protrudes by a distance x, the fiducial will come sooner than ideal. The correction is to the time which the fiducial marks on the data traces; i.e. a protruding pin gives a positive correction and a recessed pins gives a negative correction. This correction is $(+)x/U_{fp}$, where U_{fp} is the projectile (flyer plate) velocity. This is zero for a rear-surface pin technique, as normally used for 2-stage gun tests.

2) "Planarity Correction" -- Ideally, the impact will be "pancake" (planar). If it is not, the projectile may not impact the target at Pin 3 at the same time as it impacts the center of the target (the best "impact time"). The correction, then, is the difference between the impact time on the target at Pin 3 and the impact time at the center of the target (positive for impacting at the center first). To calculate this correction, all of the flush pin settings must be measured (positive = protruding). This is zero for a rear-surface pin technique. The relative timing of the flush pin firings ("relative FP times," FP_i) is determined from the appropriate digitizer or oscilloscope record. Each of these timings is then adjusted to give a set of relative timings which would have been obtained if the pins had been totally flush ("corrected for settings"). This is accomplished by adding $(+)x_i/U_{fp}$ to the original relative FP times for each of the 4 flush pins. Here, i is a value from 1 to 4 corresponding to the pin in question. The impact at the center is then at a relative time $0.25 \cdot \Sigma\,((x_i/U_{fp}) + FP_i) \equiv t_{corr}$, while that on the target spot at Pin 3 is at a relative time $(x_3/U_{fp}) + FP_3 \equiv t_3$. The timing correction, then, is $t_{corr} - t_3$

3) "Electronic Timing Correction" -- Ideally, data reaches the digitizers or oscilloscopes in zero time, or at least all types of data (in particular, VISAR fringes and fiducials) take the same amount of time to reach the recording instrumentation, except for a settable delay in the fiducial (taken as 7 μsec in the example at the beginning of this discussion). In practice, these times differ. In our experiments, the VISAR data must travel at the speed of light from the target to the VISAR, then through the legs of the interferometer. The photomultiplier tubes have a finite response time (about 18 nsec), then travel time through cabling to acquisition electronics must also be added to the total travel time. Write this travel time as T_{Data}. The fiducial must travel through a very small circuit board, then through cabling, a delay generator and more cabling. In the powder gun and 2-stage gun tests, it then triggers an LED on the VISAR photomultiplier tubes. The signal then travels with the VISAR signals (as an added voltage pulse) to the recording instrumentation. In the gas gun tests, it goes directly into the acquisition electronics. Write this travel time (including the zero-setting delay of the delay generator) as T_{Fid}. Then the timing correction is $T_{Fid} - T_{Data}$.

All of these corrections are added to the dialed-in time of the fiducial delay to calculate an actual time of the fiducial relative to impact. The data trace is then shifted in time so that the observed fiducial occurs at that time.

As a check of timing, an experiment with known time properties may be conducted (as a

symmetric aluminum/aluminum impact). The time shift required to give the proper shock arrival time should match the shift required to properly time the fiducial as discussed above.

This page intentionally left blank

Distribution

External Distribution:

California Research and Technology
20943 Devonshire St.
Chatsworth, CA 91311-2376
Attn:
Anne Cooper
Sheldon Schuster

CEWES-SD
Waterways Experiment Station
3909 Halls Ferry Road
Vicksburg, MS 39180
Attn:
John Boa
Tony Bombich

DNA Nevada Operations Office
P.O. Box 98539
Las Vegas, NV 89193-8539
Attn:
Barbara Harris-West

FCDNA/FCTTS
1680 Texas St SE
Kirtland AFB, NM 87117
Attn:
George Baladi, FCTTS
Mike O'Brien, FCTO
George Lu, FCTI
Audrey Martinez, FCTTS
Eric Rinehart, FCTTS
Bob Reinke, FCTTS
Byron Rystvit, FCTTS

HQ/DNA DFTD
6801 Telegraph Road
Alexandria, VA 22310-3389
Attn:
Don Linger
Fran Rensvold

Ktech Corp
901 Pennsylvania Ave NE
Albuquerque NM 87110
Attn:
Frank Davies
Eric Smith

Lawrence Livermore National Laboratory
P.O. Box 808
Livermore, CA 94550
Attn:
Armand Attia, Mail Stop L-200
Dave Erskine, Mail Stop L-417
Lewis Glenn, Mail Stop L-200
Bill Moran, Mail Stop L-200
Kurt Sinz, Mail Stop L-200

Los Alamos National Laboratory
Los Alamos. NM 87545
Attn:
John B. Aidun, T-1 M/S B221
Arthur Cox, T-6 M/S B268
Thomas Dey, EES-5 M/S F665
James D. Johnson, T-1 M/S B221
James N. Johnson, T-1 M/S B221

R&D Associates
P.O. Box 9377
Albuquerque, NM 87119
Attn:
Larry Germain
Barbara Killian

SAIC/Pacifica Technology
10260 Campus Point Drive, MS 62
San Diego, CA 92121
Attn:
Martin Fogel
Dan Patch
Mike McKay
Jack Klump

S-Cubed, A Division of Maxwell Laboratories, Inc.
3398 Carmel Mountain Road
San Diego, CA 92121
Attn:
Jim Baker
Steve Peyton

S-Cubed, A Division of Maxwell Laboratories, Inc.
P.O. Box 1620
San Diego, CA 92038-1610
Attn:
Phil Coleman
Norton Rimer

Robert Bass
4505 Durango Ct. NE
Albuquerque, NM 87109

SRI International
333 Ravenswood Ave.
Menlo Park, CA 94025
Attn:
Don Curran
Paul deCarli

Vermont Marble Company
61 Main Street
Proctor, Vermont 05765
Attn:
Bill Richardson
Robert W. Solari

Thomas J. Ahrens
Seismological Laboratory
Division of Geological and Planetary Sciences
California Institute of Technology
Pasadena, CA 91125

Tom Duffy
Carnegie Institution of Washington
Geophysical Laboratory
5251 Broad Brach Road, NW
Washington, D. C. 20015-1305

Conrad Felice
Mission Research Corporation
9 Exchange Place
Suite 900
Salt Lake City, UT 84111

Paul Fisher
Springfield Research Facility
P.O. Box 1220
Springfield, VA 22151
Edward S. Gaffney
GRE Corp
2921 Carlisle Blvd NE
P.O. Box 30863
Albuquerque NM 87190-0863

Yogi. M.Gupta
Dept. of Physics
Shock Dynamics Laboratory
Washington State University
Pullman, WA 99124-2814

Skip Knowles
JAYCOR
1608 Spring Hill Road
Vienna, VA 22182-2270

Wesley Martin
Terra Tek
420 Wakara Way
Salt Lake City, Utah 84108

Frank McMullen
Tech Reps
5000 Marble Ave NE
Albuquerque NM 87110-6390

John L. Remo
Quantametrics, Inc.
#1 Brackenwood Path
Head of the Harbor
St. James, NY 11780

Ken Sites
SAIC
P.O. Box 19057
Las Vegas, NV 89119

Sandia Internal Distribution:

MS 0321 1400 E. H. Barsis
MS 1111 1402 S. J. Dosanjh
MS 0318 1403 G. S. Davidson
MS 0821 1404 J. A. Ang
MS 1111 1421 Manager
MS 1110 1422 R. C. Allen
MS 1110 1423 E. F. Brickell
MS 1109 1424 A. L. Hale
MS 0819 1431 J. M. McGlaun
MS 0820 1432 A. Farnsworth
MS 0820 1432 G. I. Kerley
MS 0820 1432 M. E. Kipp
MS 0820 1432 F. R. Norwood
MS 0820 1432 P. Yarrington
MS 0821 1433 L. C. Chhabildas
MS 0821 1433 D. Crawford
MS 0821 1433 M. D. Furnish (20)
MS 0821 1433 D. E. Grady
MS 0821 1433 R. McIntosh
MS 0821 1433 M. Shahinpoor
MS 0821 1433 P. L. Stanton
MS 0439 1432 D. R. Martinez
MS 0437 1562 E. P. Chen
MS 0327 2514 L. J. Weirick
MS 0458 5602 J. R. Asay
MS 1033 6111 J. L. Wise
MS 0751 6117 W. R. Wawersik
MS 0899 13414 Technical Library (5)
MS 0619 12613 Technical Publications
MS0100 7613-2 Document processing for DOE-OSTI (2)
MS 9018 8523-2 Central Technical Files
MS 1159 9311 T. K. Bergstresser
MS 1159 9311 A. J. Chabai
MS 1159 9311 L. Hill
MS 1159 9311 C. Smith
MS 0355 9723 M. J. Forrestal